الجمهورية الجزائرية الديمقراطية الشعبية
République Algérienne Démocratique et Populaire
وزارة التعليم العالي و البحث العلمي
Ministère de l'Enseignement Supérieur et de la Recherche Scientifique

Université Mohamed Khider – Biskra
Faculté des Sciences et de la Technologie
Département : Génie Mécanique
Ref : ……

جامعة محمد خيضر - بسكرة
كلية العلوم والتكنولوجيا
قسم : الهندسة الميكانيكية
المرجع : .....

Thèse Présentée en vue de l'obtention du diplôme de

Doctorat LMD en Génie Mécanique

Spécialité : Génie Mécanique

Contribution à l'étude d'éléments finis spéciaux pour des simulations numériques à trois dimensions précises

---

Présentée par :

Hossam DJAHARA

Soutenue publiquement le 16/04/2024

Devant le jury composé de :

Pr. Lakhdar SEDIRA	**Professeur**	**Président**	**Université de Biskra**
Pr. Kamel MEFTAH	**Professeur**	**Rapporteur**	**Université de Batna 2**
Dr. Tahar MASRI	**MCA**	**Examinateur**	**Université de Biskra**
Pr. Wahid KADDOURI	**Professeur**	**Examinateur**	**Université de Batna 2**

People's Democratic Republic of Algeria
Ministry of Higher Education and Scientific Research
Mohamed Khider University of Biskra
Faculty of Sciences and Thechnology
Department of Mechanical Engineering

Order Number: .....

THESIS

In Candidacy for the Degree of
DOCTOR 3rd CYCLE IN MECHANICAL ENGINEERING
Option: Mechanical Engineering

TITLE

Contribution to the Study of Special Finite Elements for Precise Three-dimensional Numerical Simulations

Presented by **Hossam Djahara**

Defended on: 16/04/2024

In front of the jury composed of:

Pr. Lakhdar Sedira	Professor	President	University of Biskra
Pr. Kamel Meftah	Professor	Supervisor	University of Batna 2
Dr. Tahar Masri	MCA	Examiner	University of Biskra
Pr. Wahid Kaddouri	Professor	Examiner	University of Batna 2

To

My beloved family
Parents, siblings
and my lovely wife
My Professors
and my friends.

Acknowledgements

"In the name of Allah, the Most Gracious and the Most Merciful"

Allah Almighty said : [31:12] "*Be grateful to Allah, for whoever is grateful, it is only for their own good*"

I would like to praise *Allah* the Almighty, the Most Gracious, and the Most Merciful for His blessing In the completion of this thesis. Then, may Allah's blessing goes to His final Prophet *Muhammad* (peace be up on him), his family and his companions.

The writer wishes to acknowledge his deepest gratitude for all generous guidance and assistance which has given to him by a lot of people.

I would like to express my greatest gratitude and appreciation to my supervisor Pr. Kamel Meftah, who has given me his valuable guidance, advice and understanding so I could complete this thesis. Most importantly, of the confidence he gave us to work independently.

Great thanks and appreciation the writer give to the jury members, Pr. Lakhdar Sedira for doing me the honor of chairing the jury, Dr. Tahar Masri and Pr. Wahid Kaddouri, as the examiners who had given suggestions, criticism, improvements, and valuable inputs for the thesis. Special thanks goes to Pr. Lakhdar Sedira for his encouragement and countless moments of support and aid.

My ultimate thanks is dedicated to my beloved Mother, Aida Abibsi, my beloved Father, Mohamed Djahara, for their endless support, love, and prayer. my special thanks go to my brother Oussama, my sisters Sara, Hadil, Rahaf and my beloved wife Fatiha Traka who have given me plentiful help and support in completing this thesis. Also, huge thanks go to my best friends Abbase, Nawi, Mohamed, Sofian, Hakim, Fares, Fouad, Aymen, for every single moment we cherished together since the first day up to this very second. Also, I would like to express my thanks to all my friends and all persons who helped me in completing this thesis whose names cannot be mentioned one by one for their help and support.

Hossam Djahara

ملخص

تقدم هذه الأطروحة التحقق من صحة العناصر المحدودة عالية الترتيب المطورة حديثًا لتحليل الهياكل والسلوكيات المادية المختلفة في كل من الأنظمة الخطية وغير الخطية. وتعتمد هذه العناصر على مفهوم دوران الألياف الفضائية (SFR) المعروف بفعاليته. يتيح SFR الدوران في الفضاء للألياف الافتراضية ثلاثية الأبعاد داخل العنصر، مما يوفر ست درجات من الحرية (DOFs) لكل عقدة (ثلاث ازاحات وثلاث للدوران)، مما يعزز تقريب مجال الإزاحة الكلاسيكي. تشتمل العناصر الجديدة على عناصر سداسية السطوح ذات 20 عقدة مطابقة (SFR20) وغير مطابقة (SFR20I). يتم استخدام أسلوب الأوضاع غير المتوافقة في صياغة العناصر غير المطابقة لتجنب أوجه القصور العددية المرتبطة بقفل نسبة بواسون. تم اختيار العناصر عالية الترتيب لمعالجة متطلبات تهذيب الشبكة للعناصر ذات الترتيب المنخفض ومشكلات تشويه الشبكة. تتضمن عملية التحقق من التحقق الخطي مع تكامل منخفض وتقييم الأداء من خلال اختبارات التشويه ونسبة العرض إلى الارتفاع والتقارب عبر هياكل مختلفة. بالإضافة إلى ذلك، يتم إجراء التحقق غير الخطي من خلال تنفيذ العناصر ونموذج اللدونة في برنامج Abaqus في شكل روتين فرعي كعنصر محدد من قبل المستخدم (UEL) وروتين فرعي محدد للمادة من قبل المستخدم (UMAT). وبشكل عام، تُظهر العناصر المقترحة أداءً فائقًا، خاصة في التعامل مع تشويه الشبكة.

الكلمات المفتاحية: عنصر متناهي سداسي الأوجه، دوران الألياف في الفضاء، درجات الحرية الدورانية، تحليل الايلاستوبلاستيكي، التحليل غير الخطي، أبيكوس، عنصر معرف من مستخدم (UEL) ، المواد المعرفة من المستخدم (UMAT)

Abstract

This thesis presents the validation of newly developed high-order finite elements for analyzing various structures and material behavior in both linear and nonlinear regimes. These elements are based on the Space Fiber Rotation (SFR) concept, known for its effectiveness. SFR enables a spatial rotation of a three-dimensional virtual fiber within the element, introducing six Degrees of Freedom (DOFs) per node (Three translation and three rotation), which enhances the approximation of the classical displacement field. The novel elements include conforming (SFR20) and non-conforming (SFR20I) Hexahedral 20-node elements. The incompatible modes approach is utilized in the non-conforming element formulation to avoid numerical deficiencies related to Poisson's ratio locking. High-order elements are chosen to address mesh refinement requirements for low-order elements and mesh distortion issues. The validation process involves linear validation with reduced integration and performance assessment through distortion, aspect ratio, and convergence tests across various structures. Additionally, nonlinear validation is conducted by implementing the elements and the plasticity model in Abaqus software in the form of User defined ELement (UEL) and User defined MATerial subroutine, respectively. Overall, the proposed elements demonstrate superior performance, particularly in handling mesh distortion.

Keywords: Hexahedral finite element ; Space Fiber Rotation ; Rotation degrees of freedom ; Elastoplastic analysis ; nonlinear analysis ; Abaqus ; User defined ELement (UEL) ; User defined MATerial (UMAT)

Résumé

Cette thèse présente la validation de nouveaux éléments finis d'ordre supérieur développés pour analyser diverses structures et comportements des matériaux dans des régimes linéaires et non linéaires. Ces éléments sont basés sur le concept dite Space Fiber Rotation (SFR), reconnu pour son efficacité. Le SFR permet une rotation spatiale d'une fibre virtuelle tridimensionnelle à l'intérieur de l'élément, introduisant six Degrés de Liberté (DDL) par noeud (trois translations et trois rotations), ce qui améliore l'approximation du champ de déplacement classique. Les nouveaux éléments incluent des éléments hexaédriques conformes (SFR20) et non conformes (SFR20I) à 20 noeuds. L'approche des modes incompatibles est utilisée dans la formulation des éléments non conformes pour éviter les déficiences numériques liées au verrouillage du coefficient de Poisson. Les éléments d'ordre supérieur sont choisis pour répondre aux exigences de raffinement du maillage pour les éléments de faible ordre et aux problèmes de distorsion du maillage. Le processus de validation comprend une validation linéaire avec une intégration réduite et une évaluation des performances à travers des tests de distorsion, de rapport d'aspect et de convergence sur diverses structures. De plus, la validation non linéaire est réalisée en mettant en oeuvre les éléments et le modèle de plasticité dans le logiciel Abaqus sous forme de subroutine User Defined ELement (UEL) et User Defined MATerial, respectivement. Dans l'ensemble, les éléments proposés démontrent une performance supérieure, en particulier dans la gestion de la distorsion du maillage.

Mots clés : Élément fini hexaédrique ; Rotation spatiale des fibres ; Degrés de libert de rotation ; Analyse élastoplastique ; analyse non linéaire ; Abaqus ; Élément défini par l'utilisateur (UEL) ; Matériel défini par l'utilisateur (UMAT)

Contents

List of Figures

List of Tables

Nomenclature

Abbreviations

SFR	Space Fiber Rotation
DOFs	Degrees of Freedom
UEL	User defined ELment
UMAT	User defined MATerial
FEM	Finite Element Method
PDEs	Partial Differential Equations
2D	Two-dimension
3D	Tree-dimension
NURBS	Non-Uniform Rational B-Splines
IGA	Isogeometric Analysis
CAD	Computer-aided Design
BEM	Boundary Element Method
EAS	Enhanced Assumed Strain
HR	Hellinger-Reissner
NICE	Nodally Integrated Continuum Element
PFR	Plane Fiber Rotation
SPH	Small Perturbation Hypothesis
PVW	Principle of Virtual Work
NC	Non-Conforming
GP	Gauss points

Matrix notation

$[\bullet]$	Matrix
$\{\bullet\}$	Column vector
$\langle\bullet\rangle$	Row vector
$[\bullet]^T$	Transpose of a matrix
$[\bullet]^{-1}$	Inverse of a matrix
$det\,([\bullet])$	Determinant of a matrix

Greek Symbols

Υ	The motion or trajectory of the particles
Ω	Closed boundary
t	Current time
t_0	Initial time
ρ	Material density
ε_{ij}	Linearized deformation tensor
ω_{ij}	Linearized rotation tensor
ε	Strain tensor
$\varepsilon_{xx}, \varepsilon_{yy}, \varepsilon_{zz}$	Principal deformation in the directions e_1, e_2 and e_3 axis, respectively
$\gamma_{xy}, \gamma_{xz}, \gamma_{yz}$	Angular deformation in the angle between i and j
σ	Stress tensor

$\sigma_{xx}, \sigma_{yy}, \sigma_{zz}$	Principal stresses in the directions e_1, e_2 and e_3 axis, respectively
$\tau_{xy}, \tau_{xz}, \tau_{yz}$	Tangential or shear stresses
ν	Poisson's ratio
λ	Lamé's coefficient
Γ	Boundary of a continuous domain
ξ, η and ζ	Local coordinate system
$\underline{\theta}$	Rotation vector
$\underline{iq}$	Virtual fiber
$\overline{\Pi}$	Potential energy
Λ	Strain energy
Ξ	External forces
ε^E	Enhanced or incompatible strain vector
ε^e	Elastic strain tensor
ε^p	Plastic strain tensor
ϕ	Yield function
π-plane	Deviatoric plane
ψ	Function of the total strain
α	Back-stress tensor
$\dot{\gamma}$, $\dot{\lambda}$	Plastic multiplier
$\dot{\varepsilon}^p$	Plastic flow
Ψ	Plastic flow potential
θ	Load Angle
φ	Internal friction or friction angle
ι, k	Material parameters
$\boldsymbol{\eta}$	Relative shifted stress tensor
μ	Shear modulus
ϵ_{tol}	Equilibrium convergence tolerence

Latin Symbols

$\mathbb{A}$	Hardening thermodynamical force
a_u, a_v and a_w	Scale factors
$\mathcal{B}$	Fixed orthogonal coordinate system
B	Strain matrix
C	Tree dimension elasticity matrix
C^e, C^p	Elastic and plastic stress-strain matrices
C^{ep}	Elastoplastic stress-strain matrice
c	Cohesion
D	Deformable solid body
D_0	Deformable solid body at initial configuration
$\mathbb{D}^p$	Plastic dissipation function
E	Young modulus
e_p	Effective plastic strain
$\mathcal{F}_{ij}$	Deformation gradiant tensor
F^e_{int}	Element internal force vector
F^e_{ext}	Element external force vector

$\overrightarrow{f}_v$	Volumetric forces
G	Shear modulus
$\mathcal{F}$	Deformation gradient tensor
$\mathbb{H}$	Displacement gradient tensor
H	Hardening thermodynamical forces
H_{iso}	Isotropic Hardening
H_{kin}	Kinematic Hardening
P	Hydrostatic stress vectors
S	Diviatoric stress vectors
J	Jacobian matrix
j	Jacobian inverse matrix components
$detJ$	Determinant of the Jacobian matrix
$detJ_0$	Determinant of the Jacobian matrix evaluated at the center of the element
J_1, J_2, J_3	Stress invariants
$\mathcal{S}$	Surface plane or diaphragm
$\overrightarrow{T}$	Surface forces
M	Material point
m	Number of Gausse points
$\overrightarrow{n}$	Unite normal
N	Shape functions
N_{node}	Number of nodes
$\mathbb{N}$	Flow vector
P, Q	Material particles
K^e	Element stiffness matrix
K	Bulk modulus
r	Residual or out-of-balance force
$\mathcal{T}_e$	Transformation process
T_0	Matrix relating Cartesian and covariant strain vectors
$\vec{U}$	Displacement vector between two particle
V	Deformed body in equilibrium
$\vec{X}_i$	Random vector
X	Random variable
U, u	Displacement field with respect to x axis
V, v	Displacement field with respect to y axis
W, w	Displacement field with respect to z axis
$\mathcal{W}$	The weak form of the equilibrium
u_i, v_i and w_i	Nodal displacement
x, y and z	Global coordinates
w_i, w_j and w_k	Wieght Coefficients

Operators

$Grad, grad$	Gradient in the reference and in the current configuration
Div, div	Divergenz in the reference and in the current configuration
$\times$	Cross product
$\cdot$	Scalar product
:	Dual scalar product

$\otimes$	Tensor product
$\wedge$	Vectorial product
$*$	Appropriate product operation
lim	Limit of a function
∂	Partial differential operator
$\frac{d\bullet}{d\bullet}$	Time derivative of $(\bullet)$
δ_{ij}	Kronecker delta
$\bullet^T$	Transpose of vector or matrix $(\bullet)$
$\Delta\bullet$	Increment of $(\bullet)$
$\emptyset$	Empty set
$\cup$	Union
$\cap$	Intersects
$\frac{\partial\bullet}{\partial\bullet}, \dot{\bullet}$	Partial derivative of $(\bullet)$
$\| \bullet \|$	Norm of $(\bullet)$
$\delta\bullet$	(Vector-valued) Variation of $(\bullet)$
$\mathrm{A}(\bullet)$	Assembly process of $(\bullet)$
$\sum$	Sum process
$tr(\bullet)$	Trace of $(\bullet)$
$(\bullet)^{trail}$	Trail quantities
$\sin, \cos$	Sine, cosine
$\tan, cot$	Tangent, Cotangent

Chapter 1

General Introduction

Summary

1.1 Introduction

The Finite Element Method (FEM) stands out as a highly powerful tool in numerical simulation, renowned for its reliability, robustness, and efficiency. Ever since the initial mathematical validations of its formulation Babuska and Aziz , the FEM has established itself as a formidable platform for addressing Partial Differential Equations (PDEs) across diverse domains, encompassing heat transfer, fluid mechanics, electromagnetic potential, and the advancement of efficient nanoscale systems [1]. In solid mechanics, there has been a notable surge of interest in 3D modeling, particularly in response to the significant expansion of computational resources [2].

One of the main advantages of the FEM is its ability to handle complex geometries and boundary conditions Zienkiewicz et al. [3]. It also allows for the incorporation of material properties, which makes it a powerful tool for analyzing the behavior of different materials. Additionally, the FEM can provide accurate and detailed results that are

difficult or impossible to obtain through experimental testing [4]. However, the FEM also has some limitations and drawbacks. One of the main challenges is the requirement for accurate modeling of the geometry, material properties, and boundary conditions [5]. Inaccuracies in these areas can lead to errors in the results. Additionally, the FEM requires significant computational resources and time, especially for complex geometries and high-fidelity models [6]. Finally, the FEM can be sensitive to the choice of mesh size and shape, which can affect the accuracy and convergence of the solution Oden et al. [7].

There are various approaches and methods used to enhance the performance and accuracy of the finite elements for solving complex engineering problems. One such approach is the use of adaptive mesh refinement, which involves refining or coarsening the mesh based on the solution's local error estimates Babuška and Rheinboldt [8]. This approach can reduce the computational cost of the FEM while maintaining high accuracy. Another method used to enhance the performance of the FEM is the use of higher-order basis functions, such as the B-spline and NURBS (Non-Uniform Rational B-Splines) functions Piegl and Tiller [9]. These basis functions can provide more accurate solutions than traditional linear basis functions and can handle complex geometries more efficiently. Another special type of finite element used in the FEM is the isogeometric analysis (IGA) method, which utilizes the same basis functions as those used in computer-aided design (CAD) software Hughes et al. [10]. This method can simplify the mesh generation process and provide accurate solutions for problems involving curved geometries. In recent years, machine learning techniques have been applied to enhance the performance of the FEM, such as using neural networks for solution approximation and optimization Ling et al. [11]. This approach can provide a more efficient and accurate solution for high-dimensional and nonlinear problems. Finally, the FEM can be coupled with other numerical methods to provide a more comprehensive solution for complex problems, such as the FEM-Boundary Element Method (BEM) coupling for fluid-structure interaction problems Brebbia and Wrobel [12]. This approach can provide an efficient and accurate solution for problems involving complex domains and material interfaces.

One effective approach to enhance the performance of the FEM is the use of high-order finite elements. Unlike traditional linear elements, high-order elements use higher-degree polynomials to approximate the solution, which can lead to more accurate and efficient results Zienkiewicz and Taylor [3]. High-order elements also offer the advantage of reducing the number of elements required to discretize a domain, which can lead to a reduction in the computational cost of the FEM. There are several types of high-order finite elements used in the FEM, including quadratic, cubic, and higher-order elements. Quadratic elements use second-degree polynomials to approximate the solution, while cubic and higher-order elements use even higher-degree polynomials. The use of higher-order elements can provide more accurate solutions for problems involving complex geometries

and material properties Cottrell et al. [13]. However, the use of high-order elements can also pose some challenges. One major challenge is the increased computational cost due to the larger number of degrees of freedom required to represent the higher-degree polynomials accurately. Another challenge is the difficulty of generating high-quality meshes that can accurately capture the high-order solution behavior. Despite these challenges, the use of high-order finite elements is becoming increasingly popular in the FEM due to their ability to provide more accurate and efficient solutions for complex engineering problems. This approach has been successfully applied in various fields, including structural mechanics, fluid dynamics, and electromagnetics Arnold et al. [14].

Computation cost is a significant concern in the Finite Element Method since it can have a direct impact on the accuracy and efficiency of the solution. One of the main contributors to the computational cost in the FEM is the number of degrees of freedom (DOF) required to represent the problem accurately. In general, the larger the number of DOF, the longer the computational time required to obtain a solution. Various strategies have been proposed to address the issue of computation cost in the FEM. One approach is to use efficient algorithms and data structures that can minimize the memory requirements and improve the computational efficiency. Another approach is to use parallel computing techniques to distribute the computation across multiple processors and reduce the computational time Saad [15]. Moreover, the use of adaptive mesh refinement can significantly reduce the computational cost by refining the mesh only in regions where the solution requires high accuracy Babuska et al. [16]. Additionally, the use of reduced-order modeling techniques, such as model order reduction, can provide a significant reduction in the computational cost while maintaining acceptable accuracy levels Benner et al. [17]. However, it is important to note that reducing the computation cost may also come at the expense of reduced accuracy. Therefore, it is essential to strike a balance between computational cost and accuracy when using the FEM. In summary, computation cost is an important consideration in the FEM, and various strategies have been proposed to address this issue. By using efficient algorithms, parallel computing techniques, adaptive mesh refinement, reduced-order modeling techniques, and special finite elements, it is possible to reduce the computational cost while maintaining acceptable levels of accuracy.

In this context the presented work aims to provide new high-order and special finite elements. These elements are based on the Space Fiber Rotation (SFR) concept for the analysis of linear and nonlinear problems including (solids and structures). The SFR considers the spatial rotation of a virtual fiber within the element resulting in an enhancement in the displacement vector approximation. The developed elements are a conforming and a nonconforming element named SFR20 and SFR20I, respectively. The nonconforming version is mainly proposed to avoid numerical difficulties related to the

Poisson's ration locking phenomena. Thus, the performance of the elements is validation through linear and elastoplastic problems. The validation of the proposed elements SFR20 and SFR20I in linearity is done through the implementation of the elements in the form of subroutines in *"Reflex"* which is a pre-developed code developed by Batoz and Dhatt [18]. The accuracy and efficiency of elements is assessed through a series of Three-dimensional linear elastic benchmarks including beams, plates and shell structures. The elements are investigated by different type of tests as; distortion tests, aspect ratio and convergence tests. In order to investigate the performance of the SFR20 element to analyze the elastoplastic behavior of structures, the presented element was implemented as a **U**ser defined **EL**ement (UEL) subroutine in the Commercial Finite Element Software *Abaqus*. This was motivated by the need for a powerful and accurate envirement to handle the nonlinear analysis of structures, add to that the fact that *Abaqus* provides a general interface for the visualisation purposes. Moreover, the elastoplastic model was also implemented as **U**ser **MAT**erial (UMAT) subroutine in combination with th (UEL) subroutine.

1.2 State of the art

1.2.1 Review of special 3D finite elements in elasticity

The elemental formulation's significance in Finite Element Analysis (FEA) has prompted numerous endeavors aiming to refine the accuracy, efficiency, and versatility of these elements since their inception. These efforts have yielded a plethora of models and methodologies, with many pioneering works eventually integrated into commercial finite element software. The development of high-performance, low-order solid elements has gained considerable traction, particularly in meeting the demands of 3D modeling. Although standard low-order hexahedral elements offer cost efficiency, they suffer from well-known deficiencies, notably the occurrence of locking when shape functions inaccurately interpolate a field [19], potentially leading to erroneous results. Researchers such as Hughes et al. [20] and Zienkiewcs et al. [21] have effectively addressed locking phenomena through the introduction of reduced and selective reduced integration techniques, respectively. Moreover, Wilson et al. [22] introduced incompatible displacement modes to improve the element's displacement field. This initial approach being confined to parallelograms, Taylor et al. [23] rectified the flawed terms and conducted a patch test to refine this formulation. Similarly, Simo and Rifai [24] pioneered a family of three elements rooted in the Enhanced Assumed Strain (EAS) approach, augmenting the strain field by incorporating an additional field of variables to accommodate linear problems. Correspondingly,

Andelfinger and Ramm [25] utilized the EAS concept to develop membrane, plate, and shell finite elements, discussing their equivalence with Hellinger-Reissner (HR) elements. The EAS technique, aligned with the Hu-Washizu principle, was applied to address the nonlinear regime in the works of Simo and Armero [26] and Simo et al. [27]. Furthermore, several 3D finite elements emerged based on this approach, including Fredriksson and Ottosen's [28] presentation of a stabilized hexahedral element evaluated through 3D elasticity problems. Similarly, Sousa et al. [29] introduced a set of solid finite elements demonstrating minimal sensitivity to mesh distortion, resulting in heightened accuracy for 3D and thin shell applications. Another proposed method in the academic literature to create precise finite elements is through hybrid/mixed formulations [30]. Hybrid elements primarily rely on enforcing constraint conditions to guarantee interelement compatibility by introducing Lagrange multipliers [31], while Mixed elements are derived from a multi-field variational functional. Numerous other innovative works have been suggested in this domain for both linear and nonlinear analyses [32, 33, 34, 35, 36], to highlight a few.

Additionally, finite elements with rotational degrees of freedom have demonstrated significant efficiency in addressing both linear and nonlinear structural problems. Following the groundbreaking work of Allman [37], several successful methods integrating rotational DOF in 2D and 3D finite elements have been introduced [38, 39, 40, 41]. Utilizing the Hybrid formulation, Yunus et al. [38] developed hexahedral, quadrilateral, and triangular finite elements for resolving 3D and 2D elasticity problems. Similarly, Yunus et al. [39] and Pawlak et al. [40] introduced a hexahedron and a tetrahedron finite element, respectively. The inclusion of rotational DOFs in these elements stemmed from transforming the mid-side translational DOF of the standard 20-node hexahedron and 10-node tetrahedron, respectively. Shang et al. [42] recently introduced an 8-node hexahedral element designed for addressing size-dependent problems. This 48-DOF element originates from an earlier formulation by Shang et al. [43], which is essentially based on the modified couple stress theory.

The Space Fiber Rotation (SFR) concept stands as another pioneering effort to develop highly accurate finite elements with rotational DOF. Initially introduced by Ayad [41], this concept revolves around considering the rotation of a spatial virtual fiber within the element, resulting in additional rotational DOFs. Several authors [44, 45, 46, 47, 48, 49, 50] adopted this assumption to create a series of efficient 2D and 3D finite elements. In their innovative work, Ayad et al. [45] presented two 8-node hexahedrons: a conforming (SFR8) and a nonconforming (SFR8I) finite element. The latter includes three incompatible modes and was primarily proposed to resolve the Poison's ratio locking problem present within the SFR8 element. These elements were utilized in the research of Meftah et al. [46] to address geometric nonlinear problems. In a similar vein, Meftah et al. [47] introduced a multilayer version of the SFR8 element, labeled SFR8M, to model composite laminated

structures. Meftah and Sedira [48] suggested a linear four-node tetrahedral finite element, SFR4, for modeling solid structures. Ayadi et al. [49] recently adopted the SFR approach to analyze 3D nonlinear elastoplastic problems.

The massive development of computational resources has sparked renewed interest in high-order finite elements, driven by their rapid convergence and superior accuracy. In recent years, a multitude of 2D finite elements have been introduced within this domain [51, 52, 53], just to mention a few. Conversely, specific high-order solid finite elements have been proposed for 3D modeling. Ooi et al. [54] proposed a 20-node hexahedron based on an asymmetry that exploits intrinsic properties of different sets of shape functions, resulting in an efficient finite element with a notable tolerance to mesh distortion. This approach was subsequently expanded to encompass geometric nonlinearities [55]. Li et al. [56] introduced a 21-node hexahedral spline element incorporating an internal node, achieving second-order completeness in Cartesian coordinates. This element demonstrated superior performance compared to standard 20-node serendipity elements, particularly in terms of sensitivity to mesh distortion.

1.2.2 Review of the related work for 3D finite element in elasto-plasticity

The development of plasticity theory has been shaped by numerous significant contributions from researchers across the years, where it can be traced back to the work of Tresca (1864) [57], whose led to the development of his well known Tresca criterion where he stated that metals yielded plasticaly when the maximum shear stress reach a critical value. Another notable contribution to the development of plastic theory were made by Saint-Venant (1870) [58] and Lévy (1870) [59]. Otto Mohr's introduction of the yield surface concept in 1900 was also a key contribution, providing a fundamental framework for understanding plastic deformation [60]. Richard Von Mises made a profound impact on plasticity theory with his proposal of the Von Mises yield criterion in 1913, which remains a cornerstone of plasticity modeling [61]. Additionally, eminent researchers like Hencky (1924) [62] and Prandtl (1924) [63] amongst others made significant strides in understanding the theory of plasticity . Furthermore, the development of numerical methods and computational techniques, such as the Finite Element Method (FEM), greatly advanced the computational modeling of plastic deformation [3]. Indeed, the finite element method is regarded as the most suitable and reliable method for the analysis of nonlinear behavior involving elastoplastic materials. Elastoplastic analysis is of utmost importance in engineering and material science as it enables the understanding and prediction of material behavior beyond the elastic limit. It plays a crucial role in designing structures and

components that are subject to complex loading conditions, such as those encountered in manufacturing processes, structural engineering, and geomechanics. By considering the plastic deformation of materials, elastoplastic analysis provides insights into the response of structures under realistic conditions, where permanent deformations and energy dissipation occur. Elastoplastic analysis by the finite element method has gained huge interest from scientists since the first contributions in the mid-1960s [64, 65, 66].

The use of high-order finite elements or special methods and aproaches offers improved accuracy and efficiency compared to the classical formulation with low-order elements. Several works provide valuable insights into the utilization of such elements and approaches in elastoplastic analysis. May et al. [67] presents a comprehensive study on the elastoplastic behavior of beams under pure and warping torsion. The work focuses on the development and application of a 20-noded isoparametric brick finite element to accurately simulate the complex mechanical response of materials under torsional deformations. Where we find in the work of Weber et al. [68] aims to improve the accuracy, stability, and robustness of numerical simulations in analyzing the complex behavior of materials undergoing plastic deformations, by presenting a novel and objective time-integration method to efficiently solve isotropic elastic-plastic constitutive equations, both rate-independent and rate-dependent, under various loading conditions. Armero et al. [69] investigate the phenomenon of strain localization in solids, to understand and analyze the factors influencing strain localization and its numerical simulation using finite element methods. Another specialized technique for elastoplastic fracture analysis using finite elements with minimal remeshing was presented by Belytschko et al. [70], enabling efficient and accurate modeling of crack growth under plastic conditions. Cao et al. [71] presents a novel brick element formulation to overcome the limitations of conventional finite element methods by introducing a three-field variational principle that enhances the representation of complex material deformations and stress states. Several shell elements were developed for nonlinear problems involving elastoplastic analysis, Rank et al. [72] investigate the benefits and challenges of using high-order elements for accurately modeling the complex behavior of shell structures, such as thin-walled components and curved surfaces, in various engineering applications. Recently, Artioli et al. [73] developed and implemented a new linear hexahedral element based on Nodally Integrated Continuum Element (NICE) formulation to efficiently capture complex material behaviors and stress distributions in elastoplastic simulations. Moreover, a novel mixed finite element method for the analysis of elastoplastic materials addresses the challenges associated with accurately simulating the complex behavior of materials undergoing plastic deformations using highly anisotropic volume elements by Nagler et al. [74]. Another approache is the Space Fiber Rotation (SFR) concept which was successfully adopted for the analysis of different

type of problems including (Linear, nonlinear and composite materials analysis), it considers the rotaion of a virtual fiber within the element, the 3D rotaion of the fiber results in additional degrees of freedom (DOFs) that enhance the displacement field. Meftah et al. [46] adopted an 8-node hexahedral element for the analysis of geometric nonlinearity, the implementation of SFR8 element was to improve the representation of large displacements and rotations in engineering simulations. In the work of Meftah et al. [47] the same element was extanded to a new multilayered element denoted SFR8M to model composite laminate structures. Moreover, The hexahedral element SFR8 was assessed to analyse material nonlinearities for elastoplastic materials and to enhance material deformations and stress states Ayadi et al. [49]. Add to that, a plane adaptation (Plane Fiber Rotation) of the SFR concept was considered for the development of a quadrilateral finite element denoted PFR8 to analyse the behavior of plane structures, such as plates and membranes, under the influence of elastoplastic deformations [50].

1.3 Motivation

One way to enhance the performance and the accuracy of the finite elements is by using high order formulation elements. Despite, the good behavior of such elements still were not given the value in developement unlike the linear approximation elements. The use of high order elements in this work is motivated by the good performance of such elements to aviod the requirements to use the mesh refinement for low order elements and overcome mesh distortion phenomenon. Another motivation comes with need to investigate the performance of elements to analyse the elastoplastic behavior of structures, where these elements are a reduced integration scheme element SFR20 with $3\times3\times3$ Gauss points and a complet or full integration scheme element with $4\times4\times4$ Gauss points denoted as SFR20F. Finale motivation is the necessity to complete the family of volumetric finite elements based on the Space Fiber Rotation (SFR) concept; by investigating the behavior and performance of high order elements, especially, after the successful performance showed by the low order elements in the work of Ayad et al. [45], Meftah et al. [46] and Ayadi et al. [49], to mention but a few.

1.4 Scope of the thesis

This work is a contribution to develop new high order finite elements in the family based on the Space Fiber Rotation concept (SFR). This concept has proved its efficiencies through the literature for the analysis of different structures in linearity and non linearity. High order elements represent good rate of convergence and the high order approximation field

gives the ability to model complex shape of structures. For this purpose, the aim of this thesis is to introduce improvements and novel elements, this elements are based on the Space Fiber Rotation concept (SFR); the elements are hexahedrals with 20-nodes and denoted as SFR20 and SFR20I.

The formulation, implementation and validation of the proposed elements is carried out through two parts of the work. The first part of the work is related to the validation of elements in linear analysis for different type of structures by :

- Implementing these elements in a pre-coded environment *"Reflex"*.
- In order to overcome the fact that the new elements uses high number of DOFs, an investigation must be conducted through applying different type of analysis as; rate of convergence and aspect ration tests.
- The proposed elements are exposed to several distortion test to investigate their sensitivity for mesh distortion on the behavior of elements.
- Since the developed elements use high number of Degrees of Freedom DOFs; they need to be assessed for time efficiency tests to evaluate the run time cost with respect to other elements from the literature.

The second part of the work is to investigate the performance of the conforming element SFR20 with a reduced and full integration schemes. for the analysis of elastoplastic behavior for different type of structures, to achieve this objective:

- The proposed element is implemented as a **U**ser defined **EL**ement subroutine in the commercial finite element software *"Abaqus"*.
- Implementing the constitutive plasticity model through the User defined MATerial subroutine which is called for each integration point within one element in UEL.
- Simple tests need to be conducted to verify the correctness of the computation implementation for the UEL element and the constitutive model in UMAT subroutine.
- Exposing the SFR20 for different series of typical structural problems to evaluate the element's performance to analyse the elastoplastic behavior.
- Validation of the proposed element with other reference solution and developed elements from the literature.

1.5 Structure of the work

In order to address the research objective, this thesis is organized into six distinct chapters that covers key themes and methodologies. The thesis began with a general introduction that gives a general review for the related work. The general introduction was followed by the second chapter which addresses a general overview of the continuum mechanics and essential basics in the finite element method. As long as, the presented work is about the development of new special finite element based on an original technique; the third chapter presents a theoretical formulation of the developed elements SFR20 and SFR20I. This chapter was followed by the validation of the proposed elements in linearity for different type of structures and tests. The theory of plasticity and numerical modelling of the elastoplastic behavior are presented in chapter five. The validation of the SFR20 element for the analysis of elastoplastic behavior is adopted in chapter six. Finally, the thesis ends with a general conclusion summarizing the work done.

General introduction covers state of the art related to the development and validation of solid finite elements in linear and nonlinear analysis. **Chapter 2** presents the mathematical tools to describe any kinematics of bodies. Also, the description for deformation of a body, add to that, it gives the fundamentals to touch in the Finite Element Method. The second part of this chapter give a general overview of the finite element method in three dimensions. The Space Fiber Rotation (SFR) concept was introduced in **Chapter 3**, where it presents a detailed formulation of two high order hexahedral finite elements, a conforming and non-conforming elements, denoted as SFR20 and SFR20I, respectively. The element matrices of both elements were expressed with the appropriate Gaussian integration schemes. **Chapter 4** is concerned about the validation of the developed elements in the previous chapter, where these elements are implemented in a pre-programmed code in the form of a subroutines and exposed to various type of tests and structures as; distortion sensitivity test, convergence tests and aspect ratio tests. The structures are including; beams, shells and plates. Also, the elements are investigated for computational cost by determine the required time to calculate the element stiffness matrices. **Chapter 5** is devoted to provide a general framework for numerical modelling of the elastoplastic behavior. Furthermore, it addresses an overview on the plasticity theory, followed by the computation of the elastoplastic constitutive equations. This chapter is concluded with the process to solve the nonlinear equations with the finite element method. In **Chapter 6** the validation of the developed SFR20 element to analyse the elastoplastic behavior is presented. Where the element is exposed to several well know tests in the literature. The thesis ends with a **General conclusion**, where it summarizes the major findings, achieved from the proposed elements. Future research work are also discussed in this chapter.

In **Appendix A**, the shape functions and their derivatives for the classical 20 nodes hexahedral element are presented. General tutorial on the implementation of the presented SFR20 element with the constitutive plasticity model in a form of subroutine in the commercial finite element program *Abaqus* by Simulia Dassault Systems is given in **Appendix B**.

The structure of this thesis ensures a comprehensive analysis of the research topic, covering key themes such as Continuum mechanics, Finite element method, Space fiber rotation concept formulation, Plasticity theory and validation of the presented elements SFR20 and SFR20I in linearity and for the SFR20 element for the analysis of the elasto-plastic behavior with two integration schemes by implementation of the SFR20 element via UEL subroutine and the constitutive plasticity model via UMAT subroutine.

Chapter 2

Theoretical background on the continuum mechanics and finite element method

Summary

2.1 Introduction

Problems in engineering and mathematical physics are described in a form of differential equations, and it is generally not possible to obtain an analytical solution for these equations, especially, in case of complicated geometries, boundary conditions and material properties. The favourable way to obtain an acceptable solution is to rely on numerical methods such as the finite element method. The finite element method is a numerical method that allows to solve differential equations that describe engineering and mathematical physics problems. These problems include; structural analysis, heat transfer, fluid dynamics, electromagnetic potential.
In order to understand the finite element method it is better to touch basics on continuum mechanics. The continuum mechanics is introduced to present the mathematical tools to describe any kinematics of bodies. add to that, continuum mechanics makes it possible to take into account the deformations of a body and the temperature variations that accompany these deformations.
The main objective of this chapter is to give a general overview of the continuum mechanics and the finite element method. This chapter is divided into two parts; the first part addresses principles on continuum mechanics; for a detailed treatment on the continuum mechanics which is presented in this chapter the reader is refered to the textbooks [75, 76, 77]. The second part will give a general overview on the formulation of the FEM in three dimensions; Regarding the finite element method the reader is refered to the standard textbooks to mention but a few [78, 79, 80, 81].

2.2 Kinematics of continuum mechanics

2.2.1 Description of motion

Figure 2.1 presents a deformable solid body D with closed boundary Ω, and t_0 is the time where we begin to monitor its motion and deformation. We consider the body D_0 with bounded boundary Ω_0 at time t_0 as the initial or reference configuration. Let $\mathcal{B} = (O, \vec{X}_1, \vec{X}_2, \vec{X}_3)$ a fixed cartisian coordinate system and the origin of this coordinate system is located outside of the body. M_0 is a material point in the initial reference at time t_0 with the coordinates (x_0, y_0, z_0). At time t_0 the body D_0 is disturbed by any type of forces (concentrated, surface or volumetric) its material particles experience motion and as a result at current time $t > t_0$ the body D_0 occupies a different configuration D_t with closed boundary Ω_t. We refer to the new configuration as the current configuration. The point M_0 from the initial configuration occupies position M_t with coordinates (x_t, y_t, z_t) in the current configuration with respect to the same fixed orthogonal coordinate system

B. The motion or trajectory of the particles or the undeformed and deformed bodies between initial and current configurations can be described by a mapping Υ over time t as:

$$x = \Upsilon(X, t) \tag{2.1}$$

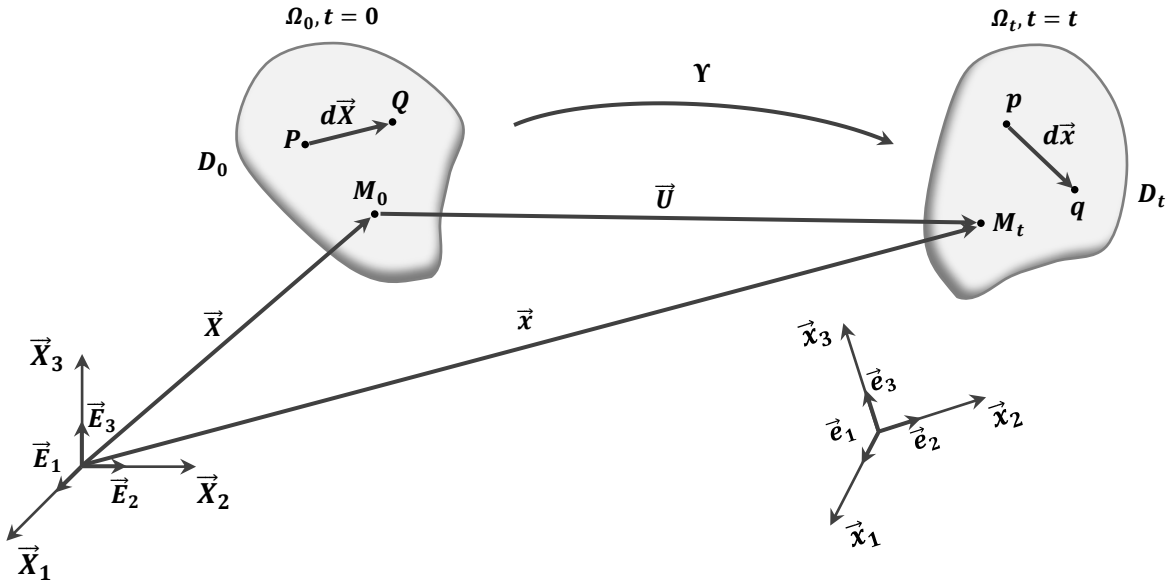

Figure 2.1: Description of motion of a deformable body.

2.2.1.1 Material and spatial description

The motion of the deforming body can be described in two possible ways. Choosing the appropriate coordinate system that describe the motion of the body is an important step. Where it can be described in terms of where the body was before deformation or where it is during deformation; The former is a material or Lagrangian description where it refers to the behavior of a material particle, whereas the latter is a spacial or Eulerian description refers to the behavior at a spacial position [75]. Let ρ be a simple scalar quantity as the current density of the material ; we define Lagrangian and Eulerian description as :

Material or Lagrangian description: The state of body in the current configuration requires initial position coordinates of the material points this leads to the variation of ρ over the body is described with respect to the original (or initial) coordinate X used to label a material particle (identified by a point M_0).

$$\rho = \rho\,(X, t) \tag{2.2}$$

Spatial or Eulerian description: Eulerian description is radically different from that of Lagrange. We do not consider initial instance, and we do not even try to follow a particle in its movement. We are interested in a fixed point M_0, whose coordinates are indicated by the x position vector. The variation of ρ is described with respect to the position in space.

$$\rho = \rho\,(x, t) \tag{2.3}$$

2.2.2 Deformation gradiant

Consider a material domain D during the deformation of continuum, and more particularly to the comparison between its initial D_0 and current D_t states. Since it is a material domain, each particle located at a point M_0 of the initial configuration is still present in the current configuration at a point M_t.

In typical Lagrangian notation, we can note the following location vectors:

$$\begin{cases} \overrightarrow{OM}_0 = \overrightarrow{X} \\ \overrightarrow{OM}_t = \overrightarrow{x} \end{cases} \quad \Rightarrow \quad \overrightarrow{x} = \overrightarrow{X} + \overrightarrow{U} \tag{2.4}$$

The Equation (2.4) can be written in a vectorial form as:

$$\begin{Bmatrix} x_1 \\ x_2 \\ x_3 \end{Bmatrix} = \begin{Bmatrix} X_1 \\ X_2 \\ X_3 \end{Bmatrix} + \begin{Bmatrix} u \\ v \\ w \end{Bmatrix} \tag{2.5}$$

Let P and Q be a material particles in the neighbourhood of a material particle M_0 Figure 2.1. After deformation, the material particles P, Q and M_0 have deformed to current configuration as p, q and M_t. A fundamental tool to compare the initial and final position of the particles of a material domain subjected to a transformation is the *deformation gradient tensor*, with components:

$$\mathcal{F}_{ij} = \frac{\partial x_i}{\partial X_j} = x_{i,j} \tag{2.6}$$

This two order tensor give the ability to connect the relative position of two adjacent particles before and after deformation. Based on this notation we can write:

$$\overrightarrow{dx} = \mathcal{F}.\overrightarrow{dX} \tag{2.7}$$

The elements of the matrix F are the partial differential of the actual coordinates with respect to the initial coordinates. Hence:

$$[\mathcal{F}] = \begin{bmatrix} \frac{\partial x_1}{\partial X_1} & \frac{\partial x_1}{\partial X_2} & \frac{\partial x_1}{\partial X_3} \\ \frac{\partial x_2}{\partial X_1} & \frac{\partial x_2}{\partial X_2} & \frac{\partial x_2}{\partial X_3} \\ \frac{\partial x_3}{\partial X_1} & \frac{\partial x_3}{\partial X_2} & \frac{\partial x_3}{\partial X_3} \end{bmatrix} \tag{2.8}$$

The matrix $\mathcal{F}$ is the Jacobian Matrix, and its determinant is called the Jacobian,who is written as follow:

$$\overrightarrow{dx} = J.\overrightarrow{dX} \tag{2.9}$$

Hence, the deformation gradient $\mathcal{F}$ can be expressed in the global reference $B = (O, \vec{X}_1, \vec{X}_2, \vec{X}_3)$ by:

$$\begin{Bmatrix} dx_1 \\ dx_2 \\ dx_3 \end{Bmatrix} = \begin{bmatrix} \frac{\partial x_1}{\partial X_1} & \frac{\partial x_1}{\partial X_2} & \frac{\partial x_1}{\partial X_3} \\ \frac{\partial x_2}{\partial X_1} & \frac{\partial x_2}{\partial X_2} & \frac{\partial x_2}{\partial X_3} \\ \frac{\partial x_3}{\partial X_1} & \frac{\partial x_3}{\partial X_2} & \frac{\partial x_3}{\partial X_3} \end{bmatrix} \begin{Bmatrix} dX_1 \\ dX_2 \\ dX_3 \end{Bmatrix} \tag{2.10}$$

If we differentiate the values inside $\mathcal{F}$, we get:

$$\begin{Bmatrix} dx_1 \\ dx_2 \\ dx_3 \end{Bmatrix} = \begin{bmatrix} 1 + u_{,X_1} & u_{,X_2} & u_{,X_3} \\ v_{,X_1} & 1 + v_{,X_2} & v_{,X_3} \\ w_{,X_1} & w_{,X_2} & 1 + w_{,X_3} \end{bmatrix} \begin{Bmatrix} dX_1 \\ dX_2 \\ dX_3 \end{Bmatrix} \tag{2.11}$$

This lead us to:

$$\mathcal{F} = I + L \tag{2.12}$$

with:

$$L = \begin{bmatrix} u_{,X_1} & u_{,X_2} & u_{,X_3} \\ v_{,X_1} & v_{,X_2} & v_{,X_3} \\ w_{,X_1} & w_{,X_2} & w_{,X_3} \end{bmatrix} \tag{2.13}$$

Because L is an unsymmetrical tensor, it can be decomposed into an antisymmetric $[W]$ and a symmetric $[D]$ tensors, where:

$$[L] = [W] + [D] \tag{2.14}$$

The linearized deformation tensor in small deformation is:

$$[D] = \frac{1}{2}[D + D^T] = \begin{bmatrix} u_{,X_1} & \frac{1}{2}(u_{,X_2} + v_{,X_1}) & \frac{1}{2}(u_{,X_3} + w_{,X_1}) \\ & v_{,X_2} & \frac{1}{2}(v_{,X_3} + w_{,X_2}) \\ sym. & & w_{,X_3} \end{bmatrix} \tag{2.15}$$

2.2.3 Displacement

We defined previously $\overrightarrow{U}$ as the displacement vector of a particle M_0 for initial configuration M_t, the vector $\overrightarrow{U}$ relates two points M_0 and M_t by this relation:

$$\overrightarrow{U} = \overrightarrow{M_0 M_t} = \overrightarrow{x} - \overrightarrow{X} \tag{2.16}$$

The displacement gradient tensor is defined as follow:

$$\mathbb{H} = grad\overrightarrow{U} \tag{2.17}$$

Or we can write:

$$\mathbb{H}_{ij} = \frac{\partial U_i}{\partial X_j} \tag{2.18}$$

As like all the second tensors, $\mathbb{H}$ can be defined or decomposed into tow parts, a symetric and unsymetric part:

$$\mathbb{H} = \varepsilon + \omega \tag{2.19}$$

We define the symmetric and the unsymmetrical parts as follows:

$$\begin{cases} \varepsilon = \frac{1}{2}\left(\mathbb{H} + \mathbb{H}^T\right) \\ \omega = \frac{1}{2}\left(\mathbb{H} - \mathbb{H}^T\right) \end{cases} \tag{2.20}$$

By replacing Equation (2.18) in Equation (2.20), we can define the tensors in a matrix notation:

$$\begin{cases} \varepsilon_{ij} = \frac{1}{2}\left(\frac{\partial U_i}{\partial X_j} + \frac{\partial U_j}{\partial X_i}\right) \\ \omega_{ij} = \frac{1}{2}\left(\frac{\partial U_i}{\partial X_j} - \frac{\partial U_j}{\partial X_i}\right) \end{cases} \tag{2.21}$$

where ε and ω are the linearized deformation and rotation tensors, respectively.

2.2.4 Linearized deformation tensor (Strain tensor)

In the classical linear theory of elasticity, the displacement gradient is supposed to be very small. We consider the Small Perturbation Hypothesis (SPH) that takes its origins from the Lagrangian description because it compares the state of two references. The hypothesis states that the displacement between the initial to the actual configuration are very small and displacements gradient are also very small. It is well known that the Green-Lagrange deformation depends in a nonlinear way with displacements. Based on the definition of the Green-Lagrange tensor:

$$E = \frac{1}{2}\left(\mathcal{F}^T \cdot \mathcal{F} - I\right) \tag{2.22}$$

The deformation gradient can be expressed in function of the displacement gradient using:

$$\mathcal{F} = \frac{\partial \overrightarrow{x}}{\partial \overrightarrow{X}} = \frac{\partial\left(\overrightarrow{X} + \overrightarrow{U}\right)}{\partial \overrightarrow{X}} = I + \frac{\partial \overrightarrow{U}}{\partial \overrightarrow{X}} \tag{2.23}$$

We write E in the following form:

$$E = \frac{1}{2}\left(\frac{\partial \overrightarrow{U}}{\partial \overrightarrow{X}} + \left(\frac{\partial \overrightarrow{U}}{\partial \overrightarrow{X}}\right)^T + \left(\frac{\partial \overrightarrow{U}}{\partial \overrightarrow{X}}\right)^T \cdot \frac{\partial \overrightarrow{U}}{\partial \overrightarrow{X}}\right) \tag{2.24}$$

Based on the definition of the SPH, the expression above will be reformulated by neglecting the quadratic or the nonlinear terms, the result is:

$$E \simeq \frac{1}{2}\left(\frac{\partial \overrightarrow{U}}{\partial \overrightarrow{X}} + \left(\frac{\partial \overrightarrow{U}}{\partial \overrightarrow{X}}\right)^T\right) \tag{2.25}$$

The quantity in the right side of the expression above is called the right Green-Lagrange deformation tensor, denoted as ε. The relation between deformation-displacement wrote as follow:

$$\varepsilon = \frac{1}{2}\left(\frac{\partial \overrightarrow{U}}{\partial \overrightarrow{X}} + \left(\frac{\partial \overrightarrow{U}}{\partial \overrightarrow{X}}\right)^T\right) = \frac{1}{2}\left(\mathcal{F} + \mathcal{F}^T\right) - I \tag{2.26}$$

We define the deformation tensor in one point by the classical formula of the linear mechanics, as follow:

$$\varepsilon_{ij} = \frac{1}{2}\left(\frac{\partial \overrightarrow{U}_i}{\partial \overrightarrow{X}_j} + \frac{\partial \overrightarrow{U}_j}{\partial \overrightarrow{X}_i}^T\right) \tag{2.27}$$

The deformations are symmetric based on the Kronecker delta δ_{ij} rule as:

$$\delta_{ij} = \begin{cases} 1 & i = j \\ 0 & i \neq j \end{cases} \quad ; \quad \varepsilon_{ij} = \varepsilon_{ji} \tag{2.28}$$

This leads to:

$$[\varepsilon] = \begin{bmatrix} \varepsilon_{xx} & \varepsilon_{xy} & \varepsilon_{xz} \\ & \varepsilon_{yy} & \varepsilon_{yz} \\ Sym & & \varepsilon_{zz} \end{bmatrix} \tag{2.29}$$

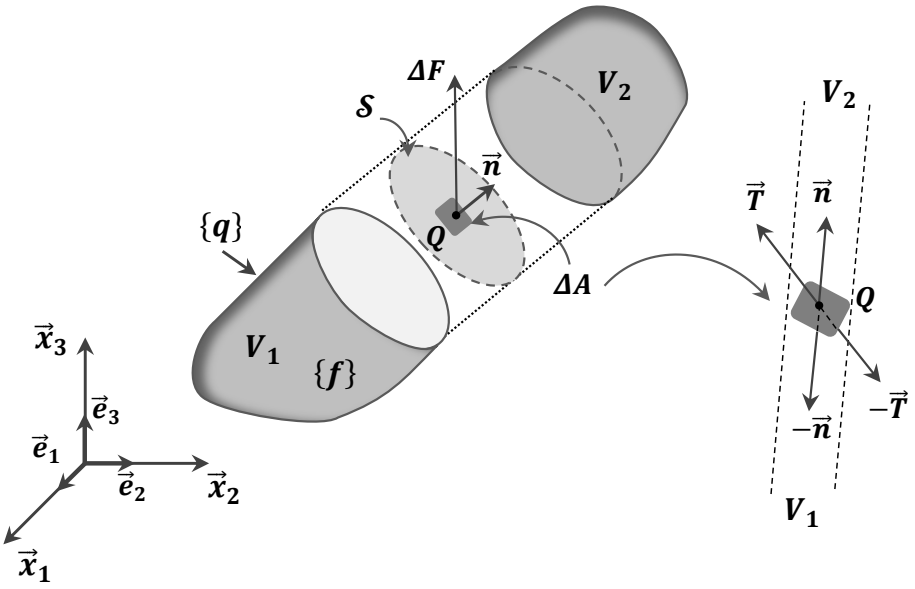

Figure 2.2: Stress tensor description in a deformable body.

The deformation tensor can be determined by knowing six components out of nine, which can be present in vectorial form by:

$$\{\varepsilon\} = \{\varepsilon_{xx}\ \varepsilon_{yy}\ \varepsilon_{zz}\ \gamma_{xy}\ \gamma_{xz}\ \gamma_{yz}\}^T \tag{2.30}$$

Where γ_{xy}, γ_{xz} and γ_{yz} are the angular deformation that represent the variation in the angle between i and j.

$$\begin{cases} \gamma_{xy} = 2\varepsilon_{xy} \\ \gamma_{xz} = 2\varepsilon_{xz} \\ \gamma_{yz} = 2\varepsilon_{yz} \end{cases} \tag{2.31}$$

2.2.5 Stress tensor

Calling V a deformed body in equilibrium bounded by boundary ∂V at any time t Figure 2.2. The body V is cut into two volumes V_1 and V_2 by a hypothetical diaphragm or cut plane $\mathcal{S}$ and bounded by ∂V_1 and ∂V_2, respectively. The body V is subjected to surface q and volume f forces; these forces are acting on the cut area ΔA and the forces exerted by volumes V_1 and V_2 on both sides of the diaphragm $\mathcal{S}$ are maintaining the equilibrium of the body V. In order to maintain the equilibrium of the body V after the cut, a virtual forces ΔF are defined that are equal and opposite in direction and exercise on the diaphragm $\mathcal{S}$ on the area ΔA.

In the neighbourhood of special point Q, Let $\overrightarrow{n}$ be unite normal to the area ΔA and ΔF is the resultant force on this area. Stress tensor $T^{(n)}$ at point Q associated to the

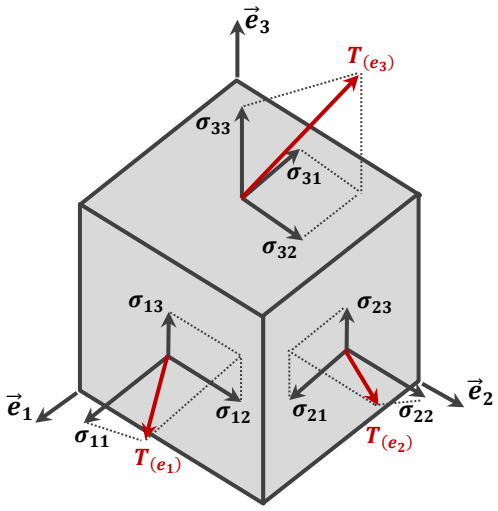

Figure 2.3: Cauchy's Stress tensors components.

plane whose normal to $\overrightarrow{n}$, is define as:

$$T_{(n)} = \lim_{\Delta A \to 0} \frac{\Delta F}{\Delta A} = \frac{dF}{dA} \tag{2.32}$$

Thus, there is an infinity of vectors of the stresses T at point Q depending on the orientation of the vector $\overrightarrow{n}$. The tensor T can be decomposed to $T(e_1)$, $T(e_2)$ and $T(e_3)$ based on the directions of the axes on the orthogonal Cartesian base $B(e_1, e_2, e_3)$, see Figure 2.3:

$$\begin{cases} T_{(e_1)} = \sigma_{xx}e_1 + \sigma_{xy}e_2 + \sigma_{xz}e_3 \\ T_{(e_2)} = \sigma_{yx}e_1 + \sigma_{yy}e_2 + \sigma_{yz}e_3 \\ T_{(e_3)} = \sigma_{zx}e_1 + \sigma_{zy}e_2 + \sigma_{zz}e_3 \end{cases} \tag{2.33}$$

The Cauchy stress tensor at point Q is defined as follows:

$$T_{(e_i)} = \sigma_{ij}e_j \tag{2.34}$$

Where $[\sigma]$ is the stress matrix at point Q, and it is symmetric ($\sigma_{ij} = \sigma_{ji}$), and we can write:

$$[\sigma] = \begin{bmatrix} \sigma_{xx} & \sigma_{xy} & \sigma_{xz} \\ & \sigma_{yy} & \sigma_{yz} \\ Sym & & \sigma_{zz} \end{bmatrix} \tag{2.35}$$

The stress matrix $[\sigma]$ can be determined by six components, that can be defined in vectorial representation:

$$\{\sigma\} = \{\sigma_{xx}\ \sigma_{yy}\ \sigma_{zz}\ \tau_{xy}\ \tau_{xz}\ \tau_{yz}\}^T \tag{2.36}$$

Where the diagonal terms are normal or principal stresses in the directions e_1, e_2 and e_3. The non-diagonal terms are the tangential or shear stresses, which we often noted as τ_{ij}. Finally, the matrix of the Cauchy tensor is most often written as follows:

$$[\sigma] = \begin{bmatrix} \sigma_{11} & \tau_{12} & \tau_{13} \\ & \sigma_{22} & \tau_{23} \\ Sym & & \sigma_{33} \end{bmatrix} \tag{2.37}$$

2.2.6 Stress-strain relationship

In elasticity the behaviour of the material is characterized by two hypothesises, where the first relationship between the stress and strain is linear, second, the material has the property for complete recovery to the initial (natural) shape on the removal of loads and there is no loss of energy. With these hypothesises we write the constitutive equation for elastic behaviour that present the relation between the stress and the strain, as follows:

$$\{\sigma\} = [C]\{\varepsilon\} + \{\sigma_0\} \tag{2.38}$$

For linear elastic materials, the stress is a linear function of the strain. Constitutive Equation (2.38) for infinitesimal deformation is referred to as the *Generalized Hook's Law.*

Where C is the behaviour elasticity matrix with a dimension of 6×6 that has 36 components. Because of the symmetry of both the stress and strain tensors, we write:

$$C_{ijkl} = C_{jikl} = C_{ijlk} \tag{2.39}$$

These will reduce the 36 components to 21 distinct coefficients at most which is the case for a fully anisotropic material. However, in the case of isotropic linear elasticity, *Hook's law* is now written in a matrix form, involving all the terms of stress and strain tensors, as follows:

$$\begin{Bmatrix} \sigma_{11} \\ \sigma_{22} \\ \sigma_{33} \\ \sigma_{12} \\ \sigma_{13} \\ \sigma_{23} \end{Bmatrix} = \begin{bmatrix} 2G+\lambda & \lambda & \lambda & 0 & 0 & 0 \\ \lambda & 2G+\lambda & \lambda & 0 & 0 & 0 \\ \lambda & \lambda & 2G+\lambda & 0 & 0 & 0 \\ 0 & 0 & 0 & G & 0 & 0 \\ 0 & 0 & 0 & 0 & G & 0 \\ 0 & 0 & 0 & 0 & 0 & G \end{bmatrix} \begin{Bmatrix} \varepsilon_{11} \\ \varepsilon_{22} \\ \varepsilon_{33} \\ \varepsilon_{12} \\ \varepsilon_{13} \\ \varepsilon_{23} \end{Bmatrix} \tag{2.40}$$

in which G and λ are the shear modulus and Lamé's coefficient, respectively, and they are expressed in terms of Young's modulus E and Poisson's ratio ν:

$$\begin{cases} G &= \frac{E}{2(1+\nu)} \\ \lambda &= \frac{E\nu}{(1+\nu)(1-2\nu)} \end{cases} \tag{2.41}$$

2.2.7 Equilibrium

Figure 2.4 shows a continuous domain Ω bounded by boundary Γ. The body S is at the current configuration and subjected to solicitation such as surface forces $\overrightarrow{T}$ applied at the region Γ_σ, imposed displacements $\overrightarrow{U}$ at the region Γ_U, and volumetric forces $\overrightarrow{f}_v$. The boundary Ω is split into Γ_σ and Γ_U, so that $\Gamma = \Gamma_\sigma \cup \Gamma_U$ and $\Gamma_\sigma \cap \Gamma_U = \emptyset$. Based on these notations the boundary conditions are expressed as:

$$\begin{cases} U_i = U_i^* & in \quad \Gamma_U \\ \sigma_{ij} n_j = T_i & in \quad \Gamma_\sigma \end{cases} \tag{2.42}$$

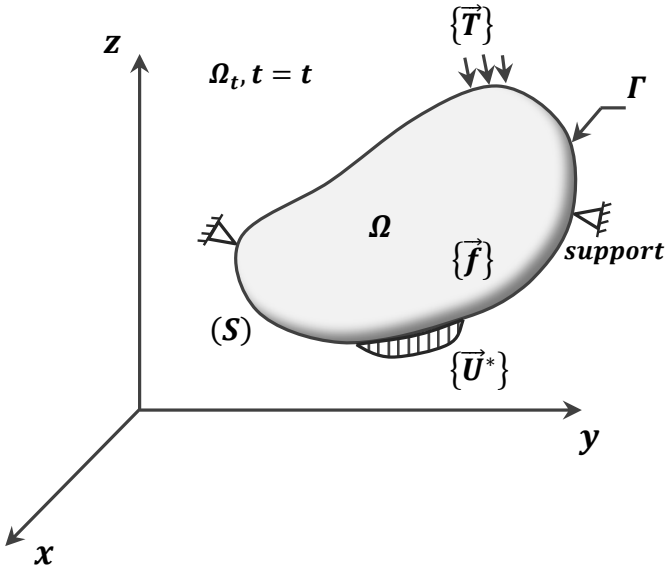

Figure 2.4: Equilibrium of an elastic domain.

Where T_i and U_i^* are the prescribed boundary values of traction and displacement, respectively, and n_j is the i^{th} component of the normal vector, and U_i is the displacement vector of Ω. The translational equilibrium implies that the sum of all forces acting on the body vanishes. The equilibrium of the solid body depicted in Figure 2.4 can be defined as:

$$\iint_S \overrightarrow{T} dS + \iiint_V \overrightarrow{f_v} dV = 0 \tag{2.43}$$

Equation (2.43) can be expressed in terms of the Cauchy stresses as:

$$div\,(\sigma) + f^v = 0 \tag{2.44}$$

Where σ and f_v are respectively the mechanical stress and the body forces. The equilibrium of the system is written as:

$$\begin{cases} div\,(\sigma) + f^v = 0 & in \quad \Omega \\ U_i = U_i^* & in \quad \Gamma_U \\ \sigma_{ij} n_j = T_i & in \quad \Gamma_\sigma \end{cases} \tag{2.45}$$

2.3 General overview of the Finite Element Method

The same continuous domain Ω bounded by boundary Γ presented in Section 2.2.7 is considered in Figure (2.5). The body is subjected to external loads. The external load acting onto the body are surface traction $\overrightarrow{T}$ and body forces $\overrightarrow{f}$.

One of the most used methods to solve the Equation (2.43) is the *Finite Element Methods* (FEM) that replaces the continuous system S with a discrete system. The solid is divided into a number of sub-domains Ω_e called *elements*, where the assembly of all sub-domains allows the reconstitution of the initial geometry Equation (2.46). Each element is connected to its neighbours by *nodes* and the solution is sought at these points.

$$\Omega \approx \underset{e=1}{\overset{n_e}{\mathrm{A}}} \Omega_e \tag{2.46}$$

where n_e is the number of sub-domains or elements, and $\mathrm{A}\,(\bullet)$ is denoted the assembly process.

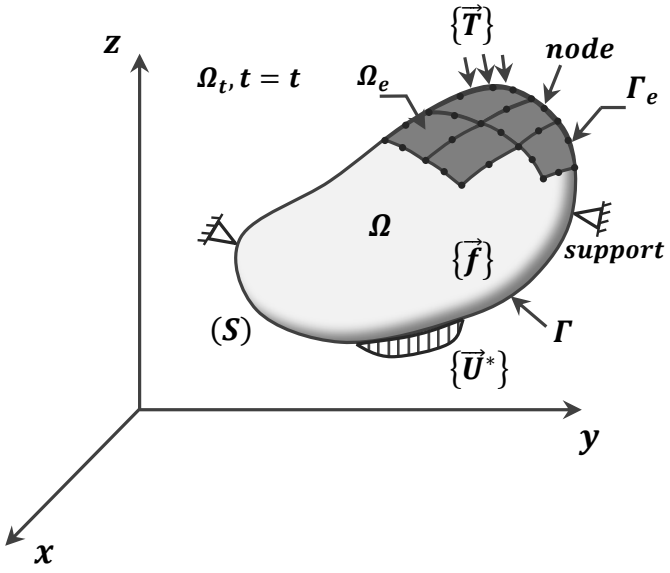

Figure 2.5: Discretisation of an elastic domain with finite elements.

Considering a cinematically admissible displacement field on the element Ω, In order to formulate the equations for the elements, it is advantageous to define *local coordinate system* (ξ, η and ζ) that is defined for an element in reference to the *global coordinate*

system (x, y and z) that is usually defined for the entire structure as shown in Figure (2.6).

The displacement field within the element can be assumed by polynomial interpolation using the displacements at its nodes, as:

$$X(x,y,z) = \sum_{i=1}^{N_{node}} N_i(x,y,z) \cdot X_i \tag{2.47}$$

Where N_{node} is the number of nodes forming the element, N_i are the *interpolation* or *shape functions* and X_i is the *nodal displacement* at the i^{th} node where the unknowns rises.

The transformation $\mathcal{T}_e$ makes it possible to calculate the coordinates of point $P(x,y,z)$ of the reel element from those of the corresponding point $P(\xi,\eta,\zeta)$ of the reference element, so we have:

$$\mathcal{T}_e : \xi,\eta,\zeta \rightarrow \begin{cases} x(\xi,\eta,\zeta) \\ y(\xi,\eta,\zeta) \\ z(\xi,\eta,\zeta) \end{cases} \tag{2.48}$$

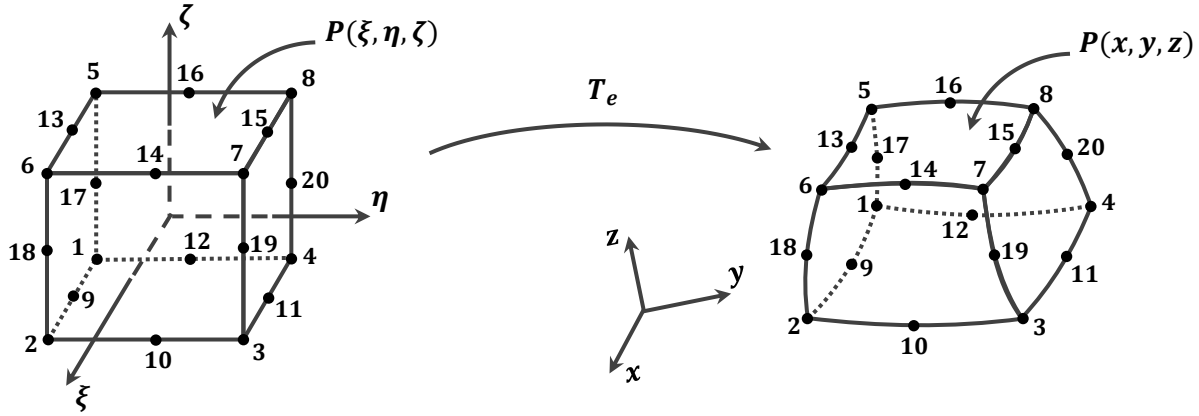

Figure 2.6: 20 node hexahedral element: local reference (Left), global reference (right).

In each element Ω_e, the position of all points is defined by:

$$X(\xi,\eta,\zeta) = \sum_{i=1}^{N_{node}} N_i(\xi,\eta,\zeta) \cdot X_i \tag{2.49}$$

The displacement field within the element can be assumed by polynomial interpolation using the displacement at its nodes, as:

$$U(\xi,\eta,\zeta) = \sum_{i=1}^{N_{node}} N_i(\xi,\eta,\zeta) \cdot U_i \tag{2.50}$$

Where $\{U\} = \{u\ v\ w\}^T$ and the parameters of the nodal displacement $\{U_i\} = \{u_i\ v_i\ w_i\}^T$.

$$\begin{cases} u(\xi,\eta,\zeta) = \sum_{i=1}^{N_{node}} N_i(\xi,\eta,\zeta) \cdot u_i \\ v(\xi,\eta,\zeta) = \sum_{i=1}^{N_{node}} N_i(\xi,\eta,\zeta) \cdot v_i \\ w(\xi,\eta,\zeta) = \sum_{i=1}^{N_{node}} N_i(\xi,\eta,\zeta) \cdot w_i \end{cases} \tag{2.51}$$

Where N_{node} is the number of nodes in element and the shape functions matrix N_i is defined with the following form:

$$N_i = \begin{bmatrix} N_1 & 0 & 0 & N_2 & 0 & 0 & \cdots & N_{N_{node}} & 0 & 0 \\ 0 & N_1 & 0 & 0 & N_2 & 0 & \cdots & 0 & N_{N_{node}} & 0 \\ 0 & 0 & N_1 & 0 & 0 & N_2 & \cdots & 0 & 0 & N_{N_{node}} \end{bmatrix} \tag{2.52}$$

2.3.1 Solution of the equilibrium

In engineering most, practical problems are governed by differential equations as the one developed in section 2.2.7 Equation (2.44). These equation is the *Strong form* of the governing system of equation for solids. In case of complex geometries and loading an exact solution of the governing equations are rarely possible. Indeed, the FEM is an approximate technique for solving differential equations. However, it is based on several other techniques. In contrast to strong form, the weak form is often an integral form an requires a weaker continuity on the field variables. Using the weak form usually produces a set of discretized well-behaved algebraic system of equations that give much more accurate results.

Principle of virtual work [82] and *Weighted residual method* [83] are the most widely used methods for creating the weak form of the system equations.

2.3.2 Principle of virtual work

Principle of Virtual Work (PVW) is the basis of many energy principles, such as the principle of minimum potential energy. The PVW postulates a power balance in virtual movement, and it stated as follows:

> *"If a deformable body is in equilibrium, the sum of the efforts is zero. By applying a fictitious (virtual) displacement δU to the body; the sum of the efforts remains zero."*

The weak form $\mathcal{W}$ of the equilibrium Equation (2.44) can be obtained by subjecting the body to an arbitrary virtual displacement δU, then the PVW requires that:

$$\mathcal{W} = \int_\Omega \delta U\,(div(\sigma) + f^v)\,d\Omega = 0 \quad ; \quad \forall \delta U \tag{2.53}$$

By substituting the boundary conditions in Equation (2.45), into Equation (2.53), and by rearranging the terms

$$\mathcal{W} = \int_{\Omega} \sigma_{ij} \delta\varepsilon_{ij} d\Omega - \left[\int_{\Omega} f_i^v \delta U_i d\Omega + \int_{\Gamma_\sigma} T_i \delta U_i d\Gamma \right] = 0 \tag{2.54}$$

Finally, we obtain the weak form of the equilibrium of the system at the actual configuration Ω:

$$\left\{ \begin{array}{rcll} \mathcal{W} & = & \mathcal{W}_{int} - \mathcal{W}_{ext} = 0 & \forall \delta U \\ \mathcal{W}_{int} & = & \int_{\Omega} \sigma_{ij} \delta\varepsilon_{ij} d\Omega & \\ \mathcal{W}_{ext} & = & \int_{\Omega} f_i^v \delta U_i d\Omega + \int_{\Gamma_\sigma} T_i \delta U_i d\Gamma & \end{array} \right. \tag{2.55}$$

$$\left\{ \begin{array}{lll} U = U^* & on & \Gamma_U \\ \delta U = 0 & on & \Gamma_U \end{array} \right. \tag{2.56}$$

Where $\delta\mathcal{W}_{int}$ and $\delta\mathcal{W}_{ext}$ are respectively the internal and external mechanical virtual works. The virtual linearized strain tensor $\delta\varepsilon$ is related to the virtual displacement δU by the following expression:

$$\delta\varepsilon = \frac{1}{2} \left(grad\,(\delta U) + grad(\delta U)^T \right) \tag{2.57}$$

The weak form Equation (2.54) can be rewritten in a vectorial notation as:

$$W = \int_{\Omega} \{\delta\varepsilon\}^T \{\sigma\}\, d\Omega - \left[\int_{\Omega} \{\delta U\}^T \{f^v\}\, d\Omega + \int_{\Gamma_\sigma} \{\delta U\}^T \{T\}\, d\Gamma \right] = 0 \tag{2.58}$$

With:

$$\left\{ \begin{array}{rcl} \{\delta U\} & = & \{\delta U\ \delta V\ \delta W\} \\ \{\delta\varepsilon\} & = & \{\delta U_{,x}\ \delta V_{,y}\ \delta W_{,z}\ \delta U_{,y} + \delta V_{,x}\ \delta U_{,z} + \delta W_{,x}\ \delta V_{,z} + \delta W_{,y}\} \\ \{\sigma\} & = & \{\sigma_{xx}\ \sigma_{yy}\ \sigma_{zz}\ \sigma_{xy}\ \sigma_{xz}\ \sigma_{yz}\} \\ \{f^v\} & = & \{f_x^v\ f_y^v\ f_z^v\} \\ \{T\} & = & \{T_x\ T_y\ T_z\} \end{array} \right. \tag{2.59}$$

2.3.3 Linear finite element analysis

The Finite element method is based on the discretization of the domain Ω, and the approximation of the solution functions consists on the transformation of the variational form in Equation (2.58) which is an integral on the whole region Ω and boundary Γ; to the sum of sub-domains (elements) and sub-boundaries of all elements, as follows:

$$\mathcal{W} = \sum_e \mathcal{W}^e = 0 \quad \forall \delta U \tag{2.60}$$

Where

$$\mathcal{W} = \sum_e \mathcal{W}^e = \sum_e \int_{\Omega^e} \{\delta\varepsilon\}^T \{\sigma\}\, d\Omega^e - \sum_e \int_{\Omega^e} \{\delta U\}^T \{f^v\}\, d\Omega^e - \sum_e \int_{\Gamma_\sigma^e} \{\delta U\}^T \{T\}\, d\Gamma^e = 0 \tag{2.61}$$

By replacing the displacement field Equation (2.50) in the deformation tensor Equation (2.27), we get the strain distribution within the element:

$$\{\varepsilon\} = [B]\,\{U_n\} \tag{2.62}$$

Equation (2.62) presents the strain-displacement relationship. Where the matrix $[B]$ contains the derivatives of the shape functions.

$$[B] = \begin{bmatrix} \frac{\partial N_i}{\partial x} & 0 & 0 \\ 0 & \frac{\partial N_i}{\partial y} & 0 \\ 0 & 0 & \frac{\partial N_i}{\partial z} \\ \frac{\partial N_i}{\partial y} & \frac{\partial N_i}{\partial x} & 0 \\ \frac{\partial N_i}{\partial z} & 0 & \frac{\partial N_i}{\partial x} \\ 0 & \frac{\partial N_i}{\partial z} & \frac{\partial N_i}{\partial y} \end{bmatrix} \tag{2.63}$$

The shape function $N_i(\xi, \eta, \zeta)$ are defined in local system, and the geometric transformation $\mathcal{T}_e$ allows as to transport from the local to the global system of coordinates and vice versa. This transformation is possible by introducing the Jacobian matrix :

$$\begin{Bmatrix} \frac{\partial N_i}{\partial \xi} \\ \frac{\partial N_i}{\partial \eta} \\ \frac{\partial N_i}{\partial \zeta} \end{Bmatrix} = \begin{bmatrix} \frac{\partial x}{\partial \xi} & \frac{\partial y}{\partial \xi} & \frac{\partial z}{\partial \xi} \\ \frac{\partial x}{\partial \eta} & \frac{\partial y}{\partial \eta} & \frac{\partial z}{\partial \eta} \\ \frac{\partial x}{\partial \zeta} & \frac{\partial y}{\partial \zeta} & \frac{\partial z}{\partial \zeta} \end{bmatrix} \cdot \begin{Bmatrix} \frac{\partial N_i}{\partial x} \\ \frac{\partial N_i}{\partial y} \\ \frac{\partial N_i}{\partial z} \end{Bmatrix} = [J] \begin{Bmatrix} \frac{\partial N_i}{\partial x} \\ \frac{\partial N_i}{\partial y} \\ \frac{\partial N_i}{\partial z} \end{Bmatrix} \tag{2.64}$$

The stresses within the element are related to the element strain by:

$$\{\sigma^e\} = [C]\,\{\varepsilon^e\} \tag{2.65}$$

Where $\{\sigma^e\}$ are the element stresses, and $[C]$ is the three dimensional elastic matrix written for a homogeneous and isotropic material presented in Equation (2.40). By substituting Equation (2.50), (2.62) and (2.65) into (2.61), we get:

$$\{\delta U\}^T \left[\sum_e \int_{\Omega^e} [B]^T [C] [B] \, d\Omega^e\right] \{U\} - \{\delta U\}^T \left[\sum_e \int_{\Omega^e} [N]^T \{f^v\} \, d\Omega^e + \sum_e \int_{\Gamma_\sigma^e} [N]^T \{T\} \, d\Gamma^e\right] = 0 \quad (2.66)$$

Equation (2.66) can be expressed by the following form:

$$[K^e] \{U_n\} - \{F^e\} = 0 \quad (2.67)$$

Where $[N]$ are the shape function matrix that connects the displacement vector with the vector of the unknown DOFs, $[K^e]$ is the element stiffness matrix, $\{U_n\}$ is the element displacement field variable and $\{F^e\}$ the element force vectors, respectively. All with respect to element e indicated by $\bullet^e$.

According to the Equation (2.46), the global stiffness matrix is giving by:

$$[K] = \sum_e [K^e] = \sum_e \int_{\Omega^e} [B]^T [C] [B] \, d\Omega^e \quad (2.68)$$

Where

$$[K^e] = \int_{\Omega^e} [B]^T [C] [B] \, d\Omega^e \quad (2.69)$$

The applied load vector $\{F^e\}$ is:

$$\{F^e\} = \int_{\Omega^e} [N]^T \{f^v\} \, d\Omega^e + \int_{\Gamma_\sigma^e} [N]^T \{T\} \, d\Gamma^e \quad (2.70)$$

Chapter 3

High order finite elements based on the Space Fiber Rotation Concept

Summary

3.1 Introduction

Since the birth of the finite element method until nowadays and the researchers seek to develop new robust and efficient finite elements. Despite, the good behavior and performance of the high order elements and the intensive research done, these elements still were not given the value in development unlike the linear approximation elements.
This Chapter present the kinematic of the Space Fiber Rotation (SFR) concept, a detailed formulation of new two high order finite elements belonging to the family of SFR Concept; a conforming and nonconforming 20-node hexahedral elements denoted as SFR20 and SFR20I, respectively. The proposed elements are based on the Space Fiber Rotation (SFR) concept. An appropriate Gaussian integration schemes were applied on the elements to evaluate the element matrices and vectors. Finally, the formulation of the incompatible element is presented in the last section.

3.2 Kinematics of the Space Fiber Rotation Concept

This section describes the kinematics of the proposed finite elements. All the elements presented in this work are developed based on the SFR concept. As depicted in Figure 3.1 this approach considers 3D rotation of a virtual fiber $\underline{iq}$. The fiber rotation represented by the vector $\underline{\theta}$ results in an additional displacement vector f which contribute to the definition of the final displacement field which is expressed as:

$$\underline{U}_q = \sum_{i=1}^{N_{node}} [\ N_i \underline{U}_i\ +\ f(\underline{\theta}_i, \underline{iq})\ ] \tag{3.1}$$

where N_{node} represent the number of nodes of the element (20-nodes for hexaheral), $\{\underline{U}_i\} = \{U_i V_i W_i\}^T$ are the parameters of the nodal displacement and N_i are the shape functions associated with the serendipity elements, further detail on the shape functions of the presented elements are presented in Annexes A.

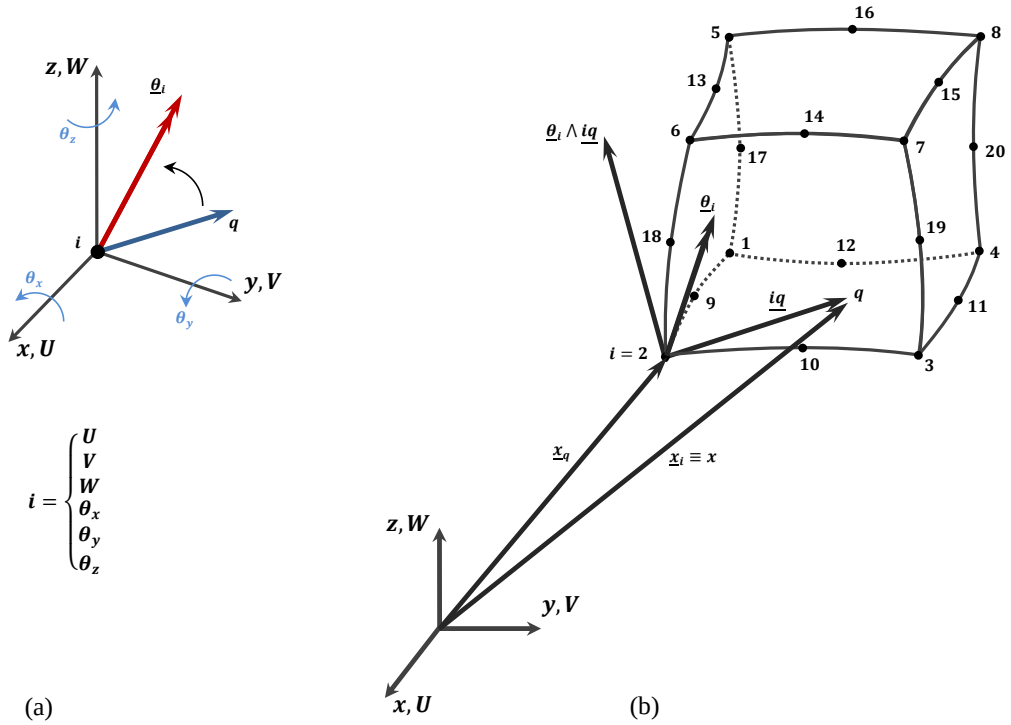

Figure 3.1: Application of the SFR concept on a 20-node hexahedral element: (a) Kinematics of the Space Fiber Rotation Concept and nodal variables, (b) Geometry and kinematic of SFR20 hexahedral element.

The additional displacement vector resulted from the rotation of the virtual fiber is given by:

$$f\left(\underline{\theta}_i, \underline{iq}\right) = N_i(\underline{\theta}_i \wedge \underline{iq}) \tag{3.2}$$

where:

$$\{iq\} = \{x_q - x_i\} = \left\{ \begin{array}{c} x - x_i \\ y - y_i \\ z - z_i \end{array} \right\} \quad ; \quad \{\theta_i\} = \left\{ \begin{array}{c} \theta_{xi} \\ \theta_{yi} \\ \theta_{zi} \end{array} \right\} \tag{3.3}$$

The global coordinates x, y and z are expressed in terms of nodal coordinates and shape function as :

$$x = \sum_{i=1}^{N_{node}} N_i \, x_i \quad ; \quad y = \sum_{i=1}^{N_{node}} N_i \, y_i \quad ; \quad z = \sum_{i=1}^{N_{node}} N_i \, z_i \tag{3.4}$$

Replacing Equation (3.2) in Equation (3.1) leads to the following improved expression of the displacement field $\underline{U}_q$ of q:

$$\underline{U}(\xi, \eta, \zeta) = \sum_{i=1}^{N_{node}} N_i(\xi, \eta, \zeta) \left(\underline{U}_i \; + \; \underline{\theta}_i \wedge \underline{iq} \right) \quad ; \quad \underline{U}_q \equiv \underline{U} \tag{3.5}$$

The SFR approximation adopted in Equation (3.5) does not affect in anyway the inter-element continuity condition of the displacement vector in case where $\underline{iq}$ vanishes when q coincides with the node i. By performing the vector product between the rotation vector $\underline{\theta}_i$ and the virtual fiber $\underline{iq}$, we obtain the following approximation of the displacement vector $\underline{U}$ (the Einstein summation convention on i is used):

$$\{U_q\} = \left\{ \begin{array}{c} U \\ V \\ W \end{array} \right\} = \left\{ \begin{array}{l} N_i \; U_i + \; N_i \; (z - z_i) \, \theta_{yi} - \; N_i (y - y_i) \theta_{zi} \\ N_i \; V_i + \; N_i \; (x - x_i) \, \theta_{zi} - \; N_i (z - z_i) \theta_{xi} \\ N_i \; W_i + \; N_i \; (y - y_i) \, \theta_{xi} - \; N_i (x - x_i) \theta_{yi} \end{array} \right\} \tag{3.6}$$

The approximation (3.6) can be expressed in a matrix form:

$$\{U_q\} = [N_q] \, \{U_n\} \quad ; \quad [N_q] = \left[\begin{array}{ccc} & \{N_{ui}\}^T & \\ \cdots & \{N_{vi}\}^T & \cdots \; i = 1, N_{node} \\ & \{N_{wi}\}^T & \end{array} \right] = \left[\begin{array}{c} \{N_u\}^T \\ \{N_v\}^T \\ \{N_w\}^T \end{array} \right] \tag{3.7}$$

where

$$\begin{array}{rcccccccc} \{N_{ui}\} & = & \{ & N_i & 0 & 0 & 0 & N_i(z - z_i) & -N_i(y - y_i) & \}^T \\ \{N_{vi}\} & = & \{ & 0 & N_i & 0 & -N_i(z - z_i) & 0 & N_i(x - x_i) & \}^T \\ \{N_{wi}\} & = & \{ & 0 & 0 & N_i & N_i(y - y_i) & -N_i(x - x_i) & 0 & \}^T \end{array} \tag{3.8}$$

and $\{U_n\}$ is the nodal DOFs vector containing 6 DOFs (three translations and three

rotations) per node.

$$\{U_n\} = \{\cdots \mid U_i \; V_i \; W_i \vdots \theta_{xi} \; \theta_{yi} \; \theta_{zi} \mid \cdots i = 1, N_{node}\}^T \tag{3.9}$$

From the standard displacement-based finite element functions, the strains of the element can be written as:

$$\{\varepsilon\} = \begin{Bmatrix} \varepsilon_x \\ \varepsilon_y \\ \varepsilon_z \\ \varepsilon_{xy} \\ \varepsilon_{xz} \\ \varepsilon_{yz} \end{Bmatrix} = \begin{Bmatrix} \frac{\partial u}{\partial x} \\ \frac{\partial v}{\partial y} \\ \frac{\partial w}{\partial z} \\ \frac{\partial u}{\partial y} + \frac{\partial v}{\partial x} \\ \frac{\partial u}{\partial z} + \frac{\partial w}{\partial x} \\ \frac{\partial v}{\partial z} + \frac{\partial w}{\partial y} \end{Bmatrix} = [B]\{U_n\} \tag{3.10}$$

Where $[B]$ is *the strain matrix* that connects both the displacement and the strain; and it can be obtained by deriving the shape functions expressed in (3.8).

$$[B] = [\partial]\{N_q\} \tag{3.11}$$

Where the matrix $[\partial]$ is the differential operator for 3D solids, given by:

$$[\partial] = \begin{bmatrix} \frac{\partial}{\partial x} & 0 & 0 & \frac{\partial}{\partial y} & \frac{\partial}{\partial z} & 0 \\ 0 & \frac{\partial}{\partial y} & 0 & \frac{\partial}{\partial x} & 0 & \frac{\partial}{\partial z} \\ 0 & 0 & \frac{\partial}{\partial z} & 0 & \frac{\partial}{\partial x} & \frac{\partial}{\partial y} \end{bmatrix}^T \tag{3.12}$$

The displacement-strain matrix became in the following form:

$$\underbrace{[B]}_{6\times DOFs} = \begin{bmatrix} \langle N_{u,x} \rangle \\ \langle N_{v,y} \rangle \\ \langle N_{w,z} \rangle \\ \langle N_{u,y} \rangle + \langle N_{v,x} \rangle \\ \langle N_{u,z} \rangle + \langle N_{w,x} \rangle \\ \langle N_{v,z} \rangle + \langle N_{w,y} \rangle \end{bmatrix} \tag{3.13}$$

The dimension of the $[B]$ matrix is six rows and the columns are equal to the number of DOFs, all the derivatives of the shape functions defining the strain matrix for the presented elements will be discussed in detail in the following sections.

$$\begin{array}{l} \{N_{\alpha,x}\} = j_{11}\{N_{\alpha,\xi}\} + j_{12}\{N_{\alpha,\eta}\} + j_{13}\{N_{\alpha,\zeta}\} \\ \{N_{\alpha,y}\} = j_{21}\{N_{\alpha,\xi}\} + j_{22}\{N_{\alpha,\eta}\} + j_{23}\{N_{\alpha,\zeta}\} \\ \{N_{\alpha,z}\} = j_{31}\{N_{\alpha,\xi}\} + j_{32}\{N_{\alpha,\eta}\} + j_{33}\{N_{\alpha,\zeta}\} \end{array} \qquad \alpha \equiv u, v, w \tag{3.14}$$

and j_{lk} are the Jacobian inverse matrix components $\left([j] = [J]^{-1}\right)$, so the Jacobian matrix

takes the following form:

$$[J] = \begin{bmatrix} x_{,\xi} & y_{,\xi} & z_{,\xi} \\ x_{,\eta} & y_{,\eta} & z_{,\eta} \\ x_{,\zeta} & y_{,\zeta} & z_{,\zeta} \end{bmatrix} \tag{3.15}$$

3.3 Linear modelling of the SFR20 element

The SFR20 represent the quadratic version of the hexahedral element SFR8 Ayad et al.[45], unlike the SFR8 the SFR20 has 20-node and they are located at the vertices and in the middle of the edges. The additional node in the middle of the edges gives the advantage to the element to simulate curved boundaries, and the higher order element are usually well behaved. The element was developed based on the Space Fiber Rotation (SFR) concept as depicted in Figure 3.2. This approach as stated before; considers the 3D rotation of a virtual fiber $\underline{iq}$. The fiber roation represented by vector $\underline{\theta}$ results in an additional displacement vector f which contributes to the definition of the final displacement field as follows:

$$\underline{U}(\xi,\eta,\zeta) = \sum_{i=1}^{20} N_i(\xi,\eta,\zeta)\left(\underline{U}_i \; + \; \underline{\theta}_i \wedge \underline{iq}\right) \quad ; \quad \underline{U}_q \equiv \underline{U} \tag{3.16}$$

where $\{\underline{U}_i\} = \{U_i V_i W_i\}^T$ are the parameters of the nodal displacement and N_i are the shape functions associated with the serendipity 20-node hexahedral element, which can be expressed as:

$$\begin{gathered} N_i = \tfrac{1}{8}(-2+\xi_i\xi+\eta_i\eta+\zeta_i\zeta)(1+\xi_i\xi)(1+\eta_i\eta)(1+\zeta_i\zeta) \quad \text{with} \quad i = 1,3,5,7,13,15,17,19 \\ N_i = \tfrac{1}{4}(1-\xi^2)(1+\eta_i\eta)(1+\zeta_i\zeta) \quad \text{with} \quad i = 2,6,14,18 \\ N_i = \tfrac{1}{4}(1+\xi_i\xi)(1-\eta^2)(1+\zeta_i\zeta) \quad \text{with} \quad i = 4,8,16,20 \\ N_i = \tfrac{1}{4}(1+\xi_i\xi)(1+\eta_i\eta)(1-\zeta^2) \quad \text{with} \quad i = 9,10,11,12 \\ \text{where} \quad -1 \le \xi,\eta,\zeta \le +1 \end{gathered} \tag{3.17}$$

Further detailes on the shape function, their derivatives and node coordinates are presented in Appendix A.

The global coordinates x, y and z of the SFR20 element are expressed in terms of nodal coordinates and shape function as :

$$x = \sum_{i=1}^{20} N_i\,(\xi,\eta,\zeta)\; x_i \quad ; \quad y = \sum_{i=1}^{20} N_i\,(\xi,\eta,\zeta)\; y_i \quad ; \quad z = \sum_{i=1}^{20} N_i\,(\xi,\eta,\zeta)\; z_i \tag{3.18}$$

Using Eqs (3.7), (3.10), (3.11) and (3.17). The strain matrix for the SFR20 hexahedral element can be easily obtained to have the following form:

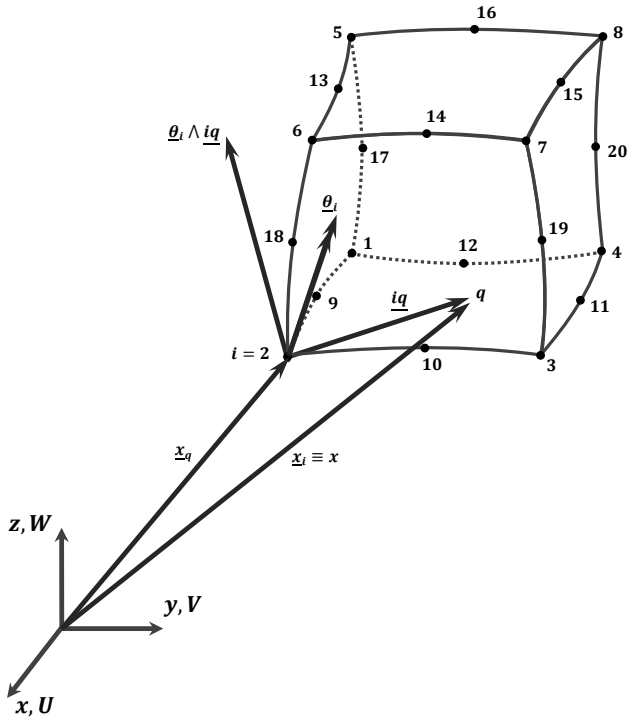

Figure 3.2: Geometry and kinematics of the SFR20 element.

$$[B] = \begin{bmatrix} & N_{i,x} & 0 & 0 & 0 & N_{i,x}(z-z_i) & -N_{i,x}(y-y_i) & \\ & 0 & N_{i,y} & 0 & -N_{i,y}(z-z_i) & 0 & N_{i,y}(x-x_i) & \\ & 0 & 0 & N_{i,z} & N_{i,z}(y-y_i) & N_{i,x}(x-x_i) & 0 & \\ ... & N_{i,y} & N_{i,x} & 0 & -N_{i,x}(z-z_i) & N_{i,y}(z-z_i) & B_{4,i} & ...i = 1,20 \\ & N_{i,z} & 0 & N_{i,x} & N_{i,x}(y-y_i) & B_{5,i} & -N_{i,z}(y-y_i) & \\ & 0 & N_{i,z} & N_{i,y} & B_{6,i} & -N_{i,y}(x-x_i) & -N_{i,z}(x-x_i) & \end{bmatrix} \tag{3.19}$$

Where

$$\begin{cases} B_{4,i} = N_{i,x}(x-x_i) - N_{i,y}(y-y_i) \\ B_{5,i} = N_{i,z}(z-z_i) - N_{i,x}(x-x_i) \qquad i = 1,20 \\ B_{6,i} = N_{i,y}(y-y_i) - N_{i,z}(z-z_i) \end{cases} \tag{3.20}$$

The strain matrix $[B]$ is of a dimension 6×120 for the SFR20 element and the derivatives of the shape functions can be obtained using the following operation:

$$\begin{Bmatrix} \frac{\partial N_i}{\partial x} \\ \frac{\partial N_i}{\partial y} \\ \frac{\partial N_i}{\partial z} \end{Bmatrix} = \begin{bmatrix} \frac{\partial \xi}{\partial x} & \frac{\partial \eta}{\partial x} & \frac{\partial \zeta}{\partial x} \\ \frac{\partial \xi}{\partial y} & \frac{\partial \eta}{\partial y} & \frac{\partial \zeta}{\partial y} \\ \frac{\partial \xi}{\partial z} & \frac{\partial \eta}{\partial z} & \frac{\partial \zeta}{\partial z} \end{bmatrix} \cdot \begin{Bmatrix} \frac{\partial N_i}{\partial \xi} \\ \frac{\partial N_i}{\partial \eta} \\ \frac{\partial N_i}{\partial \zeta} \end{Bmatrix} = [J]^{-1} \begin{Bmatrix} \frac{\partial N_i}{\partial \xi} \\ \frac{\partial N_i}{\partial \eta} \\ \frac{\partial N_i}{\partial \zeta} \end{Bmatrix} \tag{3.21}$$

3.4 Formulation of the Incompatible SFR20I element

In this section we present the nonconforming version of the SFR20 element denoted as SFR20I. The element uses a similar approach as given by Yunus et al. [39] and Ayad et al. [45] to avoid some shortcomings related to the Poisson locking phenomena. In this regard, three incompatible displacement modes at the element level are introduced in the natural space. The natural space extra modes are given as follows:

$$\begin{cases} U^{NC} = (1-\xi^2)\, a_u \\ V^{NC} = (1-\eta^2)\, a_v \\ W^{NC} = (1-\zeta^2)\, a_w \end{cases} \tag{3.22}$$

where NC stands for Non-Conforming, a_u, a_v and a_w are the scale factors.

Natural or covariant non-conforming strains are determined by:

$$\varepsilon_{\xi\xi}^{NC} = \frac{\partial U^{NC}}{\partial \xi} \quad ; \quad \varepsilon_{\eta\eta}^{NC} = \frac{\partial V^{NC}}{\partial \eta} \quad ; \quad \varepsilon_{\zeta\zeta}^{NC} = \frac{\partial W^{NC}}{\partial \zeta} \quad ; \quad \gamma_{\xi\eta}^{NC} = \gamma_{\xi\zeta}^{NC} = \gamma_{\eta\zeta}^{NC} = 0 \tag{3.23}$$

The vector of natural strains is related to the scale factors a_u , a_v and a_w through a matrix $[M]$ as:

$$\varepsilon_{\xi}^{NC} = [M]\,\{a\} \tag{3.24}$$

$$\begin{Bmatrix} \varepsilon_{\xi\xi}^{NC} \\ \varepsilon_{\eta\eta}^{NC} \\ \varepsilon_{\zeta\zeta}^{NC} \\ \gamma_{\xi\eta}^{NC} \\ \gamma_{\xi\zeta}^{NC} \\ \gamma_{\eta\zeta}^{NC} \end{Bmatrix} = \begin{bmatrix} -2\,\xi & 0 & 0 \\ 0 & -2\,\eta & 0 \\ 0 & 0 & -2\,\zeta \\ 0 & 0 & 0 \\ 0 & 0 & 0 \\ 0 & 0 & 0 \end{bmatrix} \begin{Bmatrix} a_u \\ a_v \\ a_w \end{Bmatrix} \tag{3.25}$$

In order to verify the orthogonality condition between constant stress and non-conforming strain vectors (ensuring the satisfaction of the patch test); we consider the following relationship between Cartesian and natural non-conforming strains:

$$\{\varepsilon_X^{NC}\} = \frac{\det J_0}{\det J}\,[T_0]\,\{\varepsilon_{\xi}^{NC}\} = \frac{\det J_0}{\det J}\,[T_0]\,[M]\,\{a\} \tag{3.26}$$

$$\left[M^{NC}\right] = \frac{\det J_0}{\det J}\,[T_0]\,[M] \tag{3.27}$$

where $[T_0]$ is the matrix relating Cartesian and covariant strain vectors evaluated at the element center and $detJ$ is the determinant of the Jacobian ($detJ_0$ is evaluated at the center of the element). The introduction of incompatible modes conduces to an enhanced

strain vector :

$$\{\varepsilon^E\} = \{\varepsilon\} + \{\varepsilon^{NC}\} = [B]\{U_n\} + [M^{NC}]\{a\} \tag{3.28}$$

By replacing the new incompatible strain vector $\{\varepsilon^E\}$ in the equilibrium weak form Equation (2.61), we obtain the following system of Equations:

$$\begin{bmatrix} [K^e_{uu}] & [K^e_{ua}] \\ [K^e_{au}] & [K^e_{aa}] \end{bmatrix} \begin{Bmatrix} \{U_n\} \\ \{a\} \end{Bmatrix} = \begin{Bmatrix} \{f^e_{ext}\} \\ 0 \end{Bmatrix} \tag{3.29}$$

$$[K^e]^{NC}\{U_n\}^{NC} = \{F^e_{ext}\}^{NC} \tag{3.30}$$

where the stiffness matrix $[K^e]^{NC}$ is defined by the following matrices:

$$[K^e_{uu}] = \int_{V^e} [B]^T [C][B] \; dV^e \tag{3.31}$$

$$[K^e_{ua}] = \int_{V^e} [B]^T [C]\left[M^{NC}\right] \; dV^e \tag{3.32}$$

$$[K^e_{au}] = \; [K^e_{ua}]^T \tag{3.33}$$

$$[K^e_{aa}] = \int_{V^e} \left[M^{NC}\right]^T [C]\left[M^{NC}\right] \; dV^e \tag{3.34}$$

Static condensation of the tangent matrix is performed to eliminate the unknown enhanced parameters a at element level and thus the final element stiffness matrix of SFR20I is given as :

$$[K^e]^{NC} = [K^e_{uu}] - [K^e_{ua}][K^e_{aa}]^{-1}[K^e_{au}] \tag{3.35}$$

3.5 Numerical integration over SFR20 and SFR20I elements

The analytical integration of Equation (2.69) and (2.70) frequently are not feasible to solve where large number of elements. Hence, huge number of integrations are required. Instead, we often use a numerical integration techniques, and the most used one is the *Guassian Integration schema* or *Gaussian Quadrature*. Guassian quadrature states that the integral is evaluated simply by a summation of the integrand evaluated at *Guass points* multiplied by corresponding *Wieght Coefficients* as follows:

$$\int_{\Omega^e} f(x,y,z)dxdydz = \int_{\Omega^{local}} f(\xi,\eta,\zeta)\, DetJ d\xi d\eta d\zeta \tag{3.36}$$

The Gauss integration is sampled in three dimensions by a series of linear functions at specific location, as follows:

$$\int_{\Omega^e} f(\xi,\eta,\zeta)\, DetJ d\xi d\eta d\zeta = \sum_{i=1}^{m}\sum_{j=1}^{m}\sum_{k=1}^{m} f(\xi_i,\eta_j,\zeta_k)\, DetJ(\xi_i,\eta_j,\zeta_k)\, w_i w_j w_k \tag{3.37}$$

Where $DetJ$ is the Jacobian determinant, GP is the number of Gauss points in the element, where $GP = m^3$ and m is the number of Gauss points in the direction of ξ, η and ζ. ξ_i, η_j and ζ_k are the parametric coefficients. w_i, w_j and w_k are the Wieght Coefficients.

The Gaussian integration on the reference element is necessary to obtain the element stiffness matrix. Different numerical integration scheme for hexahedral elements are indicated in Table 3.1. A reduced integration scheme with $3 \times 3 \times 3$ Gauss points is needed to determine the stiffness matrix part of the SFR20 element corresponding to the displacement DOFs. The stabilisation method used for both elements is the same that was used in the work of Ayad et al. [45].

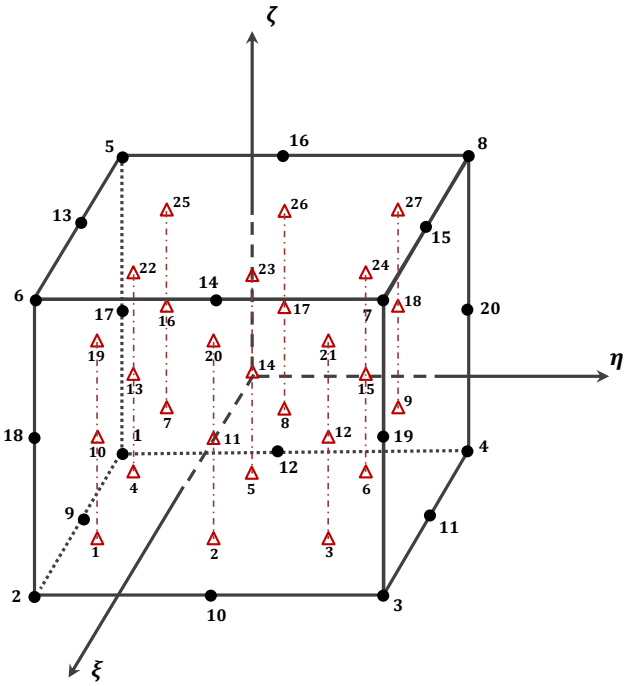

Figure 3.3: The SFR20 element in local reference with $3 \times 3 \times 3$ integration points.

Once the shape functions $[N_i]$ and the strain matrix $[B]$ are defined, add to that the appropriate numerical integration scheme for the proposed element is chosen we proceed

to evaluate the element matrices and vectors; the element stiffness matrix $[K^e]$ and the external nodal force vector $\{F^e_{ext}\}$. By applying the numerical integration on Equations (2.69) and (2.70), the element stiffness matrix $[K^e]$ and the external force vector $\{F^e_{ext}\}$ of the SFR20 element are expressed as follows:

Table 3.1: Location of the integration points in hexahedral elements.

Orders	**Integration scheme**	**Coordinates** (ξ_i, η_i, ζ_i)	**Number of points**	**Weight coefficients** w_i
Linear	$1 \times 1 \times 1$	$(0,0,0)$	1	8
Quadratic	$2 \times 2 \times 2$	$\left(\pm\frac{1}{\sqrt{3}}, \pm\frac{1}{\sqrt{3}}, \pm\frac{1}{\sqrt{3}}\right)$	8	1
Cubic	$3 \times 3 \times 3$	$\left(\pm\sqrt{\frac{3}{5}}, \pm\sqrt{\frac{3}{5}}, \pm\sqrt{\frac{3}{5}}\right)$	8	$\left(\frac{5}{9}\right)^3$
		$\left(0, \pm\sqrt{\frac{3}{5}}, \pm\sqrt{\frac{3}{5}}\right)$ $\left(\pm\sqrt{\frac{3}{5}}, 0, \pm\sqrt{\frac{3}{5}}\right)$ $\left(\pm\sqrt{\frac{3}{5}}, \pm\sqrt{\frac{3}{5}}, 0\right)$	12	$\left(\frac{8}{9}\right)\left(\frac{5}{9}\right)^2$
		$\left(0, 0, \pm\sqrt{\frac{3}{5}}\right)$	6	$\left(\frac{8}{9}\right)^2\left(\frac{5}{9}\right)$
		$(0,0,0)$	1	$(\frac{8}{9})^3$
Quartic	$4 \times 4 \times 4$	$\pm\sqrt{\frac{3}{7} + \frac{2}{7}\sqrt{\frac{6}{5}}}$	32	$\frac{18-\sqrt{30}}{36}$
		$\pm\sqrt{\frac{3}{7} - \frac{2}{7}\sqrt{\frac{6}{5}}}$	32	$\frac{18+\sqrt{30}}{36}$

$$[K^e] = \int_{V^e} [B]^T [C] [B] \, dV^e = \int_{-1}^{1}\int_{-1}^{1}\int_{-1}^{1} \left([B]^T [C] [B] \, DetJ\right)_{\xi,\eta,\zeta} d\xi d\eta d\zeta$$
$$= \sum_{i=1}^{3}\sum_{j=1}^{3}\sum_{k=1}^{3} w_i w_j w_k \left([B]^T [C] [B] \, DetJ\right)_{\xi_i,\eta_i,\zeta_i} \quad (3.38)$$

$$\{F^e_{ext}\} = \sum_{i=1}^{3}\sum_{j=1}^{3}\sum_{k=1}^{3} w_i w_j w_k \left([N_q]^T \{f_v\} \, DetJ\right)_{\xi_i,\eta_i,\zeta_i} + \sum_{i=1}^{3}\sum_{j=1}^{3} w_i w_j \left([N_q]^T \{T\} \, DetJ\right)_{\xi_i,\eta_i} \quad (3.39)$$

The numerical integration scheme used to define the stiffness matrix $[K^e]^{NC}$ of the SFR20I element is a $3 \times 3 \times 3$ integration points; Integration points and weights are presented in Table 3.1. The stiffness matrix of the SFR20I requires to define all the matrices $[K^e_{uu}]$, $[K^e_{ua}]$, $[K^e_{au}]$ and $[K^e_{aa}]$ in the following manner:

$$[K^e_{uu}] = \int_{V^e} [B]^T [C] [B] \, dV^e = \sum_{i=1}^{3} \sum_{j=1}^{3} \sum_{k=1}^{3} w_i w_j w_k \left([B]^T [C] [B] \, DetJ \right)_{\xi_i, \eta_i, \zeta_i} \tag{3.40}$$

$$[K^e_{ua}] = \int_{V^e} [B]^T [C] \left[M^{NC} \right] dV^e = \sum_{i=1}^{3} \sum_{j=1}^{3} \sum_{k=1}^{3} w_i w_j w_k \left([B]^T [C] \left[M^{NC} \right] DetJ \right)_{\xi_i, \eta_i, \zeta_i} \tag{3.41}$$

$$[K^e_{aa}] = \int_{V^e} \left[M^{NC} \right]^T [C] \left[M^{NC} \right] dV^e = \sum_{i=1}^{3} \sum_{j=1}^{3} \sum_{k=1}^{3} w_i w_j w_k \left(\left[M^{NC} \right]^T [C] \left[M^{NC} \right] DetJ \right)_{\xi_i, \eta_i, \zeta_i} \tag{3.42}$$

Chapter 4

Numerical validation of the SFR elements for 3D elasticity problems

Summary

4.1 Introduction

In this chapter, the performance and efficiency of the proposed elements is evaluated through a series of 3D benchmarks. In this context, the obtained results are compared with the analytical solution on the one hand and with those of other reference elements on the other hand Table 4.1. Computations are performed using the finite element code Reflex developed by Batoz and Dhatt [18] where the proposed elements are implemented in the form of subroutines; that calculates the element stiffness matrix. The proposed elements are exposed to a range of different type of structures (beams, plates and shells) and tests; distortion tests, aspect ratio test and convergence tests. Finally, in order to investigate the computational time coast of the proposed elements; the elapsed time required to calculate the element stiffness matrices is performed and compared with other reference elements.

Table 4.1: Listing of abbreviations to denote the element types.

Name	Description
HEX20	20-node hexahedral standard element tested by MacNeal and Harder [19];
HEX20(R)	20-node hexahedral standard element with reduced order integration tested by MacNeal and Harder in [19];
SHB20	20-node solid-shell element [84];
C3D20	20-node second-order classical hexahedral Abaqus element with an exact numerical integration scheme ($3 \times 3 \times 3$ Gauss points) [85];
C3D20R	20-node second-order classical hexahedral Abaqus element with reduced numerical integration scheme ($2 \times 2 \times 2$ Gauss points) [85];
SOLID95	20-node element of ANSYS 5.4 [86];
HEXA20	20-node isoparametric hexahedron classical symmetric element [54];
US-HEXA20	20-node Unsymmetric hexahedral element [54];
H27	27-node Lagrange element [5, 87];
HS21	21-node hexahedral spline element [56];
SFR20	Presented 20-node hexahedral element based upon the "Space Fiber Rotation" concept;
SFR20I	Presented 20-node hexahedral element based upon the "Space Fiber Rotation" concept with incompatible modes.

4.2 Distortion tests

In the next four tests the presented elements and other elements from the litirature are tested for their sensitivity to mesh distortion. A straight cantilever beam is considered with the following dimensions; Length $L = 10$, width $b = 1$ and thickness $t = 0.1$. The mechanical properties are; Young Modulus $E = 10^7$ and Poisson's ration $\nu = 0.0$. The beam is fixed in one end and a tip moment with an amplitude $M = 1$ is applied at the free end. The displasment of the free end tip is investigated. Following these four tests a well known benchmark test proposed by Cheung and Chen [88] is assessed to investigate the performance of the proposed elements for their sensitivity to mesh distortion.

4.2.1 Mid-node distortion

The beam is modeled using one single element as shown in Figure 4.1. The presented elements are tested for their sensitivity to mid-node distortion as described by Nagarayana and Prathap [89]. The mid-nodes are displaced by a distance along the length of the cantilever beam in the range $\Delta_m = 0.0 - 2.5$. The normalized deflection of the mid-nodes are tabulated in Table 4.2.

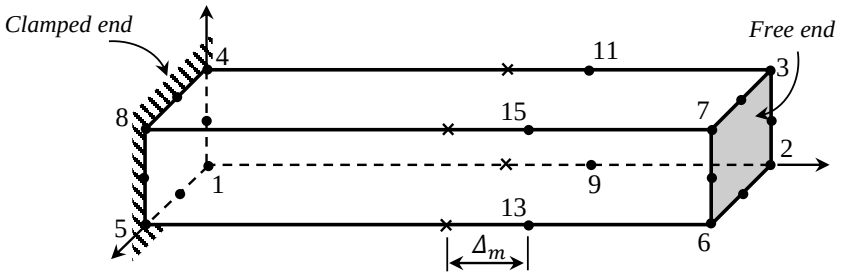

Figure 4.1: Cantilever beam modeled with one element for Mid-node distortion test. The mid-nodes are displaced with the parameter Δ_m.

Table 4.2: Normalized displacements of the free end for mid-node distortion sensitivity test.

$W^{Ref} = 0.4$ [89]					
Element	$\Delta_m = 0.0$	$\Delta_m = 0.1$	$\Delta_m = 0.5$	$\Delta_m = 1.0$	$\Delta_m = 2.5$
HEX20 [19]	0.750300	0.688250	0.428025	0.176990	0.000308
C3D20 [85]	0.750304	0.688259	0.428016	0.176991	0.000308
SFR20	1.00005	0.999825	0.994075	0.976075	0.850075
SFR20I	1.00005	0.999825	0.994075	0.976075	0.850075

As can be seen in Table 4.2, the performance of the presented elements exhibits favourable results with very slight sensitivity to distortion unlike the isoparametric elements which appear their performance deteriorate fast with increase in distortion parameter Δ_m.

4.2.2 Plane distortion

This test was proposed by Nagarayana and Prathap [89] to test the elements for their sensitivity for plan distortion. The cantilever beam is modelled using two hexhadral elements along the length. The parameter Δ_p represent the tilt of the plane Figure 4.2, and it varies in the range $\Delta_p = 0.0 - 2.5$. Normalized deflection of the free end are summarized in Table 4.3. The results indicates that the elements SFR20 and SFR20I are the most resistant to plan distortion, while the other elements deteriorates fast with increase of the parameter Δ_p.

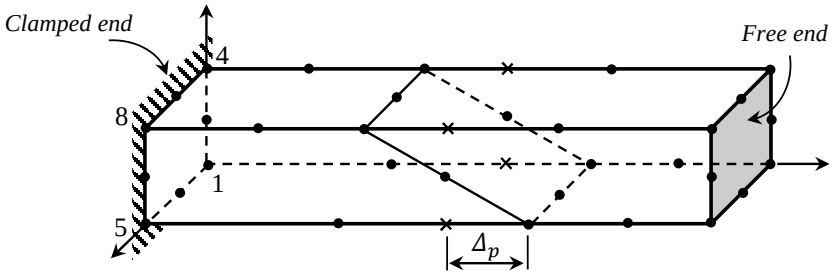

Figure 4.2: Cantilever beam modelled with two hexahedral elements for Plane distortion test. The corner mid-face nodes are displaced with the parameter Δ_p.

Table 4.3: Normalized displacements of the free end for plane-node distortion sensitivity test.

$W^{Ref} = 0.4$ [89]					
Element	$\Delta_p = 0.0$	$\Delta_p = 0.1$	$\Delta_p = 0.5$	$\Delta_p = 1.0$	$\Delta_p = 2.5$
HEX20	0.937800	0.691925	0.009081	0.001359	0.000791
C3D20	0.937807	0.691915	0.009081	0.001358	0.000791
SFR20	1.000075	0.982700	0.816050	0.770425	0.752750
SFR20I	1.000075	1.027225	0.827900	0.774275	0.752975

4.2.3 Curved face distortion

The cantilever beam shown in Figure (4.3) is modelled with two hexahedral elements. This test was conducted by Ooi et al. [54] to measure the curved face distortion of the elements.

The parameter Δ_b express the displacement of two mid-side nodes at the element interface over a range of $\Delta_b = 0.0 - 2.5$. Table 4.4 summarize the normalized deflection of the free end of the cantilever beam and it shows the sensitivity of the elements to warping test. The present elements present favourable behaviour with a slight sensitivity to mesh distortion unlike the other elements.

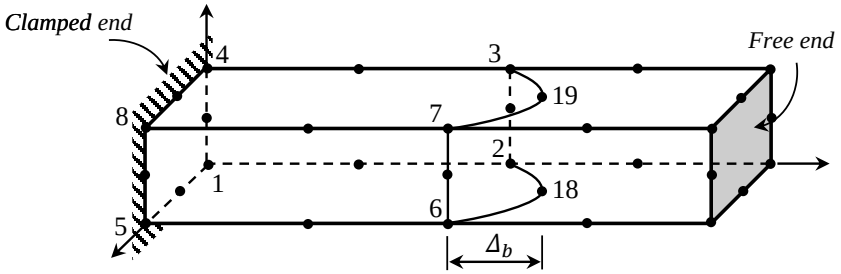

Figure 4.3: Cantilever beam modelled with two hexahedral elements for Curved face distortion test. The nodes 18 and 19 are displaced with the parameter Δ_b.

Table 4.4: Normalized displacements of the free end for curved face distortion sensitivity test.

$W^{Ref} = 0.4$ [54]					
Element	$\Delta_p = 0.0$	$\Delta_p = 0.1$	$\Delta_p = 0.5$	$\Delta_p = 1.0$	$\Delta_p = 2.5$
HEX20	0.937800	0.624325	0.064475	0.014793	0.001774
C3D20	0.937807	0.624321	0.064474	0.014793	0.001774
SFR20	1.000075	0.998900	0.969850	0.912800	0.831275
SFR20I	1.000075	0.998900	0.969850	0.912800	0.831275

4.2.4 Warping test

The cantilever beam is modelled with two hexahedral elements Figure (4.4), this test was also conducted by Ooi et al. [54] to test the elements performance for their sensitivity for warping. The parameter Δ_w represent the variation of the warping concentration in the range $\Delta_w = 0.0 - 2.5$. The performance of the proposed elements is observed in Table 4.5 where it summarizes the normalised results for the warping test. It can be noted that the elements SFR20 and SFR20I are not effected by the warping unlike the other elements which show notable sensitivity.

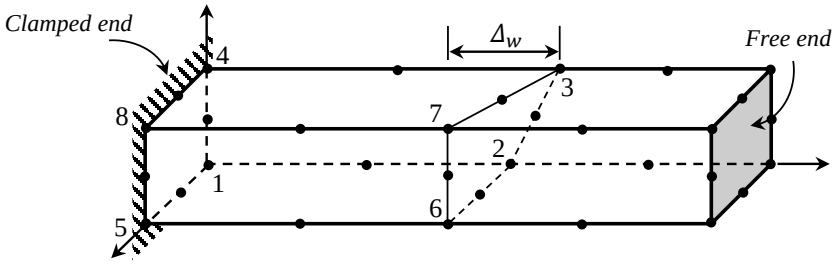

Figure 4.4: Cantilever beam modelled with two hexahedral elements for Warping test. The node 3 is displaced with the parameter Δ_w.

Table 4.5: Normalized displacements of the free end for warping distortion sensitivity test.

$W^{Ref} = 0.4$ [54]					
Element	$\Delta_p = 0.0$	$\Delta_p = 0.1$	$\Delta_p = 0.5$	$\Delta_p = 1.0$	$\Delta_p = 2.5$
HEX20	0.937800	0.901625	0.278775	0.027735	0.0017089
C3D20	0.937807	0.901625	0.278763	0.027728	0.001706
SFR20	1.000075	0.995975	0.933275	0.862375	0.780125
SFR20I	1.000075	1.023825	0.958100	0.872775	0.782750

4.2.5 Cheung and Chen tests

The test was introduced to study the effect of geometric distortions on the accuracy of results and to observe the stress fields distribution Cheung and Chen [88]. Figure 4.5 demonstrate the geometry, mechanical properties and boundary condition of the problem. The beam is discretized with five different sets of distorted mesh.

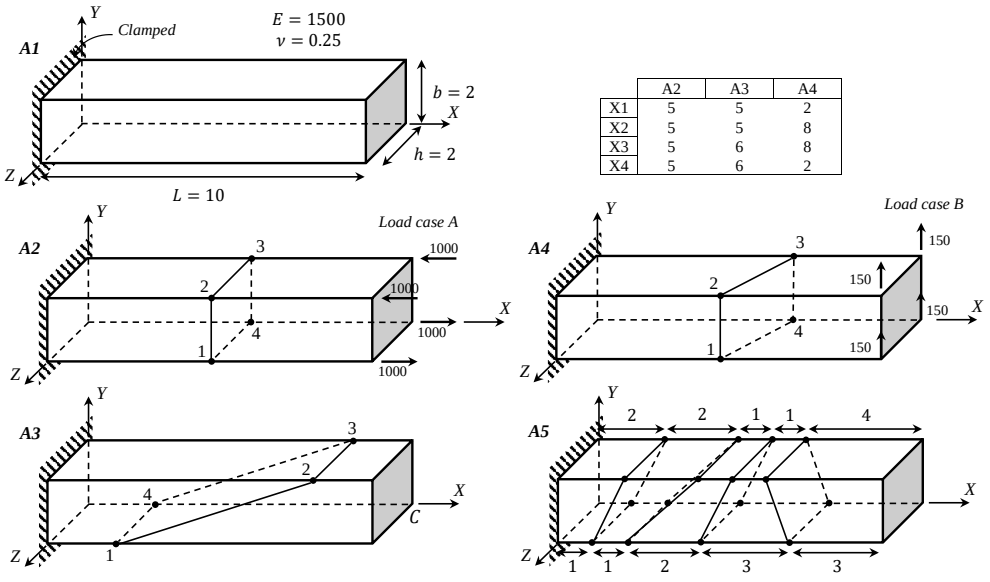

	A2	A3	A4
X1	5	5	2
X2	5	5	8
X3	5	6	8
X4	5	6	2

Figure 4.5: Geometry, mechanical properties, load distribution and five different mesh sets for Cheung and Chen tests.

All sets are clamped and subjected to two case of loading in the free end; a pure bending case **A** and transverse/shear force case **B**. The reference transverse displacements of the free end tip for case **A** and **B** are $W_C^{Ref} = 100$, $W_C^{Ref} = 102.6$, respectively. We summarize in Tables 4.6 the normalized transverse displacement.

Table 4.6: Normalised transverse displacement at tip for different Sets.

Mesh	SOLID95	USHEXA20	C3D20	SFR20	SFR20I
Load case A			$W_C^{Ref} = 100$ [88]		
A1	1.000000	1.000000	0.953272	0.98707	1.00510
A2	1.000000	1.000000	0.964689	0.97592	0.99612
A3	0.999858	1.000000	0.962730	0.98088	0.99991
A4	0.665333	1.000000	0.515490	0.97888	0.98292
A5	0.997209	1.000000	0.972750	0.99533	1.01250
Load case B			$W_C^{Ref} = 102.6$ [88]		
A1	0.839201	0.839038	0,792997	0.960964	0.989474
A2	0.983236	0.982114	0.931034	0.967914	0.992105
A3	0.978002	0.977721	0.924849	0.967583	0.991618
A4	0.618807	0.541773	0.488958	0.924395	0.968479
A5	1.005029	1.004382	0.972462	0.990351	1.006628

We notice for all sets the presented elements exhibits favourable results, however, the element SFR20 results are less accurate than the other elements except for the element C3D20. It is clear that the SFR20I converge faster than the SFR20 and its results are the most accurate beside the element US-HEXA20.

4.3 Maximum aspect ratio test

This test was examined in the works of Legay and Combescure [90] and Abed Meraim et al. [84] to evaluate the aspect ratio limits of elements in beam bending problems. It consists of a clamped beam subjected to a bending load at its free edge as depicted in Figure 4.6. The analytical solution of this problem can be obtained using the Timoshenko beam theory [91] Equation (4.1):

$$Y^{Ref} = PL^3/3EI \quad ; \quad I = bt^3/12 \tag{4.1}$$

The length and the width of the beam were constant and equal to $L = 100$ and $b = 10$, respectively. The beam was modeled with one element through the thickness and

the width, in the length of the beam 10 elements were used in both regular and irregular meshes, the aspect ratio between the width and the thickness is $r = b/t$. The mechanical properties of the beam are: $E = 68.25 \times 10^6$ and $\nu = 0.3$. A bending load $P = 4$ is applied at the free end of the beam.

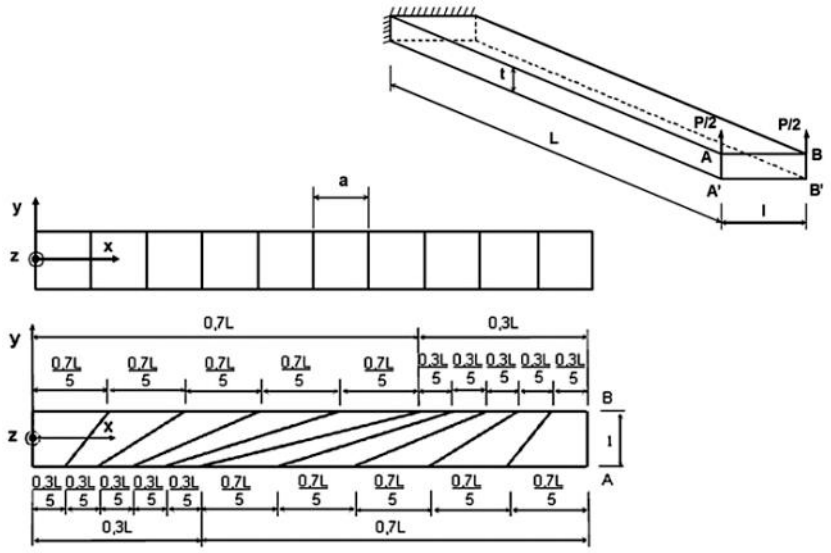

Figure 4.6: Cantilever beam geometry and mesh description.

Table 4.7: Normalized displacement at point A for the regular mesh.

$r = b/t$	**Analytical Solutions**	**HEX20**	**SHB20**	**SFR20**	**SFR20I**
1	2.344×10^{-5}	1.005	1.009	0.993	1.005
10	2.344×10^{-4}	0.984	0.998	0.999	1.009
100	2.344×10^{-3}	0.951	0.997	1.001	1.010
200	4.689×10^{-3}	0.959	0.996	1.001	1.010
333	7.814×10^{-3}	NA	0.998	1.001	1.010
500	1.172×10^{-2}	NA	1.004	1.001	1.010

Tables 4.7 and 4.8 present the displacement results at point A for various elements, encompassing both regular and irregular (distorted) meshes. The outcomes of the proposed elements and the solid-shell element SHB20 consistently align well with the analytical solution, even as the thickness diminishes. However, the standard hexahedron HEX20 exhibits a decline in accuracy as the aspect ratio increases, particularly evident in the case of the distorted mesh. Visual representations of the normalized displacement concerning the evolution of aspect ratio for both regular and irregular meshes are depicted in Figures 4.7 and 4.8, respectively.

Table 4.8: Normalized displacement at point A for the irregular (distorted) mesh.

$r = b/t$	**Analytical Solutions**	**HEX20**	**SHB20**	**SFR20**	**SFR20I**
1	2.344×10^{-5}	0.981	1.010	0.982	0.994
10	2.344×10^{-4}	0.682	0.997	0.988	0.998
100	2.344×10^{-3}	0.345	0.995	0.989	0.999
200	4.689×10^{-3}	0.294	1.002	0.989	0.999
333	7.814×10^{-3}	0.251	0.984	0.989	0.999
500	1.172×10^{-2}	NA	NA	0.989	0.999

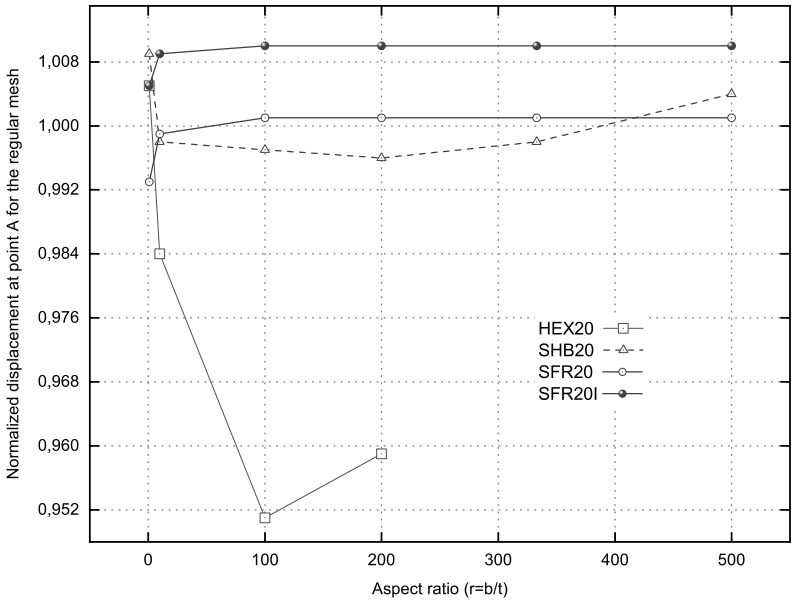

Figure 4.7: Convergence of normalized displacement at point A as a function of the aspect ration for regular mesh.

4.4 In-plane bending of a cantilever beam

As shown in Figure 4.9, the second numerical example considers a cantilever beam subjected to in plane bending load $P_y = 1.0 \times 10^4$. The beam is supposed to have the following physical properties: $E = 1.0 \times 10^7$, $\nu = 0.3$. This cantilever beam is modeled with six meshes: three regular meshes : M1, M2 and M3 and three distorted ones : M4, M5 and, M6 as shown in Figure 4.10. The reference solution of the transverse displacement at point C can be obtained using the Timoshenko beam theory [91] Equation (4.2):

$$V_C = \frac{PL^3}{3EI} + \frac{6PL}{5GA} = 4 + 0.03 = 4.03 \tag{4.2}$$

The outcomes of various solutions are presented in Table 4.9. This table contrasts the normalized displacement at point C for the proposed elements with the outcomes of Abaqus C3D20; a quadratic hexahedral element. Both SFR20 and SFR20I exhibit

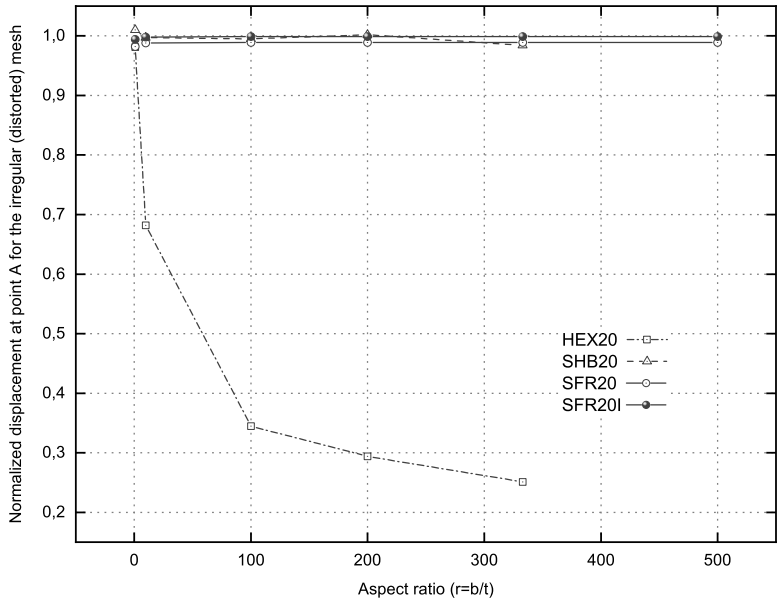

Figure 4.8: Convergence of normalized displacement at point A as a function of the aspect ration for irregular (distorted) mesh.

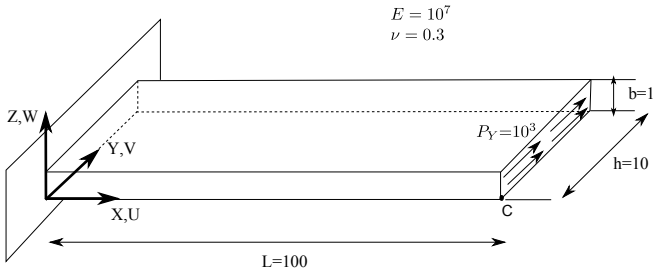

Figure 4.9: Geometry and mechanical properties of a thin cantilever beam under plane bending.

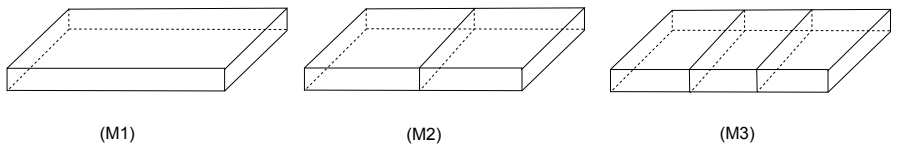

(a) Regular meshes.

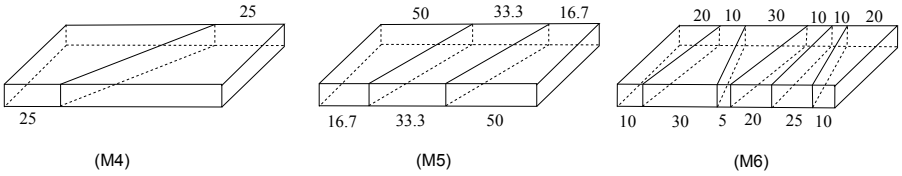

(b) Distorted meshes.

Figure 4.10: Mesh types of the thin cantilever beam.

favourable behaviour and a commendable rate of convergence. Notably, this is observed in the case of the distorted mesh, distinguishing them from the performance of the C3D20

element.

Table 4.9: In-plane bending of a cantilever beam. Normalized transverse displacement of point C (the quantity inside parentheses indicates the total number of variables in the model: DOFs plus internal variables).

$V_C = 4.03$						
Mesh Shape	**M1**	**M2**	**M3**	**M4**	**M5**	**M6**
C3D20	0.735	0.899	0.972	0.146	0.424	0.859
	(60)	(96)	(132)	(96)	(132)	(240)
SFR20	0.966	0.977	0.981	0.887	0.948	0.988
	(120)	(192)	(264)	(192)	(264)	(480)
SFR20I	0.998	0.999	0.999	0.907	0.957	1.012
	(123)	(198)	(273)	(198)	(273)	(498)

4.5 Straight cantilever beam

To evaluate the proposed elements' performance in terms of sensitivity to mesh distortion, a straight cantilever beam is considered. This example was examined in the work of MacNeal and Harder [19] to test the combination of different shapes with linearly varying strains.

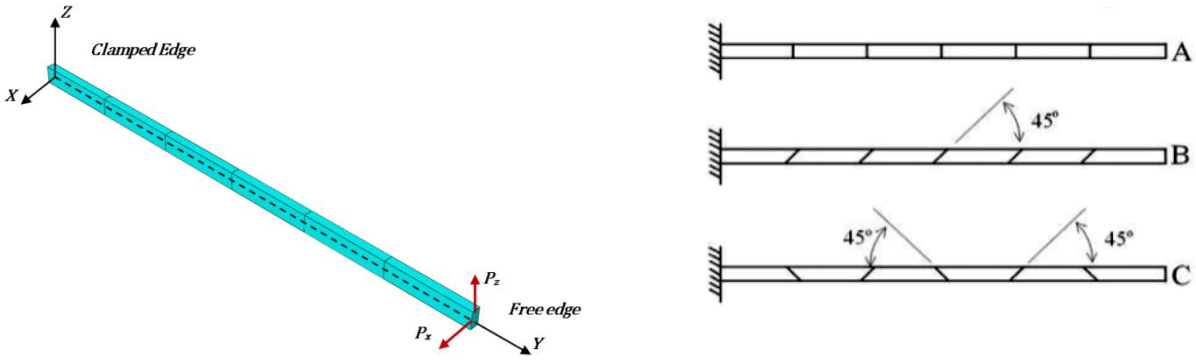

Figure 4.11: Straight cantilever beam with three types of meshes: rectangular (A); parallelogram (B) and trapezoidal (C).

In this respect, The beam is meshed with six elements with different shapes (regular bricks, trapezoidal and parallelogram-shaped) and subjected to an in-plane and out-of-plane unit-shear force at the free end as shown in Figure 4.11. The dimensions of the problem and the physical properties are: $Length = 6.0$; $width = 0.2$; $depth = 0.1$; $mesh = 6 \times 1 \times 1$; $E = 1.0 \times 10^7$; $\nu = 0.3$. The theoretical solutions for the problem are $U^{Ref} = 0.1081$ and $W^{Ref} = 0.4321$ for the in-plane and out-of-plane load, respectively.

Table 4.10: Normalized tip deflection of the straight cantilever beam. In-plane loading case.

$U^{Ref} = 0.1081$ [19]			
Element shape	**Regular**	**Trapezoidal**	**Parallelogram**
HEX20	0.970	0.886	0.967
HEX20(R)	0.984	0.964	0.994
SOLID95	0.994	0.966	0.988
USHEXA20	0.994	0.985	0.989
SFR20	0.990	0.989	0.985
SFR20I	0.998	0.995	0.991

Comparison of the normalized tip deflection for the proposed elements with other reference elements is presented in Tables 4.10 and 4.11. Notably, the SFR20 and SFR20I elements demonstrate accurate performance when subjected to trapezoidal shapes for both in-plane and out-of-plane loads. Conversely, a slight decrease in accuracy is observed when parallelograms are employed, particularly under out-of-plane loads.

Table 4.11: Normalized tip deflection of the straight cantilever beam. Out-of-plane loading case.

$W^{Ref} = 0.4321$ [19]			
Element shape	**Regular**	**Trapezoidal**	**Parallelogram**
HEX20	0.961	0.920	0.941
HEX20(R)	0.972	0.964	0.961
SOLID95	0.992	0.987	0.987
USHEXA20	0.992	0.987	0.987
SFR20	0.986	0.975	0.946
SFR20I	0.996	0.986	0.964

4.6 Square clamped plate

This example is a popular benchmark to evaluate the performance and accuracy of finite elements [19, 54, 92]. Figure 4.12 shows a square plate with clamped supports subjected to a point load of $P = 4 \times 10^{-4}$ at the center. The square plate of dimension $L = 2.0$ with uniform thickness $h = 0.01$ and material properties $E = 1.7472 \times 10^7$, $\nu = 0.3$. Because of the symmetry only a quarter of the plate is studied. The convergence of the proposed elements was studied by modelling the square plate using one element through

the thickness and $N = 2, 4, 6, 8$ and 10 elements on each side. The analytical solution for square clamped plate under a concentrated load is $W^{Ref} = 5.6 \times 10^{-6}$. The normalized values of the deflection at the central point are given in Table 4.12.

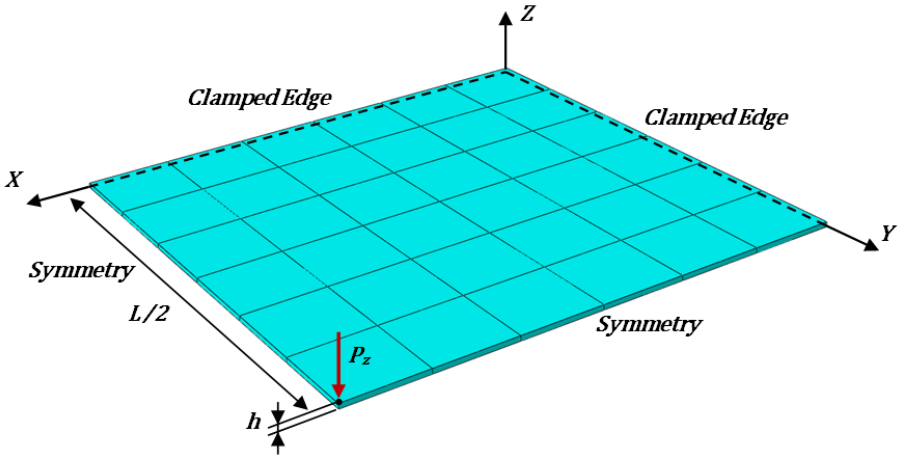

Figure 4.12: Square plate subjected to a concentrated load in the center with $6 \times 6 \times 1$ mesh.

From the observation of Figure 4.13, it is evident that the presented elements yield the most favourable overall results, exhibiting rapid convergence to the exact solution. The noteworthy rate of convergence is particularly notable even for a very coarse mesh ($N = 2$), distinguishing them from other quadratic hexahedral elements.

Table 4.12: Normalized transverse displacement at the center. Square plate with clamped supports subjected to a concentrated load.

$W^{Ref} = 5.6 \times 10^{-6}$ [19]							
Mesh	**C3D20**	**C3D20R**	**SOLID95**	**HEXA20**	**USHEXA20**	**SFR20**	**SFR20I**
$2 \times 2 \times 1$	NA	0.434	0.313	0.310	0.191	0.847	0.864
$4 \times 4 \times 1$	0.822	0.943	0.868	0.868	0.912	0.978	0.990
$6 \times 6 \times 1$	0.931	0.979	0.870	0.943	0.952	0.990	0.998
$8 \times 8 \times 1$	0.960	0.987	0.959	0.970	0.973	0.994	1.000
$10 \times 10 \times 1$	0.973	0.991	0.982	0.982	0.984	0.996	1.001

4.7 Circular plate

The test considers a circular plate clamped along the circumference and it is loaded with a concentrated force at the center. Because of the symmetry of the problem, only a quarter of the plate is discretized and the appropriate boundary conditions are applied on the symmetry plans. This quarter is modeled with one element through the thickness

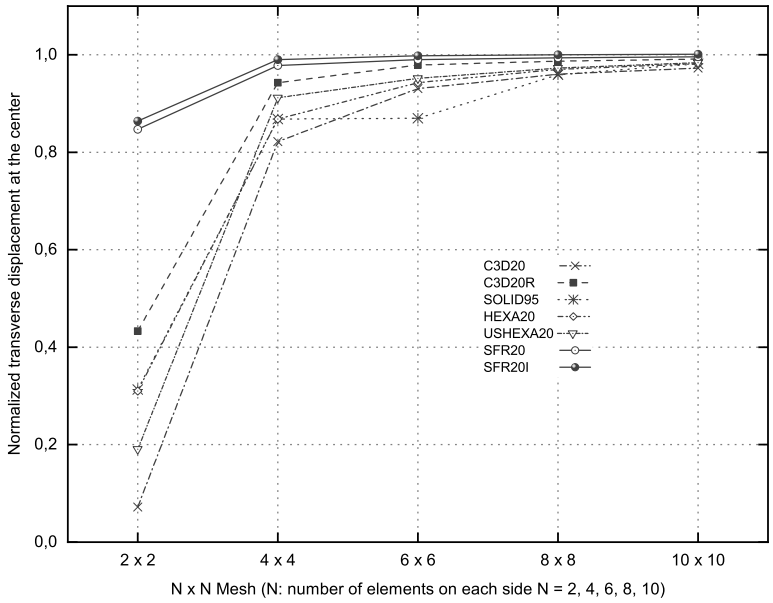

Figure 4.13: Convergence of normalized transverse displacement at the center. Square plate subjected to a concentrated load.

and $N = 2, 4, 6, 8, 10$ and 12 elements on each side. Geometry, mechanical properies and boundary conditions of the problem are indicated in Figure 4.14. The analytical solution of the transverse displacement at the center is given by Kirchhoff plate theory [93] Eq. (4.3):

$$W = \frac{3(1-\nu^2)FR^2}{4\pi Et^3} = 2.1725 \times 10^{-3} \tag{4.3}$$

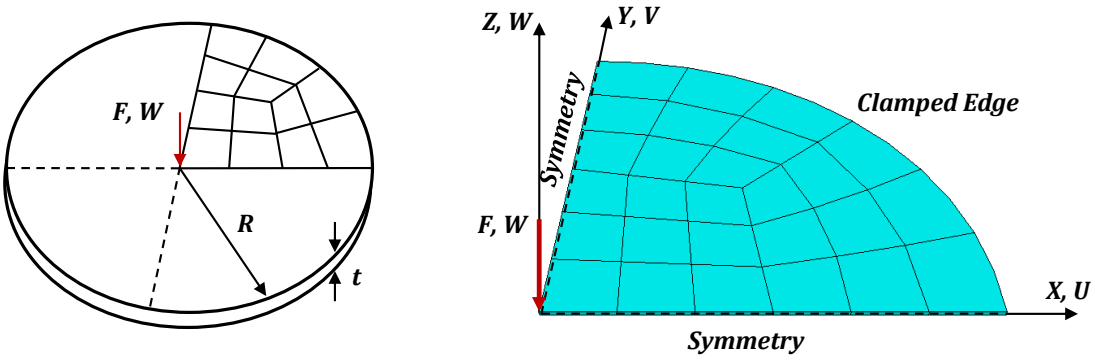

Figure 4.14: Problem statement of clamped circular plate under concentrated load.

Normalized values for various elements are displayed in Table 4.13. It is evident that SFR20 and SFR20I yield highly accurate results in comparison to the classical hexahedral element HEX20, as well as both Abaqus elements C3D20 and C3D20R. Moreover, the

presented elements exhibit a rapid convergence to the analytical solution, even with a coarse mesh, as illustrated in Figure 4.15. Therefore, the SFR approach made adding another layer of elements across the thickness unnecessary.

Table 4.13: Normalized transverse displacement at the center. Circular plate with clamped supports subjected to a concentrated load.

$W = 2.1725 \times 10^{-3}$ [93]					
Mesh	**HEX20**	**C3D20**	**C3D20R**	**SFR20**	**SFR20I**
$2 \times 2 \times 1$	0.151	0.151	0.465	0.907	0.931
$4 \times 4 \times 1$	0.688	0.688	0.863	0.977	0.990
$6 \times 6 \times 1$	0.895	0.895	0.956	0.988	0.997
$8 \times 8 \times 1$	0.947	0.947	0.979	0.992	0.999
$10 \times 10 \times 1$	0.968	0.968	0.987	0.994	1.000
$12 \times 12 \times 1$	0.989	0.978	0.991	0.996	1.000

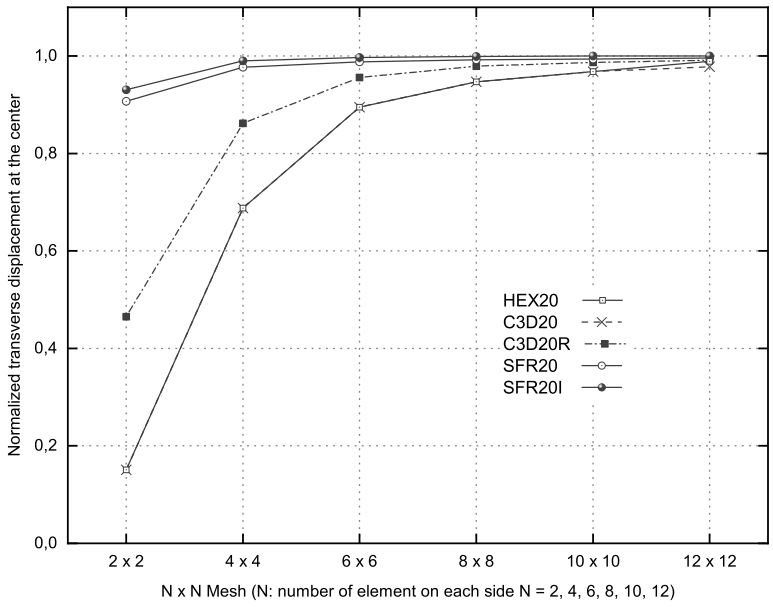

Figure 4.15: Convergence of Nomalized transverse displacement at the center for circular plate problem.

4.7.1 Run-time efficiency test

To evaluate the run-time efficiency of the proposed elements, the computational time is assessed for the aforementioned circular plate problem. The computational cost for establishing the global stiffness matrix and solving the algebraic equations is depicted in Figure 4.16. From the plots, it can be inferred that, for equivalent displacement results,

the run-time required for both SFR20 and SFR20I elements employing the Space Fiber Rotation concept presented here appears to asymptotically lower than that of the classical hexahedral element HEX20.

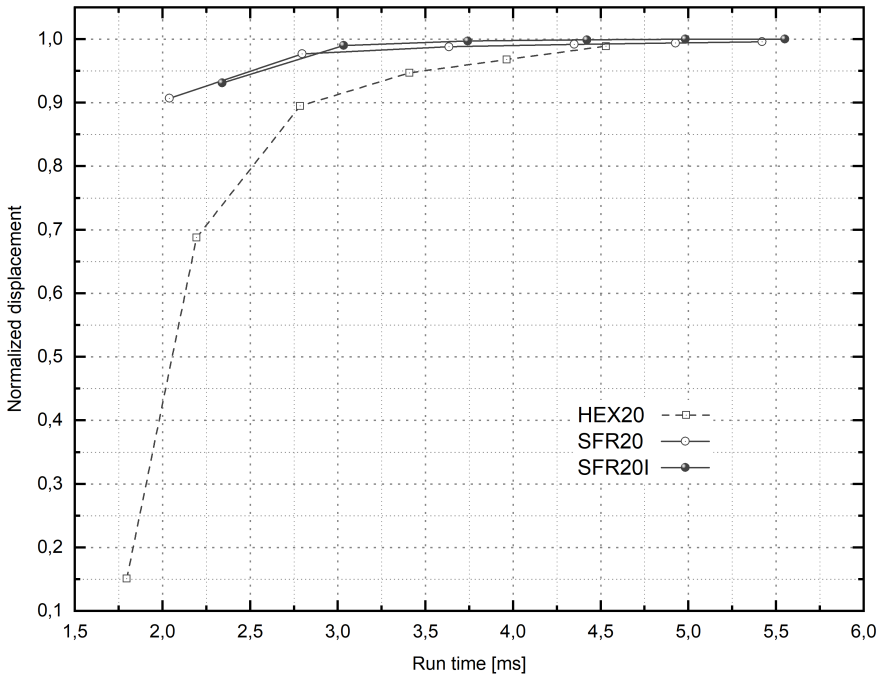

Figure 4.16: Computational cost for establishing the global stiffness matrix and the solving system equations of the circular plate problem.

4.8 Pinched spherical shell

The following example deals with a hollow sphere with two radially opposed point loads as shown in Figure 4.17. This example is usually used to check the absence of shear and membrane locking in structures exhibiting bending behavior. Dimensions, mechanical properties, and boundary conditions are shown in Table 4.14. Due to symmetry, only an eighth of the structure is discretized into $N \times N \times 1$ regular elements ($N = 2, 4, 8$ and 10 per side). The analytical solution of the problem is given in the work of MacNeal and Harder [19]:

$$U_A \;=\; -\,V_B \;=\; 0.094$$

Findings of displacements at point A across various solutions are summarized in Table 4.15. For assessing the rate of convergence, the normalized displacements at point A are graphed against the number of elements in Figure 4.18. It is evident from the outcomes that the accuracy and rate of convergence of the SFR20 and SFR20I elements surpass those of all reference elements.

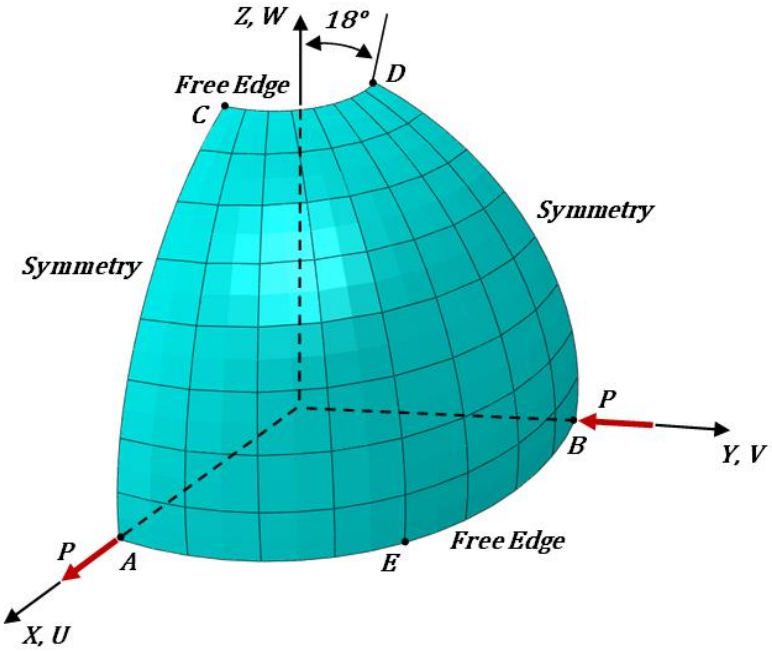

Figure 4.17: Hemisphere under diametrically opposite charges.

Table 4.14: Mechanical properties, geometry, boundary and symmetry conditions of shell tests.

	Spherical shell	**Cylindrical shell**
Mechanical properties and geometry		
	$R = 10$, $h = 0.04$, $R/h = 250$, $E = 6.825 \times 10^7$, $\nu = 0.3$	$L = 6$, $R = 3$, $h = 0.03$, $E = 3 \times 10^{10}$, $\nu = 0.3$
Boundary condition		
	$W = 0$ on E	$U = W = \theta_Y = 0$ on AD
Symmetry conditions		
	$V = \theta_X = \theta_Z = 0$ on AC	$W = \theta_X = \theta_Y = 0$ on AB
	$U = \theta_Y = \theta_Z = 0$ on BD	$V = \theta_X = \theta_Z = 0$ on BC
		$U = \theta_Y = \theta_Z = 0$ on CD
Load		
	$P = 2$	$P_Z = -0.25$

4.9 Pinched cylindrical shell with end diaphragms

This last example considers a cylinder with rigid end diaphragms subjected to radially point load at point C, as shown in Figure 4.19. This problem evaluates the performance of finite elements in both inextensional bending and complex membrane states of stress [94]. A reference solution of the present problem is given by Flügge [95] as:

$$W_C^{Ref} = -\frac{W_C E h}{P} = 164.24 \tag{4.4}$$

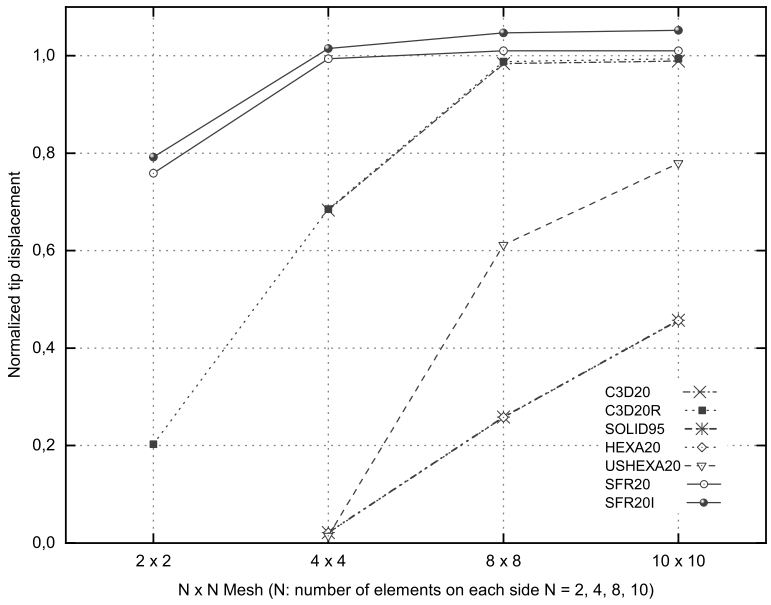

Figure 4.18: Convergence of normalized tip displacement of the pinched spherical shell.

Table 4.15: Normalized tip displacement in the force direction for pinched spherical shell problem.

$U_A = -V_B = 0.094$ [19]							
Mesh	**C3D20**	**C3D20R**	**SOLID95**	**HEXA20**	**USHEXA20**	**SFR20**	**SFR20I**
$2 \times 2 \times 1$	NA	0.203	NA	NA	NA	0.759	0.792
$4 \times 4 \times 1$	0.683	0.685	0.021	0.021	0.014	0.994	1.015
$8 \times 8 \times 1$	0.984	0.988	0.258	0.258	0.612	1.010	1.047
$10 \times 10 \times 1$	0.989	0.994	0.457	0.457	0.779	1.010	1.052

Dimensions, mechanical properties as well as applied boundary conditions are exposed in Table 4.14. Due to symmetry, only a segment of 90^o of the cylinder is examined with the appropriate boundary conditions along the symmetry plans. The cylinder is modeled using a regular mesh of $N = 2, 4$ and 6 elements per side. The displacements at point C of different element solutions are presented in Table 4.16.

SFR20 yields superior results compared to the classical hexahedral element HEX20 and C3D20. A slight difference is observed between the proposed element SFR20 and the elements C3D20R and SHB20. Conversely, the outcomes of the non-conforming element SFR20I surpass those of all other counterparts.

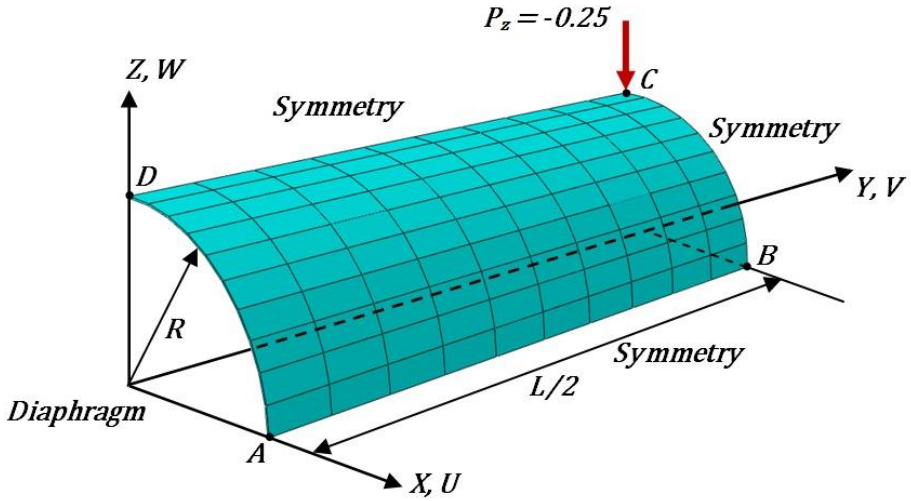

Figure 4.19: Pinched cylindrical shell with end diaphragms geometry, boundary and symmetry conditions; example of a cylindrical shell mesh.

Table 4.16: Normalised displacement for the pinched cylinder with diaphragms.

$W_C^{Ref} = 164.24$ [95]						
Mesh	**HEX20**	**C3D20**	**C3D20R**	**SHB20**	**SFR20**	**SFR20I**
$2 \times 2 \times 1$	NA	0.043	0.630	NA	0.468	0.551
$4 \times 4 \times 1$	0.140	0.140	0.872	0.883	0.823	0.932
$6 \times 6 \times 1$	0.328	0.328	0.952	0.961	0.929	1.057

Chapter 5

Numerical modelling of the elastoplastic behaviour

Summary

5.1 Introduction

The following chapter provides a general framwork of the continuum constitutive description of the behaviour of elastoplastic materials. The theory behained the description called the theory of plasticity, and it can be traced back to the middle of the nineteenth to the first half of the twentieth century. Basically, the theory of plasticity is concerned to the materials or solids in general that after being subjected to a loading, the solid exhibites a permanant deformation when completely unloading. Materials that exhibites elastoplastic behaviour are called plastic materials, such as metals, concrete, rocks, clays and soils. For more additional details on the theory of plasticity the reader is reffered to the standard textbooks [96, 97, 98, 99, 100, 101]. The chapter is structured as follows: Firstly, section 5.2 gives a brief description of different types of nonlinearity in solid mechanics. After that, section 5.3 addresses a detailed overview on the elastoplastic behaviour. Moreover, the numerical implementation of stresses and tangent moduli which are needed for the computation of the elastoplastic constitutive equations are presented in section 5.4. The last section 5.6 shows the computation process to solve the non-linear equation by using iterative methods and the finite element method.

5.2 Nonlinearity in solid mechanics

nonlinearity in solid mechanics refers to the phenomenon where the relationship between the stress and strain in a material is not linear. In linear mechanics, the relationship between stress and strain is described by *Hooke's law*, which states that stress is proportional to strain. However, for many materials, this relationship is only valid within a certain range of stresses and strains, beyond which the material exhibits non-linear behaviour.

Non-linear behaviour in solid mechanics can be caused by various factors, such as material composition, loading conditions, and geometry. Some examples of non-linear behaviour include plastic deformation, creep, fatigue, and fracture. This behaviour can be analyzed using numerical methods such as finite element analysis, which involve dividing the material into small elements and solving the equations of motion for each element.

5.2.1 Geometric nonlinearity

This type of nonlinearity arises when the deformation of a structure or material is large enough to cause a change in the geometry of the structure. As a result, the relationship between stress and strain becomes nonlinear, and the response of the structure to external loads can be highly dependent on the magnitude and direction of the applied loads. Examples of geometric nonlinearity include large deflection of beams, buckling

of columns, and instability of plates. Add to that, geometric nonlinearity can lead to complex deformation patterns, such as bifurcations, snap-through, and limit points [102].

5.2.2 Boundary nonlinearity

Boundary nonlinearity occures when the boundary conditions of a problem are nonlinear. For example, if the boundary of a structure is not rigid, but instead undergoes deformation, this can cause nonlinear behaviour in the structure itself. Examples of boundary nonlinearity include a curved beam with a nonlinearly varying radius and a structure with a nonlinearly varying stiffness along its length. A detailed explanation of various analytical and numerical methods for analyzing thin-walled structures under nonlinear boundary conditions can be found in [103].

5.2.3 Contact nonlinearity

Contact nonlinearity can be found when two or more bodies come into contact, causing changes in the deformation and stress distribution in the bodies. This can lead to nonlinear behaviour, such as stick-slip behaviour, in which the contact surfaces alternate between sticking and sliding. Examples of contact nonlinearity include frictional contact between two surfaces, indentation of a material by a rigid object, and impact of two objects. Contact nonlinearity can be found in various engineering applications, including automotive, aerospace, and biomedical engineering.

5.2.4 Material nonlinearity

Material nonlinearity arises from the nonlinear behaviour of the material itself. For example, many materials exhibit nonlinear stress-strain behaviour due to phenomena such as plastic deformation, creep, and damage. The stress-strain relationship may also depend on the rate of loading, temperature, and other factors. Examples of material nonlinearity include elasto-plastic deformation of metals, viscoelastic behaviour of polymers, and damage accumulation in composites.

5.3 Elastoplastic behaviour description

The major objective of the mathematical theory of plasticity is to provide a continuum constitutive mathematical model capable of describing the relationship between the stress and strain of materials that posses an elastoplastic behaviour sufficiently. One way to form the basis of the mathematical theory of plasticity is by performing a uniaxial tension

experiment with a metallic bar, this test with ductile metals produces a stress-strain curve that is shown in Figure 5.1. The path $(O_0Y_0Y_1Z_1)$ is normally defined as the *virgin curve* and it can be described in the following. In this path; the segment O_0Y_0 is linear, and the behaviour of the material is regarded as linear elastic. Thus, in case of loading and unloading the material remains with the original state. After loading from the initial unstressed state to the stress level σ_0, it can be noted a dramatic changing in the stress-strain curve. After reaching the stress level σ_0 and unloading, the bar returns to a new state via the path Y_1O_1 and a permanent (plastic) change in the shape of the bar is observed; that can be seen in the graph by the strain ε^p. At this state the behaviour of the bar between O_1 and Y_1 is considered to be linear elastic, with constant strain ε^p and yield limit σ_0. At this stage the total strain ε is split up into the sum of two components; an elastic (or reversible) component ε^e and a plastic (or irreversible) component ε^p, that gives:

$$\varepsilon = \varepsilon^e + \varepsilon^p \tag{5.1}$$

where we can define the elastic strain as:

$$\varepsilon^e = \varepsilon - \varepsilon^p \tag{5.2}$$

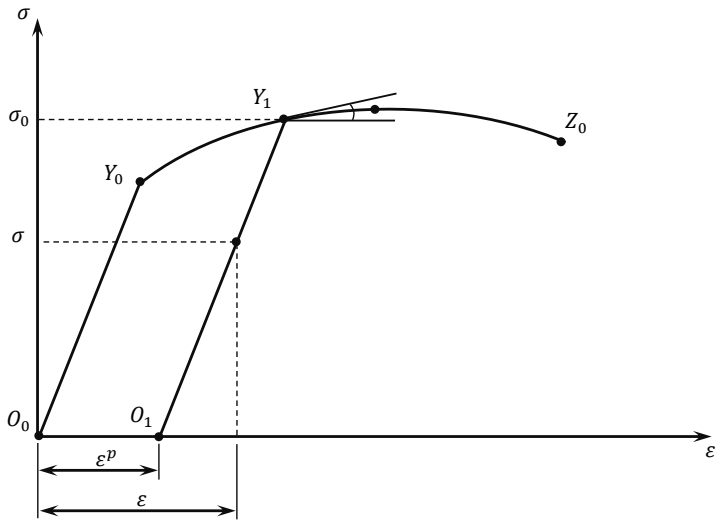

Figure 5.1: A nonlinear stress-strain curve for a metallic bar under uniaxial tension.

Before the plastic yielding, the relation between the uniaxial stress and strain is given by the standard linear elastic expression:

$$\sigma = C^e \varepsilon^e \tag{5.3}$$

By substituting Equation (5.2) in Equation (5.3) we define the uniaxial stress with respect to the total strain:

$$\sigma = C^e \left(\varepsilon - \varepsilon^p\right) \tag{5.4}$$

The formulation of the elastoplastic constitutive mathematical model requires four fundamental phenomenological properties:

- The formulation of stress-strain relation that describe the material behaviour before the plastic yielding zone.
- A yield function that indicates the beginning of the plastic yielding. The yield function describe the transition from elasticity to plasticity, a flow rule appears after further loading on the yield stress; which describe the evolution of plastic strain.
- Hardening law which governs the evolution of yield stress with respect to plastic strain.
- The decomposition of the total strain increment into, an elastic reversible part $d\varepsilon^e$ and an irreversible plastic part $d\varepsilon^p$.

5.3.1 The yield function and the yield surface

The yield function or *yield criterion* evaluates the stress limits to yielding point where the plastic strain occurs, and it can be written in the general form as:

$$\phi\left(\sigma, H\right) = 0 \tag{5.5}$$

Where ϕ is the yield function; which is a function of the stress tensor and a set H of *Hardening thermodynamical forces.* The yield function can be depicted by a hypersurface (or *yield surface*) in the space of stresses, where it can be found to satisfies three states:

$\phi\left(\sigma, H\right) < 0$ elastic, σ lies in the elastic domain

$\phi\left(\sigma, H\right) = 0$ plastic, σ lies at the boundary

$\phi\left(\sigma, H\right) > 0$ inadmissible, σ lies outside of the domain

- The yield function defines the elastic domain, where the stress states lying in the yield surface and the material behave elastically:

$$D_{el} = \left\{\sigma \mid \phi\left(\sigma, H\right) < 0\right\} \tag{5.6}$$

- The yield function defines the plastic domain, where the stress states reaches the yield limit or in the boundary of the elastic domain. Hence:

$$D_{pl} = \{\sigma \mid \phi(\sigma, H) = 0\} \tag{5.7}$$

- The stress lying outside the yield surface are in the inadmissible domain, where:

$$D = \{\sigma \mid \phi(\sigma, H) > 0\} \tag{5.8}$$

5.3.1.1 Three dimensional principal stress space

Consider three dimension space with perpendicular principal stress axes in Figure 5.2. The stress states at any arbitrary point on the yield surface as point A with the components $(\sigma_1, \sigma_2, \sigma_3)$; it may be represented by a vector from the origin O (ie. $\overrightarrow{OA} = \sigma$). A space diagonal Oh defined by point $\sigma_1 = \sigma_2 = \sigma_3$ with equal angles to all three principal stress axes; that its cosines equal $\left(1/\sqrt{3}, 1/\sqrt{3}, 1/\sqrt{3}\right)$.

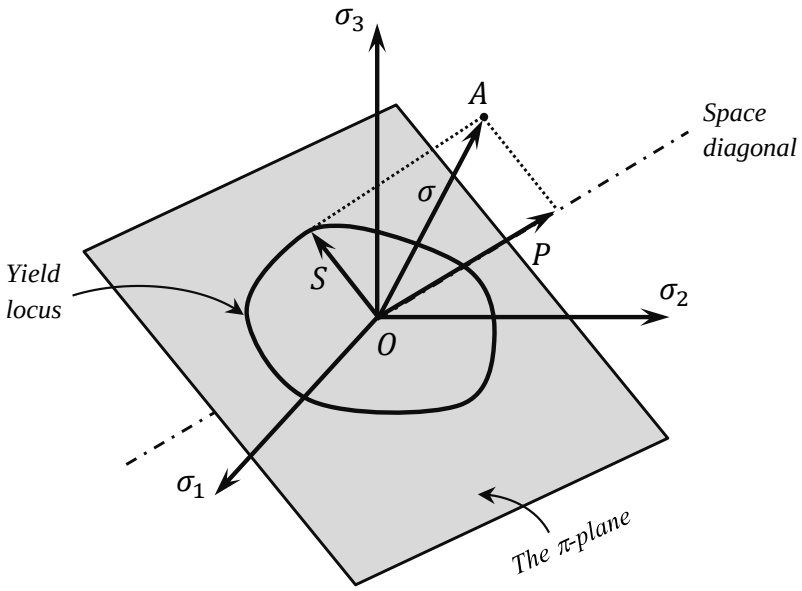

Figure 5.2: Yield locus/surface in three dimensional stress-space.

Where P and S are the *Hydrostatic* and *Diviatoric stress vectors*, respectively. Both vectors are defined as follows:

$$P = \frac{1}{\sqrt{3}}(\sigma_1 + \sigma_2 + \sigma_3) \tag{5.9}$$

$$S = \frac{1}{3}\left[(\sigma_1 - \sigma_2)^2 + (\sigma_2 - \sigma_3)^2 + (\sigma_3 - \sigma_1)^2\right] \tag{5.10}$$

It is worth noting that the deviatoric stress vector lies in the plane passing through O. This plane is known as *the deviatoric plane* (or *the π-plane*) with the Equation $\sigma_1 + \sigma_2 + \sigma_3 = 0$ in the principle stress space. Since the hydrostatic stress does not affect on yielding. Hence, any other arbitrary point will also be on the yield surface and the yielding will be depending only on the deviatoric stress. The yield surface can be obtained by sliding the yield locus up and down along the space diagonal.

5.3.2 Plastic dissipation function

An important step in the derivation of the model that proves a constitutive formulation is the formulation of general dissipative model by the *free energy potential*, where the free energy ψ is described as:

$$\psi\left(\varepsilon, \varepsilon^p, \alpha\right) \tag{5.11}$$

Where ψ is a function of the total strain, the plastic strain and a set α of internal variables describing the Hardening phenomenon. The free energy is assumed to be decomposed of two components as:

$$\psi\left(\varepsilon, \varepsilon^p, \alpha\right) = \psi^e\left(\varepsilon, \varepsilon^p\right) + \psi^p\left(\alpha\right) = \psi^e\left(\varepsilon^e\right) + \psi^p\left(\alpha\right) \tag{5.12}$$

Where the first part is related to elastic contribution and the scond is a contribution due to hardening. By applaying the CLAUSIUS-DUHEM inequality [98] the free energy function can be written as:

$$\left(\sigma - \rho\frac{\partial\psi^e}{\partial\varepsilon^e}\right) : \varepsilon^e + \sigma : \varepsilon^p - \mathbb{A} * \dot{\alpha} \geqslant 0 \tag{5.13}$$

Where $\mathbb{A}$ is the hardening thermodynamical force:

$$\mathbb{A} \equiv \rho\frac{\partial\psi^p}{\partial\alpha} \tag{5.14}$$

By deriving the stress tensor we get:

$$\sigma = \rho\frac{\partial\phi^e}{\partial\varepsilon^e} \tag{5.15}$$

The plastic dissipation function takes the form:

$$\mathbb{D}^p\left(\sigma, \mathbb{A}, \varepsilon^p, \dot{\alpha}\right) \equiv \sigma : \dot{\varepsilon}^p - \mathbb{A} * \dot{\alpha} \tag{5.16}$$

5.3.3 Plastic flow rule and hardening law

The plastic dissipation function in Equation (5.16) is associated with two internal variables; the plastic tensor and the set α of hardening variables. The definition of the evolution laws are required to complete the elastoplastic model. The plastic flow rule determines the evolution of the plastic strain ε^p, and the hardening law describe an evolution of the yield stress accompanies the evolution of the plastic strain. The plastic flow rule and the hardening law can be expressed as:

$$\dot{\varepsilon}^p = \dot{\gamma}\mathbb{N}\left(\sigma, \mathbb{A}\right) \tag{5.17}$$

$$\dot{\alpha}^p = \dot{\gamma}H\left(\sigma, \mathbb{A}\right) \tag{5.18}$$

Where $\mathbb{N}(\sigma, A)$ is the flow vector, $H(\sigma, \mathbb{A})$ describe the evolution of hardening. Both variables can be derived by the plastic flow potential $\Psi = \Psi(\sigma, A)$ as following:

$$\mathbb{N}\left(\sigma, \mathbb{A}\right) \equiv \frac{\partial \Psi}{\partial \sigma} \tag{5.19}$$

$$H\left(\sigma, \mathbb{A}\right) \equiv -\frac{\partial \Psi}{\partial \mathbb{A}} \tag{5.20}$$

Lastly, $\dot{\gamma}$ is *the plastic multiplier* in which it describe the magnitude of plastic flow.

These two Equation (5.19) and (5.20) are completed by the KUHN-TUKER optimality conditions or loading/unloading condition when plastic flow may occur [98] and can be written as:

$$\phi\left(\sigma, \mathbb{A}\right) \leqslant 0 \quad , \quad \dot{\gamma} \geqslant 0 \quad , \quad \dot{\gamma}\phi\left(\sigma, \mathbb{A}\right) = 0 \tag{5.21}$$

The above KUHN-TUCKER condition satisfies all possible states of materials; in case of the material behave elastically where $(\phi \neq 0)$ it becomes:

$$\phi\left(\sigma, \mathbb{A}\right) < 0 \quad , \quad \dot{\gamma} = 0 \quad , \quad \dot{\gamma}\phi\left(\sigma, \mathbb{A}\right) = 0 \tag{5.22}$$

When the stress is on the yield surface which means the material behave plastically $(\phi = 0)$, three cases the plastic multiplier can be distinguished:

$$\begin{array}{lll} \dot{\phi} < 0 & \Rightarrow & \dot{\gamma} = 0 \quad \textit{elastic unloading}, \\ \dot{\phi} = 0 & \Rightarrow & \dot{\gamma} = 0 \quad \textit{neutral loading}, \\ \dot{\phi} = 0 & \Rightarrow & \dot{\gamma} > 0 \quad \textit{plastic flow}. \end{array} \tag{5.23}$$

5.3.4 Plastic multiplier

During plastic flow ($\dot{\gamma} > 0$), the current stress is required to remain on the yield surface. Thus, yield function remains constant during the plastic loading state ($\phi = 0$). Therefore, *additional complementary condition* can be established:

$$\dot{\phi}\dot{\gamma} = 0 \tag{5.24}$$

Where $\dot{\phi}$ is the rate of the yield function and it vanishes whenever plastic yielding occurs ($\dot{\gamma} \neq 0$). Hence:

$$\dot{\phi} = 0 \tag{5.25}$$

Where Equation (5.25) is *the consistency condition.* The plastic multiplier can be determined initially by differentiating the yield function with respect to time, one can obtain:

$$\dot{\phi} = \frac{\partial \phi}{\partial \sigma} : \dot{\sigma} + \frac{\partial \phi}{\partial \mathbb{A}} * \dot{\mathbb{A}} \tag{5.26}$$

The rate of the stress tensor can be obtain with respect to Equation (5.4) by the following expression:

$$\dot{\sigma} = C^e \left(\dot{\varepsilon} - \dot{\varepsilon}^p\right) \tag{5.27}$$

Where C^e denotes, the elasticity tensor with respect to *HOOK's Law.* By substituting the plastic flow rule Equation (5.19) in Equation (5.27), the rate form of the stress becomes:

$$\dot{\sigma} = C^e \left(\dot{\varepsilon} - \dot{\gamma}\mathbb{N}\right) \tag{5.28}$$

Using the definition of $\mathbb{A}$ stated in Equation (5.14), the evolution law Equation (5.20) and the stress rate in Equation (5.28) in Equation (5.26) gives:

$$\dot{\phi} = \frac{\partial \phi}{\partial \sigma} : C^e : \left(\dot{\varepsilon} - \dot{\gamma}\mathbb{N}\right) + \dot{\gamma}\frac{\partial \phi}{\partial \mathbb{A}} * \rho\frac{\partial^2 \Psi}{\partial \alpha^2} * H \tag{5.29}$$

The plastic multiplier is obtained from the Equation above, by applying the consistency condition, where $\dot{\phi} = 0$, this leads to:

$$\dot{\gamma} = \frac{\dfrac{\partial \phi}{\partial \sigma} : C^e : \dot{\varepsilon}}{\dfrac{\partial \phi}{\partial \sigma} : C^e : \mathbb{N}\left(\sigma, \mathbb{A}\right) - \dfrac{\partial \phi}{\partial A} * \rho\dfrac{\partial^2 \Psi^p}{\partial \alpha^2} * H\left(\sigma, \mathbb{A}\right)} \tag{5.30}$$

Or we can write:

$$\dot{\gamma} = \frac{\phi_{,\sigma} : C^e : \dot{\varepsilon}}{\phi_{,\sigma} : C^e : \mathbb{N} - \phi_{,\mathbb{A}} * \rho\Psi^{p2}_{,\alpha} * H} \tag{5.31}$$

5.3.5 The continuum elastoplatic tangent stiffness modulus

Back to Equation (5.28) the rate of stress tensor is defined with the definition of the plastic multiplier, by substituting the plastic multiplier in Equation (5.31), this gives:

$$\dot{\sigma} = C^e \left(\dot{\varepsilon} - \frac{\phi_{,\sigma} : C^e : \dot{\varepsilon}}{\phi_{,\sigma} : C^e : \mathbb{N} - \phi_{,\mathbb{A}} * \rho\Psi^{p2}_{,\alpha} * H} N \right) \tag{5.32}$$

Equation (5.32) can be rearranged to express the elastoplastic stress-strain rates, as:

$$\dot{\sigma} = \left[C^e - \frac{(C^e : \mathbb{N})\,(C^e : \phi_{,\sigma})}{\phi_{,\sigma} : C^e : \mathbb{N} - \phi_{,\mathbb{A}} * \rho\Psi^{p2}_{,\alpha} * H} \right] : \dot{\varepsilon} \equiv C^{ep} : \dot{\varepsilon} \tag{5.33}$$

Where C^{ep} is *the continuum elastoplastic tangent modulus* and it can be expressed as a combination of an elastic and plastic component:

$$C^{ep} = C^e + C^p \tag{5.34}$$

Where C^e and C^p are the elastic and plastic stress-strain matrices, respectively. C^e is already defined in Equation (2.40) and C^p is expressed as follows:

$$C^p = \frac{(C^e : N)\,(C^e : \phi_{,\sigma})}{\phi_{,\sigma} : C^e : \mathbb{N} - \phi_{,\mathbb{A}} * \rho\Psi^{p2}_{,\alpha} * H} \tag{5.35}$$

5.3.6 Yield criterion

A general form of the yield function has been introduced in Section (5.3.1), and it found that it can be expressed by a yield surface; where the yield surface is an hypothesis concerning the limit of elasticity under any kind or combination of stresses, where as in engineering the yield criteria found through the literature with different kinds; the most used yield criterion are *Tresca*, *Von-Mises*, *Mohr-Coulomb* and *Drucker-Prager*. Each criteria has its advantages with respect to the type of material; for pressure-insensitive materials like metals the Tresca and Von-Mises criterion are the most adequate. In the other hand, the Mohr-Coulomb and Drucker-Prager criterion are more suitable to model soil, rocks or concretes or pressure-sensitive materials. A condition have to be considred is that the yield criteria should be independent of the orientation of the coordinates system used, and the yield function ϕ should be expressed by the three stress invariants as [96]:

$$\phi\left(J_1, J_2, J_3, \mathbb{A}\right) = 0 \quad or \quad \phi\left(J_1, J_2, J_3\right) = \mathbb{A} \tag{5.36}$$

Where the stress invariants are defined by the following expressions:

$$\begin{cases} J_1 = \sigma_{ij} = tr\left(\sigma\right) \\ J_2 = \frac{1}{2}\sigma_{ij}\sigma_{ij} = \frac{1}{2}\left(S:S\right) \\ J_3 = \frac{1}{3}\sigma_{ij}\sigma_{jk}\sigma_{ki} = \frac{1}{3}tr\left(S\right)^3 \end{cases} \tag{5.37}$$

Where S is the deviatoric stress tensor is given by:

$$S = \sigma - \frac{1}{3}\left(tr\sigma\right) \tag{5.38}$$

Bridgeman [104] states by experimental observation, that the plastic deformation of metal is independent of the hydrostatic pressure. Therefore, the yield function can be expressed in terms of the deviatoric stress tensors as:

$$\phi\left(J_2, J_3, \mathbb{A}\right) = 0 \tag{5.39}$$

5.3.6.1 Tresca yield criterion

The criterion was proposed following the works of Tresca on metal plasticity in 1986. The Tresca criterion states that plastic yielding begins when the maximum shear stress reaches a critical value.

$$\tau_{max} = Max\left(|\frac{\sigma_1 - \sigma_2}{2}|, |\frac{\sigma_2 - \sigma_3}{2}|, |\frac{\sigma_1 - \sigma_3}{2}|\right) \tag{5.40}$$

Whereas the stress tensor is defined by the principle stresses $\sigma_1,\ \sigma_2$ and σ_3 and the condition $\sigma_1 \geqslant \sigma_2 \geqslant \sigma_3$.

The onset of the Tresca criterion can be reached by performing a simple experiments. The yield stress in tensile test is σ_y; where: $\sigma_1 = \sigma_y,\ \sigma_2 = 0,\ \sigma_3 = 0$. In shear test, $\sigma_1 = \tau_y,\ \sigma_2 = 0,\ \sigma_3 = -\tau_y$, where τ_y is the yield stress of a material in pure shear. This leads to the following expression:

$$\frac{1}{2}\left(\sigma_{max} - \sigma_{min}\right) = \sigma_y = \tau_y\left(\alpha\right) \tag{5.41}$$

Where $\sigma_{max}, \sigma_{min}$ are the maximum and minimum principle stresses, respectively. τ_y is *the shear yield stress* which is assumed to be a function of a hardening internal variable α. The Tresca yield function is defined in case of $\phi = 0$ as:

$$\phi(\sigma) = (\sigma_{max} - \sigma_{min}) - \sigma_y(\alpha) \tag{5.42}$$

Where σ_y is the uniaxial yield stress. Thus, the Tresca yield criterion may be written as:

$$\sigma_y = 2\tau_y \tag{5.43}$$

Figure (5.3) show a representation of the yield surface for the Tresca criterion in the space of principal stress by an infinitely long regular hexagonal cylinder with radius $\sqrt{2/3}\sigma_y$, where the cylinder axes coincides with *the Hydrostatic or space diagonal* with the Equation ($\sigma_1 = \sigma_2 = \sigma_3$). Figure (5.4) illustrate the Tresca yield surface by its projection on the π-plane with zero hydrostatic pressure component. The Tresca yield criterion can also be described in term of stress invariant, where the yield function is expressed as:

$$\phi = 2\sqrt{J_2}\cos\theta - \sigma_y \tag{5.44}$$

Where J_2 is the invariant of the stress deviator stated early in Equation (5.37), and θ is *the Load angle* which is a function of the deviatoric stress defined as:

$$\theta = \frac{1}{3}\sin^{-1}\left(\frac{-3\sqrt{3}J_3}{2J_2^{3/2}}\right) \quad ; \quad -\frac{\pi}{6} < \theta < \frac{\pi}{6} \tag{5.45}$$

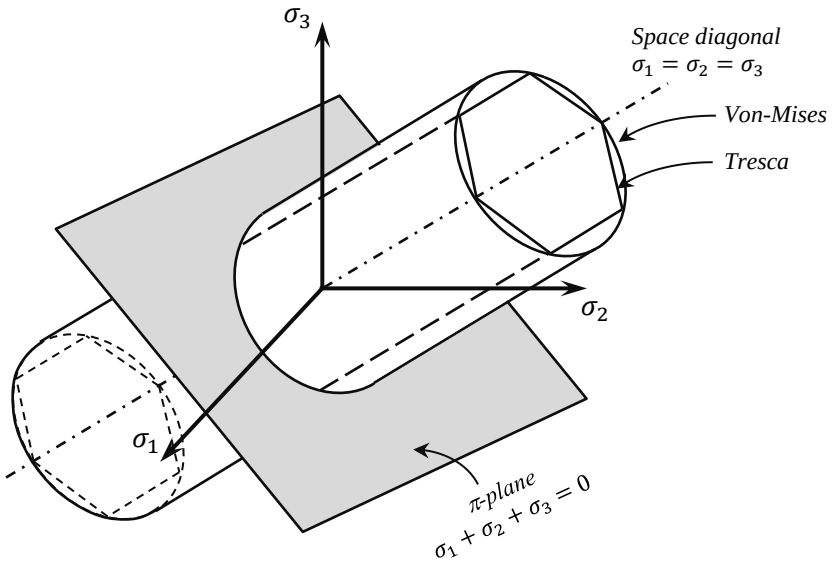

Figure 5.3: Geometrical representation of the Tresca and Von Mises yield surfaces in principal stress space.

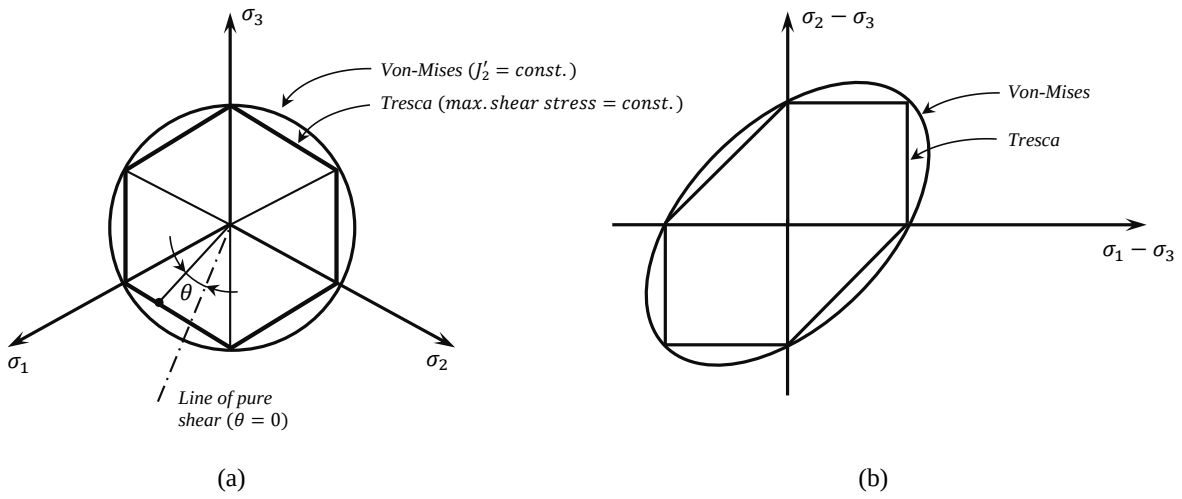

Figure 5.4: Two-dimensional representations of the Tresca and Von Mises yield criteria. (a) Octahedral plane representation, (b) Conventional engineering representation or biaxial state of stress.

5.3.6.2 Von-Mises yield criterion

While Tresca uses the maximum shear stress τ_{max} as an equivalent stress σ_e, the Von-Mises uses *the distortion energy theory*; by stating that yielding occurs when the equivalent stress reaches critical value (the yield stress σ_y) of the material in case of uniaxial tension, then the equivalent stress is expressed as follows:

$$\sigma_e \equiv \sqrt{\frac{3}{2} S : S} \equiv \sigma_y \equiv \sqrt{3J_2} \tag{5.46}$$

Where J_2 is the second deviatoric stress invariant, which can be explicitly expresses in term of stress components as:

$$J_2 = \frac{1}{6}\left[(\sigma_x - \sigma_y)^2 + (\sigma_y - \sigma_z)^2 + (\sigma_z - \sigma_x)^2\right] + \tau_{xy}^2 + \tau_{yz}^2 + \tau_{xz}^2 \tag{5.47}$$

The Von-Mises yield function is expressed using the equivalent stress by:

$$\phi(\sigma) = \sigma_e - \sigma_y = \sqrt{3J_2} - \sigma_y = 0 \tag{5.48}$$

Where σ_y is the uniaxial yield stress. The Von-Mises yield surface in which $\phi = 0$ is graphically represented in Figure (5.3) to be a circular cylinder in the principal stress space, where the cylinder axis coincides with the hydrostatic axis. The plastic behaviour of a material can be described by the diviator of a tensor that preserves the volumetric components. Thus, the deviatoric stress can be written as:

$$J_2 = \frac{1}{2} S : S \tag{5.49}$$

By the definition of Equation (5.47) one can observe that the Von-Mises yield surface is an ellipse which is ploted in Figure (5.4.b). Any point reside inside the ellipse where $\phi < 0$ it represent an elastic stress state. Points on the yield surface $\phi = 0$ represents the stress state where the material yielded. This leads to the definition of the Von-Mises yield criterion, to be written as:

$$\phi(\sigma) = \|S\| - \sqrt{\frac{2}{3}}\sigma_y = 0 \tag{5.50}$$

Where $\|S\|$ is the norm of the deviatoric stress, which can be expressed by:

$$\|S\| = (S : S)^{1/2} \tag{5.51}$$

The projection of the Von-Mises yield surface on the π-plane gives a smooth circle with a radius $\sqrt{2/3}\sigma_y$ in deviatoric stress space Figure (5.4.a). The Von-Mises circle apears to intersect with the vertices of the Tresca hexagon. In state of pure shear, the yield function for the Von-Mises criterion can be defined as:

$$\phi(\sigma) = \sqrt{2}\tau - \sqrt{\frac{2}{3}}\sigma_y = 0 \tag{5.52}$$

Hence, the yield and shear stresses for the Von-Mises criterion are related by the following relation:

$$\sigma_y = \sqrt{3}\tau \tag{5.53}$$

5.3.6.3 Mohr-Coulomb yield criterion

As mentioned before in Paragraph 5.3.6, the Tresca and Von-Mises are pressure-independent criteria and are suitable for modelling of plasticity in metals. However, the Mohr-Coulomb and Drucker-Prager criteria poses strong dependencies on hydrostatic pressure and they are adequate for modelling material such as soil, rocks and concrete. The Mohr-Coulomb criteria stems its notion from the generalisation of the Coulomb's 1773 *Friction failure law* by the following expression:

$$\tau = c - \sigma_n \tan\varphi \tag{5.54}$$

Where τ is the magnitude of shearing stress, c is the cohesion, φ is the internal friction or frictional angle and σ_n is the normal stress. The Mohr-Coulomb states that yielding occurs when the shearing stress τ and normal stress σ_n reach the critical combination. The Mohr-Coulomb criteria can be represent using the Mohr plane as shown in Figure (5.5). Given the condition $\sigma_1 \geqslant \sigma_2 \geqslant \sigma_3$, $\tau = \pm c$ and $\pm\tan\varphi$. Yield occurs when the

largest Mohr circle touches the critical line defined by the Equation (5.54) as depicted in Figure (5.5). Thus, one has:

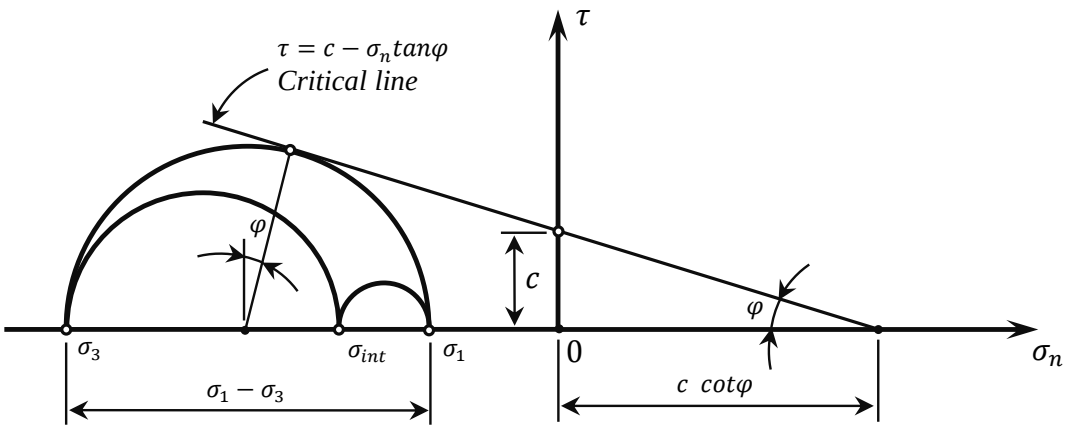

Figure 5.5: Representation of the Mohr-Coulomb criterion by the Mohr's circle.

$$\tau = \frac{\sigma_1 - \sigma_3}{2} \cos\varphi \tag{5.55}$$

$$\sigma_n = \frac{\sigma_1 + \sigma_2}{2} + \frac{\sigma_1 - \sigma_3}{2} \sin\varphi \tag{5.56}$$

The Mohr-Coulomb criterion in terms of the principal stresses can be defined by the following form:

$$(\sigma_1 - \sigma_3) = 2c\cos\varphi - (\sigma_1 + \sigma_3)\sin\varphi \tag{5.57}$$

The yield function for the Mohr-Coulomb criteria in terms of the principal stresses attains the form:

$$\phi(\sigma, c) = (\sigma_1 - \sigma_3) + (\sigma_1 + \sigma_3)\sin\varphi - 2c\cos\varphi \tag{5.58}$$

Figure (5.6) shows the Mohr-Coulomb yield surface in the principal stress space in which is an irregular hexagonal pyramid aligned with the hydrostatic axis, and whose Apex is located at $P = c\cot\varphi$. The projection of the yield surface in the π-plane represent an irregular hexagon as depicted in Figure (5.6.b). The Apex of the pyramid defines the limit of resistance to tensile pressure for a given material such as rock, soil or concrete.

From Figures (5.3) and (5.6.a), one can note that the Mohr-Coulomb criterion can be considered a reduced version of the Tresca criterion. Hence, both criteria tends to coincide when $c = \tau_y$ and $\varphi = 0$.

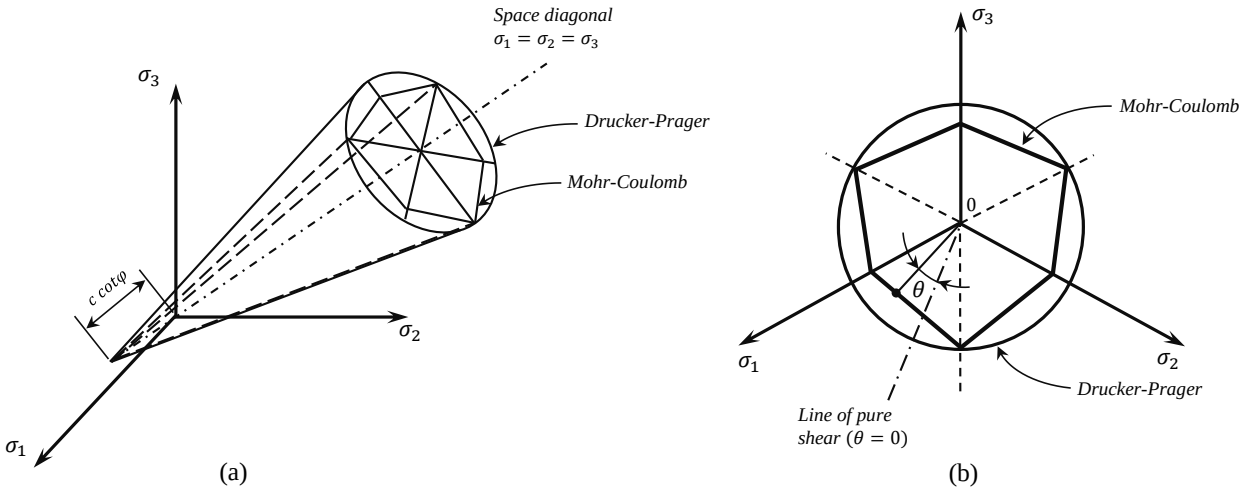

Figure 5.6: (a) Geometrical representation of the Mohr-Coulomb and Drucker-Prager yield surfaces in principal stress space, (b) Octahedral plane representation, projection of the Mohr-Coulomb and Drucker-Prager yield criteria on the π-plane.

5.3.6.4 Drucker-Prager yield criterion

The Drucker-Prager yield criterion was presented in 1952 as a smooth approximation to the Mohr-Coulomb yield criterion, In a similar way as the Von-Mises to the Tresca criterion. The Drucker-Prager yield criteria states that the yielding occurs when the second invariant J_2 of the deviatoric stress and the hydrostatic stress reach a critical combination. Hence, the The Drucker-Prager yield criteria is defined by:

$$\alpha J_1 + \sqrt{J_2(S)} = \overline{c} \tag{5.59}$$

The Drucker-Prager yield function can be defined in which the yield surface is approximated, where $\phi = 0$:

$$\phi\left(\sigma, c\right) = \sqrt{J_2\left(s\left(\sigma\right)\right)} + \iota J_1 - k = 0 \tag{5.60}$$

Where J_1 is the hydrostatic-dependent first invariant, ι and k are material parameters defined as follows:

$$\iota = \frac{6\sin\varphi}{3 - \sin\varphi} \tag{5.61}$$

$$k = \frac{6c\sin\varphi}{3 - \sin\varphi} \tag{5.62}$$

The representation of the The Drucker-Prager yield surface in the principal stress space is a circular cone with a radius $\sqrt{2}k$ and it has the same Apex of the Mohr-Coulomb yield

surface Figure (5.5). The circular cone is aligned with the hydrostatic axis. The projection of the yield surface on the π-plane shows that the yield locus is a circle Figure (5.6.b).

5.3.7 Hardening law

Earlier in Section 5.3.3 it has been stated that the evolution of the plastic strain accompanies an evolution of the yield stress, and this phenomenon is called *Hardening* or *strain-hardening*; where it is represented by changes in the hardening thermodynamical forces during plastic yielding. As the material is loaded beyond the first yield point; the yield surface get effected and changes where it can be characterized by its shape, size and orientation in the stress space. In this section the strain hardening of materials is regarded and four hardening models are considered namely; *perfect plasticity*, *isotropic*, *kinematic* and *combined* hardening.

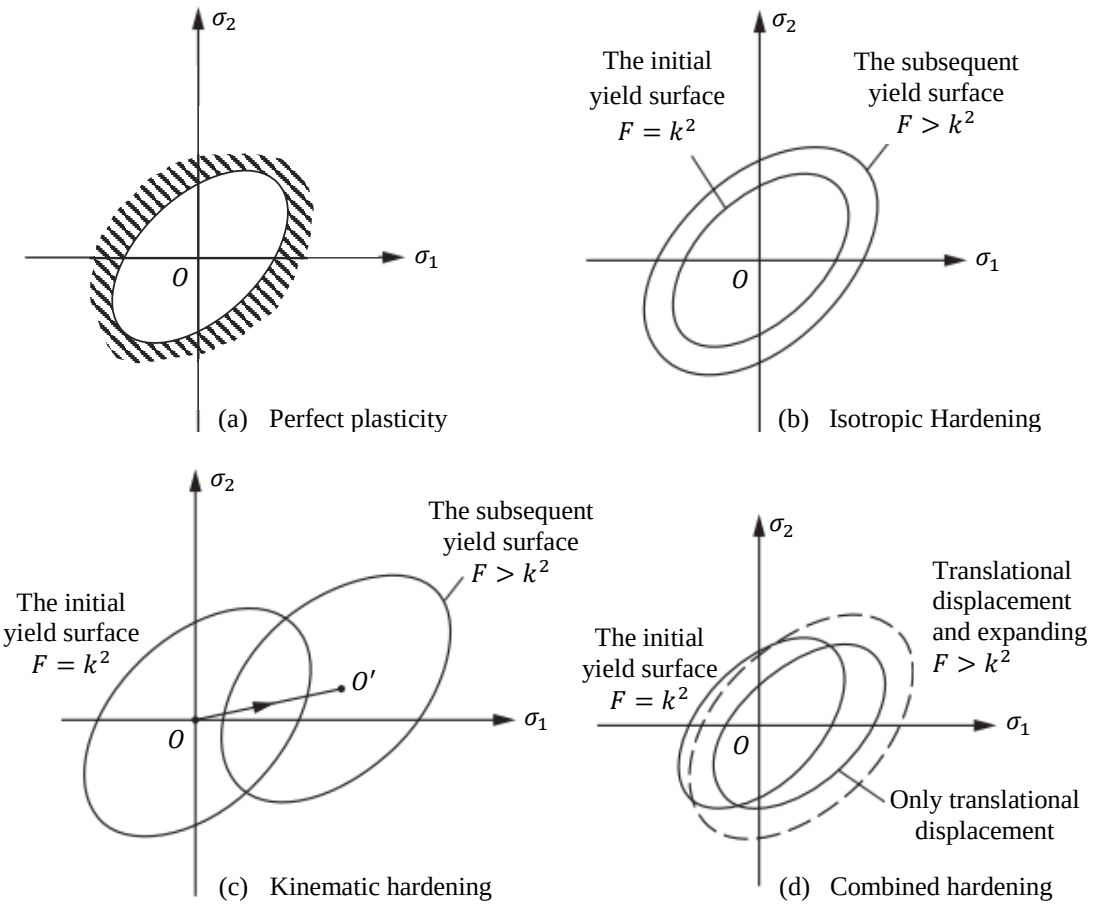

Figure 5.7: Strain hardening model (a) perfect plasticity (b) isotropic strain hardening (c) kinematic strain hardening, and (d) combined strain hardening.

5.3.7.1 Perfect plasticity

A representation of the perfect plasticity in materials is shown in Figure (5.7.a), where one can note that the yield stress σ_y level remains constant and does not depend on the evolution of the plastic strain, this means no hardening is allowed. Moreover, the yield surface ϕ is independent of the degree of plasticity.

5.3.7.2 Isotropic hardening

The evolution of the yield surface is said to be isotropic; if the evolution of the yield surface of the subsequent expands uniformly of the original yield surface Figure (5.7.b). In the isotropic hardening, the yielding depends on the accumulated effective plastic strain e_p, as:

$$\sigma_y = \sigma_y^0 + He_p \tag{5.63}$$

where H is the plastic modulus obtained from the uniaxial stress-strain relationship by the following expression:

$$H = \frac{\delta\sigma}{\delta e_p} \tag{5.64}$$

5.3.7.3 Kinematic hardening

If kinematic hardening model is considered, one can note that the yield surface preserves its shape and orientation. However, the center of the yield surface translates in the stress space as shown in Figure (5.7.c). The evolution of the yield surface for the Von-Mises criterion for the kinematic hardening model is given by:

$$\phi(\sigma, \beta) = \sqrt{3J_2(\boldsymbol{\eta}(\alpha, \beta))} - \sigma_y \tag{5.65}$$

where $\boldsymbol{\eta}(\alpha, \beta) = S(\sigma) - \beta$ is the relative shifted stress tensor; it represent the distance from the center of yield surface to the yield surface, $S(\sigma)$ is the stress deviator and α is known as the *Back-stress tensor*.

5.3.7.4 Combined hardening

The last hardening model is the closest model that approves the reel-life material behaviour. This model can be obtained by combining both the isotropic and kinematic hardening Figure (5.7.d). Under plastic straining, the combined hardening model allows the yield surface to shrink/expand and change its position simultaneously in stress space,

while preserving its shape. A general form of the combined hardening model is defined as:

$$\|\boldsymbol{\eta}\| - \sqrt{\frac{2}{3}}\left[\sigma_y^0 + (1-\beta)\, He_p\right] = 0 \tag{5.66}$$

And the back stress increment is determined by the following expression:

$$\Delta\alpha = \sqrt{\frac{2}{3}}\beta H \Delta e_p \frac{\boldsymbol{\eta}}{\|\boldsymbol{\eta}\|} \tag{5.67}$$

where β is a parameter, equals 1 for kinematic H and 0 for isotropic hardening, respectively.

5.4 Numerical implementation of elastoplasticity model

This section addresses the numerical implementation of the elastoplastic behaviour with the Von-Mises criterion and linear isotropic hardening model that will be adopted for the presented SFR20 element. Small strains are considered in the following study. The numerical implementation of the stress update and the stiffness tangent moduli are essential part to determine the elastoplastic constitutive equations. Back to the assumption of the decomposition of the total strain rate tensor into an elastic $\dot{\varepsilon}^e$ and plastic $\dot{\varepsilon}^p$ strain rate is giving as follows:

$$\dot{\varepsilon} = \dot{\varepsilon}^e + \dot{\varepsilon}^p \tag{5.68}$$

Introducing *Hook's law* to predict the elastic behaviour, the stresses are split into a deviatoric S and hydrostatic p part as:

$$S = 2\mu\dot{\varepsilon}^e = 2\mu\left(\dot{\varepsilon} - \dot{\varepsilon}^p\right) \tag{5.69}$$

$$P = k\ tr\left(\dot{\varepsilon}^e\right) \tag{5.70}$$

where μ and k are denoted the shear and bulk modulus, respectively. The yield function for the Von-Mises criterion with isotropic hardening is given by:

$$\phi\left(\boldsymbol{\eta}, \alpha\right) = \|\boldsymbol{\eta}\| - \sqrt{\frac{2}{3}}\left(\sigma_y + H_{iso}\alpha\right) \leqslant 0 \tag{5.71}$$

In which $\|\boldsymbol{\eta}\|$ is already mentioned. The evolution equations for the plastic strain for the hardening variables are defined as:

$$\dot{\varepsilon^p} = \dot{\lambda}\frac{\partial \phi}{\partial S} \tag{5.72}$$

$$\dot{\alpha} = \sqrt{\frac{2}{3}}\dot{\lambda} \tag{5.73}$$

$$\dot{\beta} = -\frac{2}{3}H_{kin}\dot{\lambda}\frac{\partial \phi}{\partial S} \tag{5.74}$$

In the following study an implicite integration method such as *the Backward Euler Method* is used to solve the elastoplastic differential equations. Since, they are stiff in the mathematical sense [97]. The method consist to find the solution by solving an equation in the current state of the system t_n and the later one t_{n+1}, corresponding to a typical (pseudo-) time increment $[t_n, t_{n+1}]$. After applying the Backward Euler method, the evolution equations for the variables (5.72, 5.73, 5.74) are reformulated as:

$$\varepsilon^p_{n+1} = \varepsilon^p_n + \Delta\lambda \mathbf{n}_{n+1} \tag{5.75}$$

$$\alpha_{n+1} = \alpha_n + \sqrt{\frac{2}{3}}\Delta\lambda \tag{5.76}$$

$$\beta_{n+1} = \beta_n - \frac{2}{3}H_{kin}\Delta\lambda \mathbf{n}_{n+1} \tag{5.77}$$

where $\Delta\lambda = \lambda_{n+1} - \lambda_n$ and $\mathbf{n} \equiv N(\sigma, A)$. The deviatoric stresses at time step t_{n+1} are expressed by:

$$S_{n+1} = 2\mu\left(\varepsilon_{n+1} - \varepsilon^p_{n+1}\right) \tag{5.78}$$

By substituting Equation (5.72) into Equation (5.78) leads to:

$$S_{n+1} = 2\mu\left(\varepsilon_{n+1} - \varepsilon^p_{n+1}\right) - 2\mu\Delta\lambda \mathbf{n}_{n+1} \tag{5.79}$$

At this stage the solution of Equations (5.72, 5.73, 5.74) and (5.79) are not an easy task since the inequality constrain $\phi(\boldsymbol{\eta}_{n+1}, \alpha_{n+1}) \leqslant 0$ should be fullfiled. An effective and robust algorithm called *the radial return-mapping* [105] is used to formulate the constitutive equations. The method is subdivided into two steps. First step, is called *the elastic-predictor* or an elastic prediction of the stresses. At this stage the plastic variables at the beginning of a time step from t_n to t_{n+1} are assumed as fixed. This assumption results in the trial state in which the evolution Equations (5.78, 5.73, 5.74) are updated as follows:

$$S_{n+1}^{trail} = 2\mu \left(\varepsilon_{n+1}^{trail} - \varepsilon_n^p\right) \tag{5.80}$$

$$\boldsymbol{\eta}_{n+1}^{trail} = S_{n+1}^{trail} - \beta_n \tag{5.81}$$

$$\alpha_{n+1}^{trail} = \alpha_n \tag{5.82}$$

where the subscript $(\bullet)^{trail}$ stands for *trail* quantities which is being fixed for a moment. The relations (5.80, 5.81, 5.82) can be used to check the behaviour status is an elastic or plastic. For this, a trail state is inserted into the yield function:

$$\phi\left(\boldsymbol{\eta}_{n+1}^{trail}, \alpha_{n+1}^{trail}\right) = \|\boldsymbol{\eta}_{n+1}^{trail}\| - \sqrt{\frac{2}{3}}\left(\sigma_y + H_{iso}\alpha_n\right) \quad \begin{cases} \leqslant 0 & \Rightarrow \quad elastic \\ > 0 & \Rightarrow \quad plastic \end{cases} \tag{5.83}$$

In the case where the deviatoric stress S_{n+1}^{trail} fulfils the yield condition within the time interval $[t_n, t_{n+1}]$, i.e. $\phi\left(\boldsymbol{\eta}_{n+1}, \alpha_{n+1}\right) \leqslant 0$, the material behaviour is purely elastic and the constitutive variables are updated as:

$$S_{n+1} = S_{n+1}^{trail} \tag{5.84}$$

$$\varepsilon_{n+1}^p = \varepsilon_n^p \tag{5.85}$$

$$\beta_{n+1}^{trail} = \beta_n \tag{5.86}$$

$$\alpha_{n+1} = \alpha_n \tag{5.87}$$

Otherwise, if $\phi\left(\boldsymbol{\eta}_{n+1}, \alpha_{n+1}\right) > 0$, the material shows an elastoplastic behaviour within the time step t_{n+1} and the stress state has to be corrected to satisfies the yield condition, this second step is called *plastic-corrector*; if the predicted stress exceeds the yield surface, a correction of the stresses has to be applied. This leads to the definition of the trial and the adapted deviatoric part of the relative stresses, as following:

$$S_{n+1} - \beta_{n+1} = \boldsymbol{\eta}_{n+1}^{trail} - \left(\frac{2}{3}H_{kin} + 2\mu\right)\Delta\lambda\boldsymbol{\eta}_{n+1} \tag{5.88}$$

$$\|\boldsymbol{\eta}_{n+1}\| = \|\boldsymbol{\eta}_{n+1}^{trail}\| - \left(\frac{2}{3}H_{kin} + 2\mu\right)\Delta\lambda \tag{5.89}$$

By inserting Equation (5.89) into the yield condition Equation (5.71) gives:

$$\phi_{n+1} = \|\boldsymbol{\eta}_{n+1}^{trail}\| - \left(\frac{2}{3}H_{kin} + 2\mu\right)\Delta\lambda - \sqrt{\frac{2}{3}}\left[\sigma_y + H_{iso}\left(\alpha_n + \sqrt{\frac{2}{3}}\Delta\lambda\right)\right] = 0 \quad (5.90)$$

The plastic multiplier within the current time step t_{n+1} can be calculated by rearranging the previous equation of the yield condition to have the following form:

$$\Delta\lambda = \frac{\sqrt{\frac{2}{3}}\sigma_y + H_{iso}\alpha_n}{2\mu\left(1 + \frac{H_{iso} + H_{kin}}{3\mu}\right)} \quad (5.91)$$

At this stage since the plastic flow is known, one can determine the stresses, the plastic strain and the internal variables can be computed from (5.72, 5.73, 5.74). Then, the actual stresses are given by:

$$\sigma_{n+1} = k\ tr\left(\varepsilon\right) + 2\mu\left(\varepsilon_{n+1} - \varepsilon_n^p\right) - 2\mu\Delta\lambda\mathbf{n}_{n+1}^{trail} \quad (5.92)$$

After, determining the actual stresses, the expression for the elastoplastic Consistent Tangent Operator with the Von-Mises model and isotropic hardening is expressed as:

$$\begin{aligned} C^{ep} &= \frac{\partial\sigma_{n+1}}{\partial\varepsilon_{n+1}} \\ &= C_{n+1}^e - 2\mu\mathbf{n}_{n+1}^{trail} \otimes \frac{\partial\Delta\lambda}{\partial\varepsilon_{n+1}} - 2\mu\Delta\lambda\frac{\partial\mathbf{n}_{n+1}^{trail}}{\partial\varepsilon_{n+1}} \end{aligned} \quad (5.93)$$

where C^e is the elasticity tensor with the explicit definition:

$$C_{n+1}^e = k\ \mathbf{1}\otimes\mathbf{1} + 2\mu\left(\mathbf{I} - \frac{1}{3}\mathbf{1}\otimes\mathbf{1}\right) \quad (5.94)$$

where I is the identity matrix. More details on the derivation of $\frac{\partial\Delta\lambda}{\partial\varepsilon_{n+1}}$ and $\frac{\partial\mathbf{n}_{n+1}^{trail}}{\partial\varepsilon_{n+1}}$ are given in the following section.

5.5 Elastoplastic Consistent Tangent Operator

The following section presents the explicit derivation of the following $\frac{\partial\Delta\lambda}{\partial\varepsilon_{n+1}}$ and $\frac{\partial\mathbf{n}_{n+1}^{trail}}{\partial\varepsilon_{n+1}}$ components of the elastic-plastic tangent modulus which have been introduced in Equation (5.93), by applying the chain rule on both derivatives we get:

$$\frac{\partial \Delta\lambda}{\partial \varepsilon_{n+1}} = \frac{\partial \Delta\lambda}{\partial f_{n+1}^{trial}} \frac{\partial f_{n+1}^{trial}}{\partial \boldsymbol{\eta}_{n+1}^{trial}} \frac{\partial \eta_{n+1}^{trial}}{\partial \varepsilon_{n+1}} \tag{5.95}$$

$$a_1 = \frac{\partial \Delta\lambda}{\partial f_{n+1}^{trial}} = \left(2\mu\left(1 + \frac{H_{iso} + H_{kin}}{3\mu}\right)\right)^{-1} \tag{5.96}$$

$$a_2 = \frac{\partial f_{n+1}^{trial}}{\partial \boldsymbol{\eta}_{n+1}^{trial}} = \frac{\partial \|\boldsymbol{\eta}_{n+1}^{trial}\|}{\partial \boldsymbol{\eta}_{n+1}^{trial}} = \frac{1}{2}\left(\Sigma_{i=1}^{n}\left(\boldsymbol{\eta}_{n+1,i}^{trial}\right)^2\right)^{-\frac{1}{2}} 2\boldsymbol{\eta}_{n+1,i}^{trial} = \mathbf{n}_{n+1}^{trial} \tag{5.97}$$

$$a_3 = \frac{\partial \boldsymbol{\eta}_{n+1}^{trial}}{\partial \varepsilon_{n+1}} = 2\mu \tag{5.98}$$

The first derivative became:

$$\frac{\partial \Delta\lambda}{\partial \varepsilon_{n+1}} = \left(1 + \frac{H_{iso} + H_{kin}}{3\mu}\right)^{-1} \mathbf{n}_{n+1}^{trial} \tag{5.99}$$

Calculating the last derivation part;

$$\begin{aligned} \frac{\partial \mathbf{n}_{n+1}^{trail}}{\partial \varepsilon_{n+1}} &= \frac{\partial \mathbf{n}_{n+1}^{trail}}{\partial \mathbf{S}_{n+1}} \frac{\partial \mathbf{S}_{n+1}}{\partial \varepsilon_{n+1}} \\ &= \frac{2\mu}{\|\boldsymbol{\eta}_{n+1}^{trail}\|}\left[\mathbf{I} - \mathbf{n}_{n+1}^{trail} \otimes \mathbf{n}_{n+1}^{trail}\right] \end{aligned} \tag{5.100}$$

By substituting the derivatives in Equations (5.99) and (5.100). Add to that, the explicit form of the elasticity matrix in Equation (5.94) into Equation (5.93), we get the algorithmic Consistent Tangent Modulus for the J_2-elastic-plastic material for the presented SFR20 element, as:

$$C_{n+1}^{ep} = k\mathbf{1} \otimes \mathbf{1} + 2\mu A_{n+1}\left(\mathbf{I} - \frac{1}{3}\mathbf{1} \otimes \mathbf{1}\right) - 2\mu B_{n+1}\mathbf{n}_{n+1}^{trial} \otimes \mathbf{n}_{n+1}^{trial} \tag{5.101}$$

where

$$A_{n+1} = 1 - \frac{2\mu\Delta\lambda}{\|\boldsymbol{\eta}_{n+1}^{trail}\|} \tag{5.102}$$

and

$$B_{n+1} = \left(1 + \frac{H_{kin} + H_{iso}}{3\mu}\right)^{-1} - \frac{2\mu\Delta\lambda}{\|\boldsymbol{\eta}_{n+1}^{trail}\|} \tag{5.103}$$

5.6 Computational implementation of elastoplasticity by the Finite element method

The computation of elastoplastic behaviour of materials by the Finite Element Method is generally carried out by means of an increment-iterative solution procedure. In which the load and/or imposed displacements are gradually applied in increments. Where the equilibrium is sought at each load level by minimising the force residual, i.e. the difference between the external and internal forces. An iterative process is carried out until the residual is smaller than a prescribed number. The Newton-Raphson algorithm is an efficient method for establishing equilibrium, and it has been adopted for all the finite element calculation in this part of the work for nonlinear analysis. The incremental method consist on dividing the applied external charge in terms of a certain number of increments in which they are small enough to consider a nonlinear problem to an approximated linear problem. A simple way to manage incremental analysis is to introduce the pseudo-time parameter noted t, which is used to describe a particular loading program. In the following work deformations are assumed as infinitesimal. Thus, the total displacements and strains at load increment t_{n+1} after adding all incremental displacements and strains, are given by:

$$U_{n+1} = U_n + \Delta U \tag{5.104}$$

and

$$\{\varepsilon_{n+1}\} = \{\varepsilon_n\} + \Delta\varepsilon \tag{5.105}$$

Since the increment equilibrium is examine by minimising the force residual, that is the difference between the external and internal forces, we define the *residual* (or *out-of-balance force*) vector as:

$$\{r\,(\Delta U)\} \equiv \mathop{\mathbf{A}}_{i=1}^{e} \int_{V_{n+1}}^{e} [B]_{n+1}^{T} \{\sigma\}_{n+1}\, dV^e - \{F\}_{n+1}^{ext} = 0 \tag{5.106}$$

where $\{\sigma\}_{n+1}$ is the internal force vector which is a nonlinear function of the vector of nodal unknowns ΔU.

Incremental analysis tends to provide the value of the displacement increment ΔU corresponding to the chosen load increment ΔF^{ext}. This is accomplished by building and solving the linear problem equivalent to each load step:

$$K_T\,(U_n)\,\Delta U_{n+1} = \Delta F_{n+1}^{ext} \tag{5.107}$$

where K_T is the tangent stiffness at configuration U_n.

The Newton-Raphson method is used to find the roots of the nonlinear Equation (5.107) by iteratively improving an initial guess. The method is based on the idea of linearizing the nonlinear equation at the current guess and solving the resulting linear equation to obtain a better guess. The method can be expressed mathematically as follows:

Let $f(x)$ be a nonlinear function, and let x_i be an initial guess for the root. The Newton-Raphson method seeks to find a better guess x_{i+1} by solving the linearized equation:

$$f(x_i) + f'(x_i)(x_{i+1} - x_i) = 0 \quad ; \quad i = 1, 2, ... \tag{5.108}$$

where $f'(x_i)$ is the derivative of $f(x)$ evaluated at x_i. Solving for x_{i+1} yields:

$$x_{i+1} = x_i - \frac{f(x_i)}{f'(x_i)} \quad ; \quad i = 1, 2, ... \tag{5.109}$$

Figure 5.8 demonstrate that the method can give quadratic convergence $f(\bar{x}) = 0$ to the solution, if three conditions are satisfied: the tangent of the function must not equal zero $f'(x) \neq 0$ and it must be continues in same interval of the increment. In addition, the initial guess should be close to the root $x = \bar{x}$.

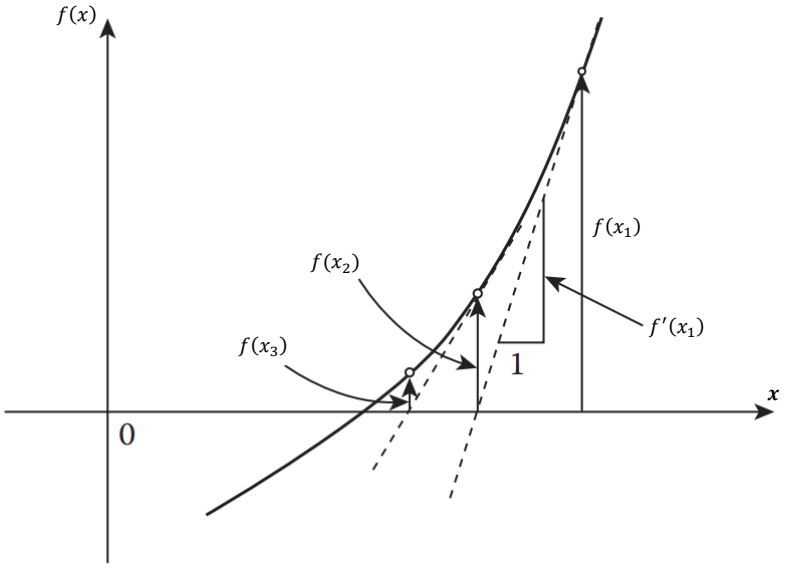

Figure 5.8: Representation of the Newton-Raphson iteration in one variable.

The discrete version of solving the nonlinear equilibrium model by the Newton-Raphson scheme by typical iteration (k), gives:

$$K_T \Delta U^k = -r^{(k-1)} \tag{5.110}$$

where the residual can be written by:

$$r^{(k-1)} \equiv F^{int}(U_{n+1}^{k-1}) - F_{n+1}^{ext} \tag{5.111}$$

and

$$K_T \equiv \int_V B^T C^{ep} B dV = \frac{\partial r}{\partial U_{n+1}} \mid_{U_{n+1}^{k-1}} \tag{5.112}$$

The global displacement in term of displacement *increments* is expressed as:

$$U_{n+1}^k = U_n + \Delta U^k \tag{5.113}$$

where ΔU^k is the incremental displacement vector:

$$\Delta U^k = \Delta U^{k-1} + \delta U^k \tag{5.114}$$

The process as illustrated in Figure 5.9 is repeated until a desired level of accuracy is achieved. Thus, the iterations are repeated until the residual r is less than a specified convergence tolerance or *equilibrium convergence tolerance* ϵ, which is expressed by:

$$\frac{\mid r^{iter} \mid}{\mid F_{n+1}^{ext} \mid} \leqslant \epsilon_{tol} \tag{5.115}$$

where *iter* is the number of iteration for each increment, and ϵ_{tol} should be sufficiently small.

The method can converge very quickly if the initial guess is close to the root and if the function is well-behaved. However, if the function is not well-behaved, the method may fail to converge.

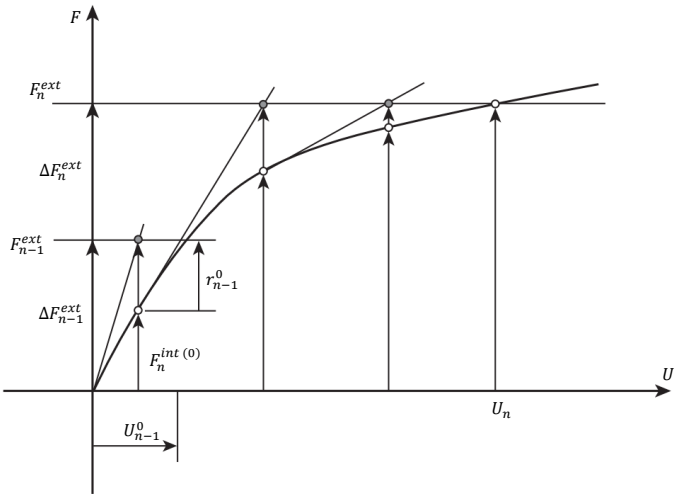

Figure 5.9: Incremental-iterative Newton-Raphson method.

Chapter 6

Validation of high order SFR elements in elastoplasticity

Summary

6.1 Introduction

This chapter presents the validation of the performance of the conforming SFR20 element for the analysis of elastoplastic behavior of structures. These element uses a reduced integration schemes with $3 \times 3 \times 3$ Gauss points and it was previously developed and validated for the analysis of linear problems and it showed good performance through a series of benchmark tests. In the following chapter the presented element SFR20 is tend to be validated by using two integration schemes; the reduced integration and a full integration scheme with $4 \times 4 \times 4$ Guass points where this element is denoted as SFR20F. The presented element is implemented in the commercial finite element software *Abaqus* as user subroutine (see Appendix B for more details on Abaqus implementation tutorial); this software provide the facility for users to specify their own elements and material models. The correctness of the implementation and performance of the presented element was assessed by examining different type of analysis with respect to the Abaqus C3D20

element. The constitutive model adopted for all analysis in this chapter is the Von-Mises plasticity criterion with isotropic hardening.

6.2 One element analysis

The purpose of performing the one element test is to validate the computational implementation of the UEL and UMAT subroutine with the proposed elements SFR20 and SFR20F, and to investigate their performance in coarse meshes. The problem represent a block of material an it is modelled with one element. This single element tested in the case of simple uniaxial tension and compression using both displacement and force control. The main reason for applying these series of tests is that there is a variety of problems uses displacement and force control. Therefore, it is reasonable to confirm that the implementation works properly in these type of problems.

Figure 6.1 shows the boundary conditions and the geometry of the structure where $a = 100\ mm$. The properties of the material are : Young modulus $E = 216\ GPa$ and Poisson's ration $\nu = 0.3$. For all the analysis performed we use a von Mises elastoplastic material with linear isotropic hardening whose parameters are defined in the Table 6.1, these parameters are generated by the following expression $\sigma_y\left(\varepsilon_p\right) = 0.243 + 0.2\varepsilon_p\ (GPa)$.

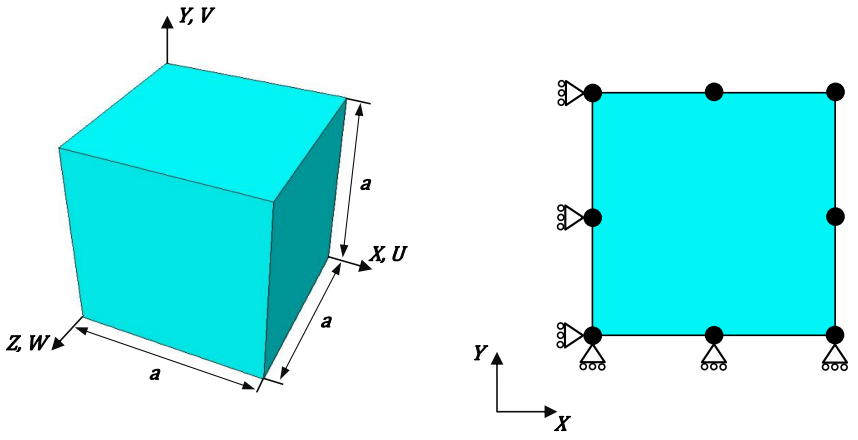

Figure 6.1: One element test: (a) 3D view with geometry definition, (b) XY plan view with boundary conditions.

Figure 6.2 shows the uniaxial tension case, a displacement and force control was applied on the upper surface of the element subjecting the element into uniaxial tension. Figure 6.2.a and Figure 6.2.b represent uniaxial tension with displacement control and force control, respectively. Both Figures shows the undeformed and deformed configurations along with the boundary conditions that used in the analysis. The evolution of the Von-Mises stress with respect to the Logarithmic strain is traced in Figure 6.2.

Uniaxial compression results are presented in Figure 6.3. As like the tension test a displacement and force control was applied on the upper surface of the element subjecting the element into uniaxial compression. The undeformed and deformed configurations are shown in Figure 6.3.a and Figure 6.3.b. In addition to that, The evolution of the Von-Mises stress with respect to the Logarithmic strain for uniaxial compression with displacement and force control are traced in the same Figures, respectively. In the case of compression with force control, the results of the SFR20F element are very close to SFR20 element, for the sake of brevity they were not presented.

Table 6.1: Elastoplastic material data for one element test.

ε	$\sigma\ (GPa)$
0.0	0.243
0.1	0.263
0.4	0.323
0.8	0.403
1.3	0.503
1.9	0.623

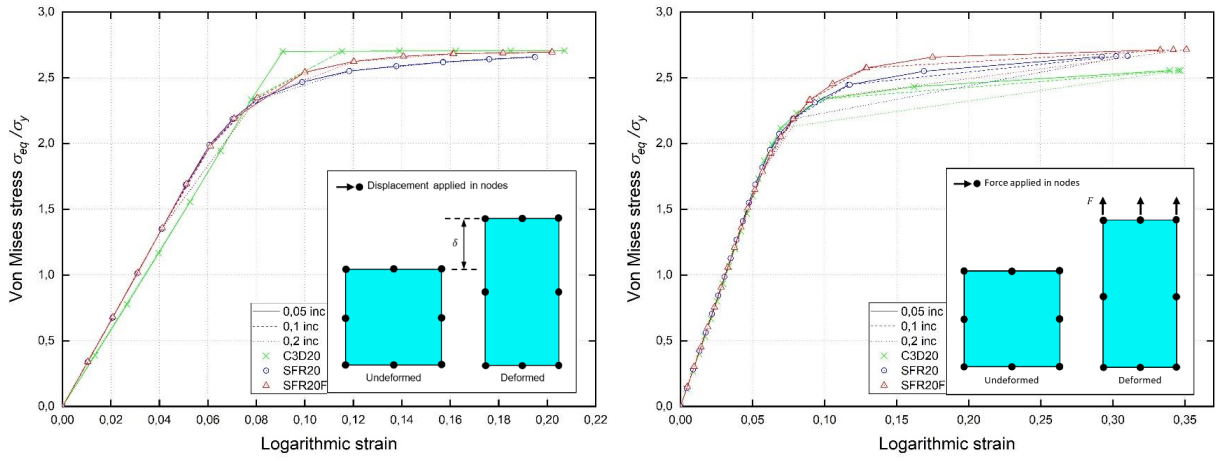

(a) (b)

Figure 6.2: The stress (Von Mises) - strain (equivalent Logarithmic strain) curve for uniaxial tension case : (a) displacement control, (b) force control.

Figures 6.2 and 6.3 shows that the presented elements and Abaqus C3D20 element are in good agreement verifying that the presented elements are implemented correctly within the subroutines. Concerning the performance of the SFR20 and SFR20F, for the displacement and force control configurations for both tests (Uniaxial tension and compression) and for the same displacement field and force magnitude, we find that the presented elements gives good results comparing to the reference Abaqus C3D20 element.

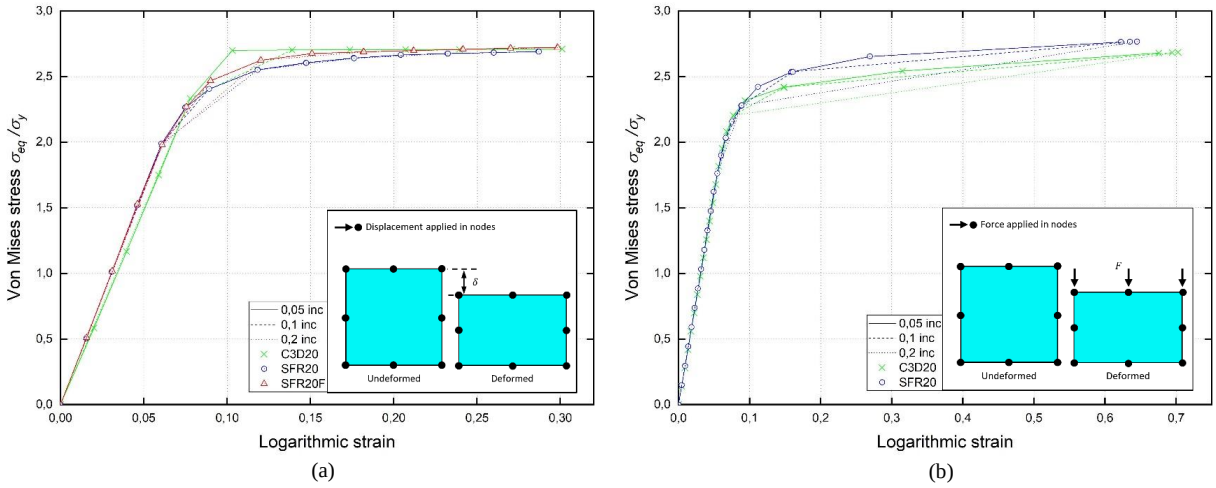

Figure 6.3: The stress (Von Mises) - strain (equivalent Logarithmic strain) curve for uni-axial compression case : (a) displacement control, (b) force control.

6.3 Bending of clamped beam

In the following test, a straight beam is studied and modelled to assess the performance of the proposed elements. The beam is clamped from one end and subjected to vertical shear force at its free edge as depicted in Figure 6.4. The beam has the following geometric values: The length $L = 1000\ mm$, the width $h = 100\ mm$ and a thickness $b = 50\ mm$. The mechanical properties are: Young Modulus $E = 210\ GPa$, Poisson's ration $\nu = 0.3$ and yielding point $\sigma_y = 0.24\ GPa$. The material was assumed as elastic-perfectly plastic. The beam is modeled with a regular mesh $(50 \times 2 \times 1)$ elements, this test is conducted to investigate the performance of the proposed elements SFR20 and SFR20F with respect to the 20-node hexahedral C3D20 Abaqus element. The beam is subjected and tested for two different loading cases :

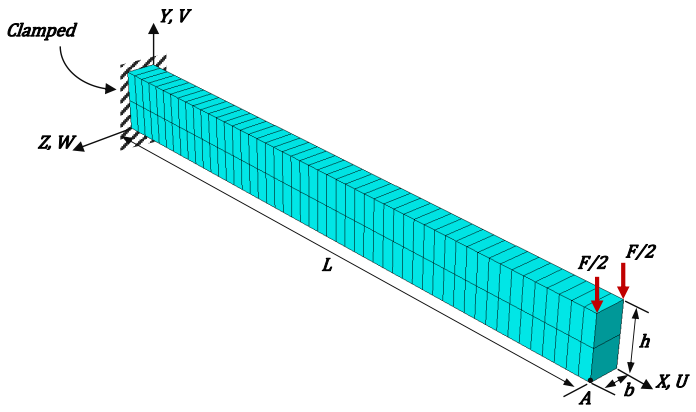

Figure 6.4: Clamped cantilever beam geometry, modelled with $50 \times 2 \times 1$ elements.

- **First case:** The plate is loaded at its free end with concentrated force where the analytical limit load is given by [98] :

$$F_{lim} = \frac{\sigma_y b h^2}{4L} \tag{6.1}$$

- **Second case:** The beam is subjected to cyclic loading, where the free end is imposed to concentrated force, the evolution with time of the proportional load coefficient amplifies the imposed concentrated force according to the graph illustrated in Figure 6.5. Simulating five cycle loading program in bending of the structure.

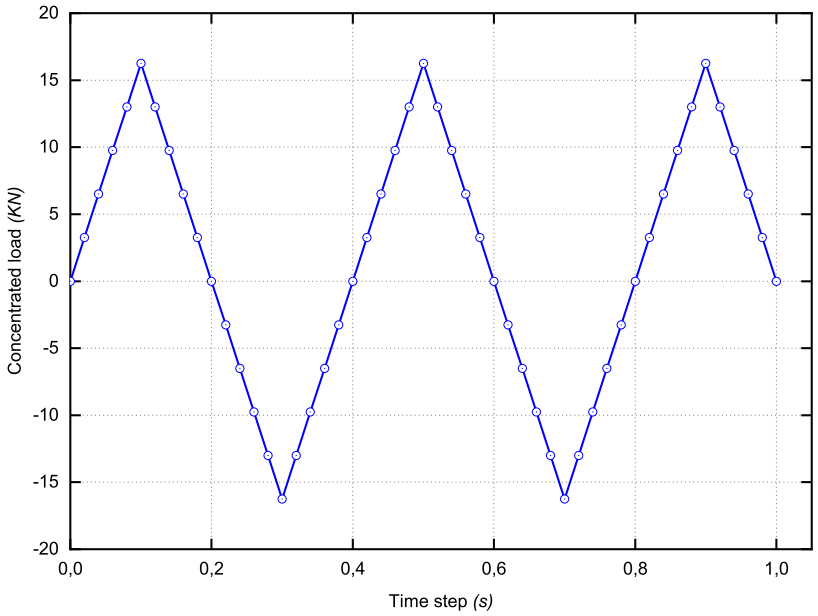

Figure 6.5: Clamped cantilever beam: cycle loading program for concentrated force.

Figure 6.6 shows the results for the first case of the analysis, where it represent the vertical displacement of point A with respect to the applied load. One can note that the results of the presented elements are identical with the results of the Abaqus C3D20 element. The load level for all element at the end of the last increment is $F \approx 32.4985\ KN$. At this stage of load the cantilever beam is effectively collapsing and equilibrium can no longer be found. The evolution of the Von Mises stress and the equivalent plastic strain are demonstrated in Figure 6.7 for the presented elements and for the C3D20 Abaqus element for different loading increments, respectively.

The presented elements gives almost the same results in capturing the Von Mises stress and plastic strain evolution, for the sake of brevity, the results of the SFR20F are not presented. Overall, the presented element SFR20 shows good performance in capturing the plastic deformation.

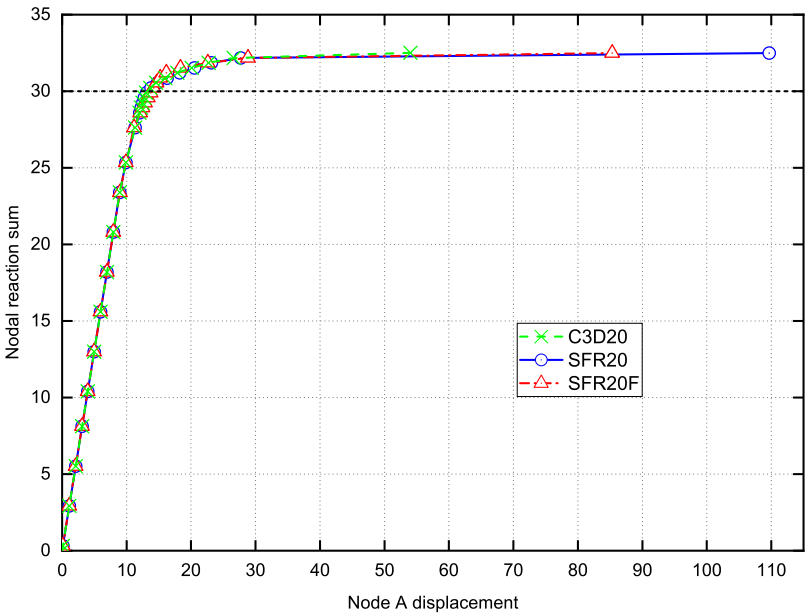

Figure 6.6: Clamped cantilever beam: displacement at point A of the beam versus applied force.

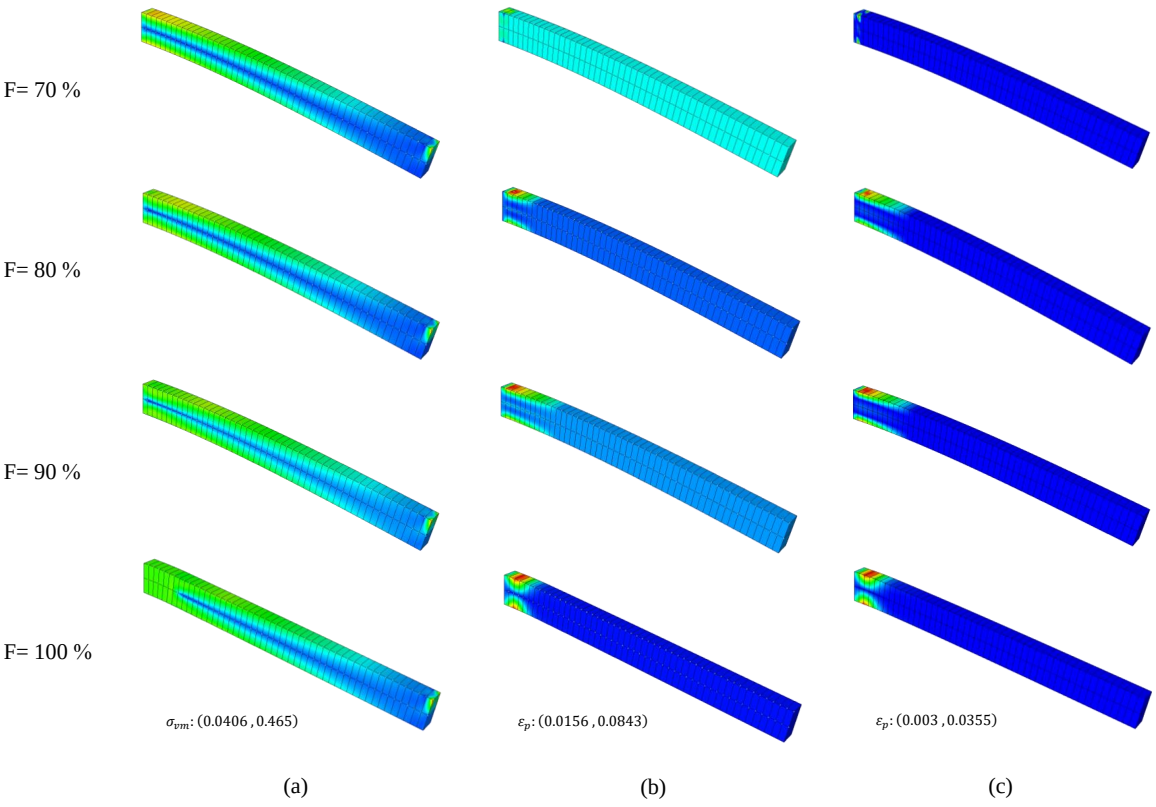

Figure 6.7: Clamped cantilever beam: (a) Von-Mises stress with SFR20 element (b) evolution of equivalent plastic strain for SFR20 element (c) evolution of equivalent plastic strain for C3D20 element. Post-processing of results was made by UMAT implementation for the presented elements. 100% Averaging of results.

The initial yield surface locus with respect to the yield locus for the presented SFR20 element is demonstrated in Figure 6.8. We note that the principle stresses move on the yield surface when the material is assumed to be perfectly plastic. However, for isotropic hardening, the principal stresses exceed the yield surface where the yield surface itself expands.

The results for the second case of the analysis, where the beam is subjected to cyclic loading are illustrated in Figure 6.9. It can be say that the best rate of displacement is obtained by the presented elements SFR20 and SFR20F comparing to the C3D20 element for the same cyclic loading.

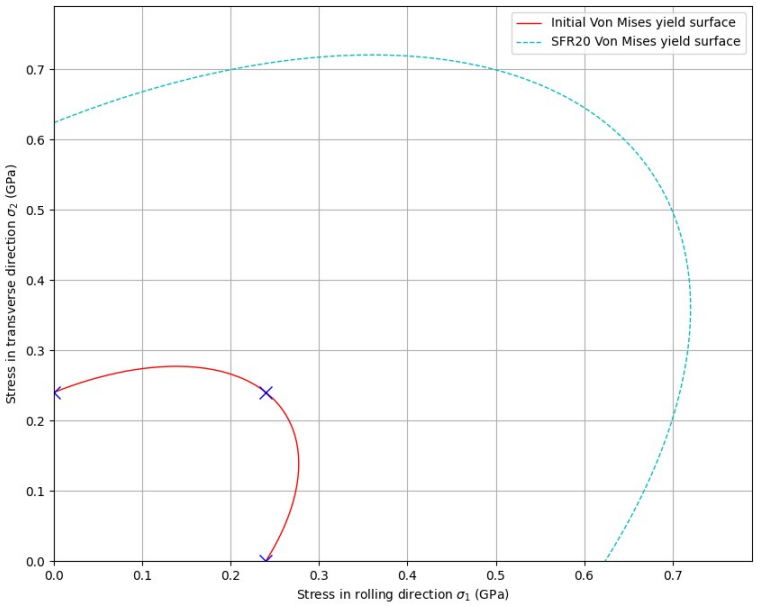

Figure 6.8: Clamped cantilever beam: Von Mises yield locus with evolution of principal stresses.

6.4 Perforated plate

Figure 6.10 shows a perforated plate considered as made from a homogeneous, isotropic elastic-perfectly plastic material. The test is a popular benchmark to assess the developed element for its precision and effectiveness, and it was conducted by many authors such as [66, 73, 98] and expremently [106]. The geometry of the structure is considered as: $W = 10\ mm$, $L = 18\ mm$, the plate thickness $T = 1\ mm$ and circular hole with a radius $r = 5\ mm$. The given material properties for the plate are: Young's modulus $E = 7000\ GPa$, Poisson's ratio $\nu = 0.2$ and yielding point $\sigma_y = 24.3\ GPa$. Because of the symmetry only a quarter of the structure is modelled, where the mesh and boundary conditions are depicted in Figure 6.10. The perforated plate problem is studied with two loading cases :

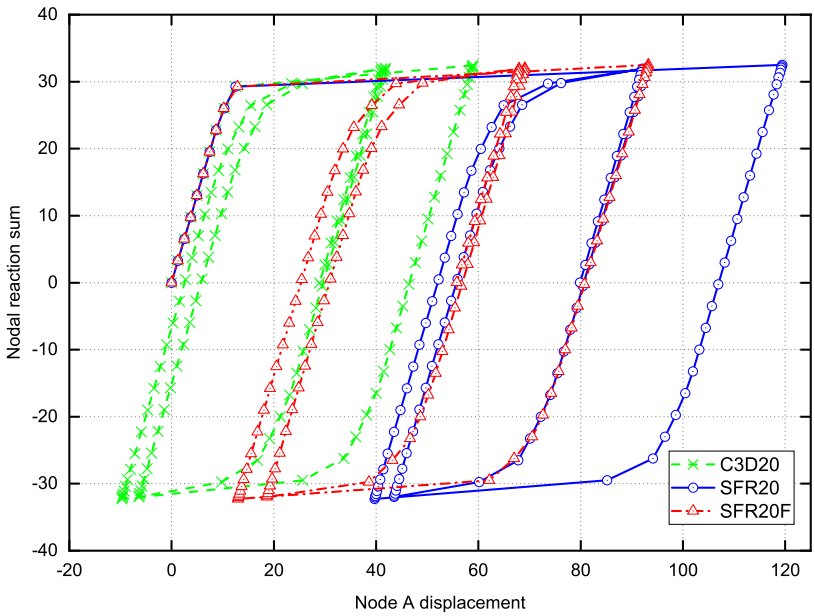

Figure 6.9: Clamped cantilever beam subjected to cyclic loading: cyclic response for isotropic hardening.

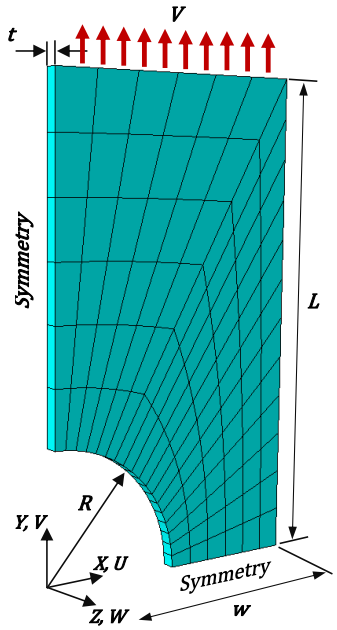

Figure 6.10: Perforated plate: geometry, boundary conditions with non uniform mesh.

- **First case:** The plate is subjected to stretching along its longitudinal axes with a uniform displacement control on the upper boundary where the displacement magnitude is $v = 0.1$;
- **Second case:** The plate is subjected to cyclic loading, where the upper boundary is stretched with imposed displacement $\widehat{v} = 0.1$, the evolution with time of the

proportional load coefficient amplifies the imposed displacement according to the graph illustrated in Figure 6.11. Simulating one-cycle loading program in tension and compression of the structure.

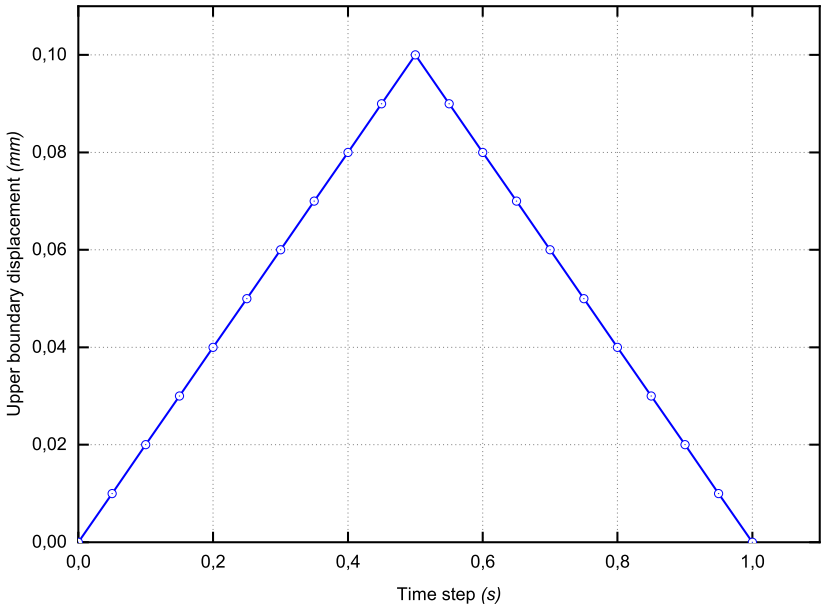

Figure 6.11: Perforated plate: One cycle loading program.

Figures 6.12 and 6.13 illustrate the evolution of the Von-Mises stress for the SFR20 element and the plastic strains for different time increments starting from the first appearance of the plastic deformation for both element SFR20 and C3D20, respectively. The results are indicated in Gauss points for different time increment.

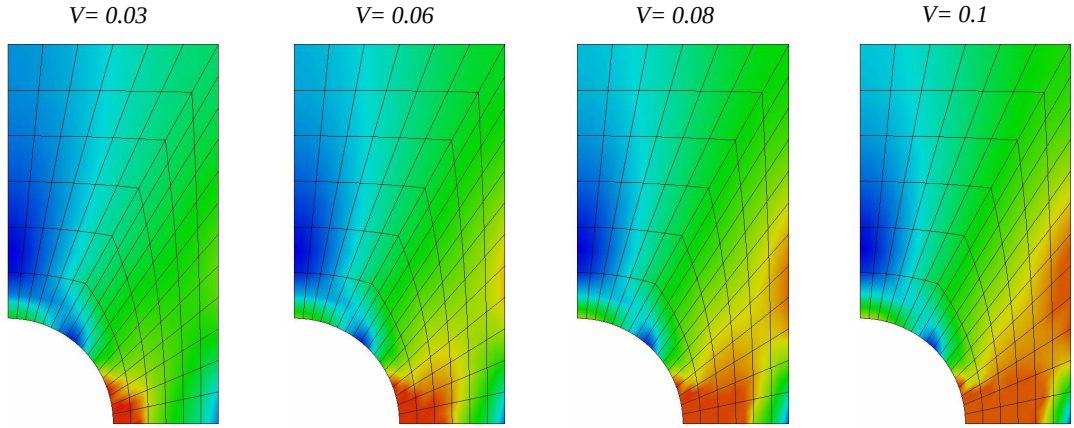

Figure 6.12: Perforated plate : Evolution of the Von-Mises stress with SFR20 element. Post-processing of results was made by UMAT implementation for SFR20 element. 100% Averaging of results.

For the purpose of brevity the results of the SFR20F are not illustrated and plotted, because they are almost identical to the reduced integration SFR20 element. Both elements SFR20 and C3D20 captures a value of $\sigma_{vm} = 24.3$ for the Von-Mises stress in the last increment. In the other hand, the plastic deformation for the presented element SFR20 was captured when the displacement reaches 30% of the total displacement with a value of $\varepsilon_p = 0.0027$, and in the last increment the plastic strain became $\varepsilon_p = 0.0912$. The C3D20 element captures the plastic deformation when the displacement reaches 30% of the total displacement with a value of $\varepsilon_p = 0.0028$, and it get increased until the last increment with a value of $\varepsilon_p = 0.0898$.

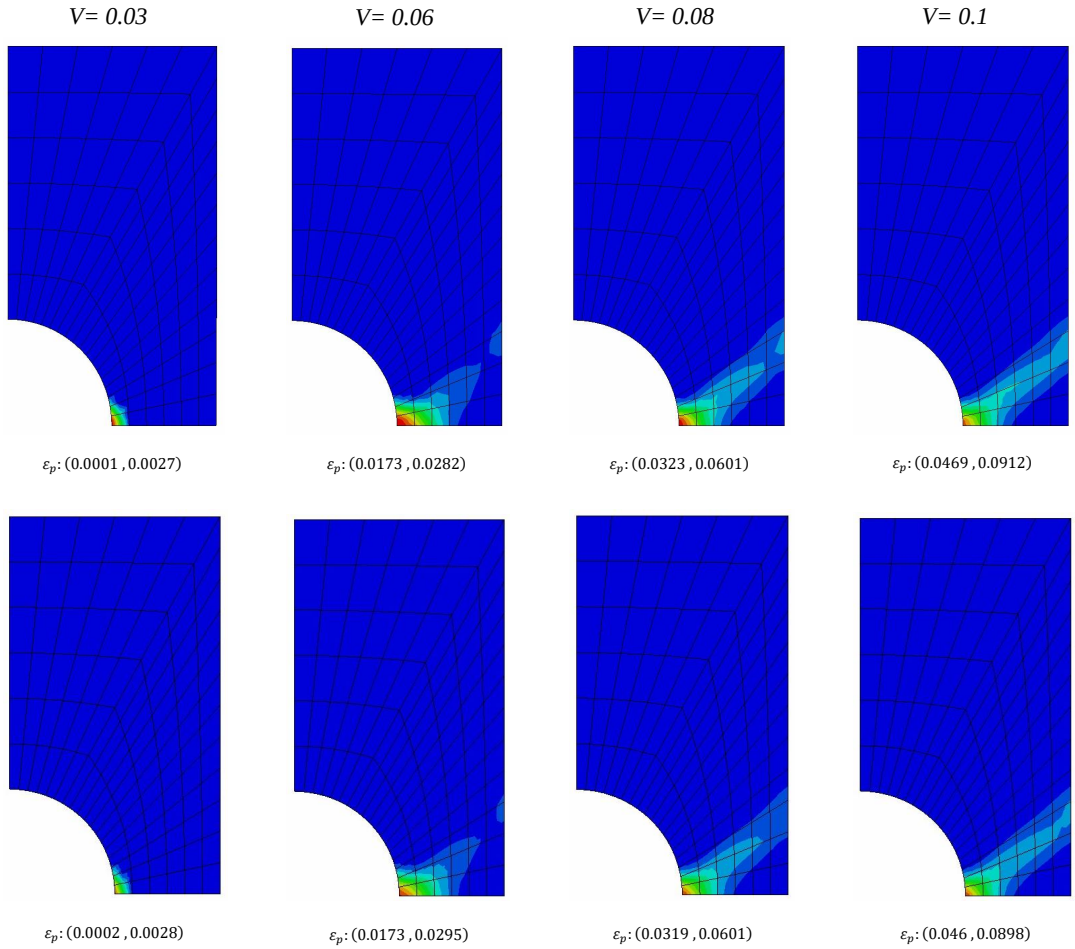

Figure 6.13: Perforated plate : Evolution of the plastic strain upper row with SFR20 element, plastic strain lower row with C3D20 element. Post-processing of results was made by UMAT implementation for SFR20 element. 100% Averaging of results.

The results obtained from the displacement of the upper edge versus the nodal reactions are traced in Figure 6.14.a and the true distance calculated in the center of the plate along the length with respect to the upper edge displacement is illustrated in Figure 6.14.b. As it can be noted from the Figures, the results obtained from the presented SFR20 element are identical with the C3D20 *Abaqus* element. The cyclic response for

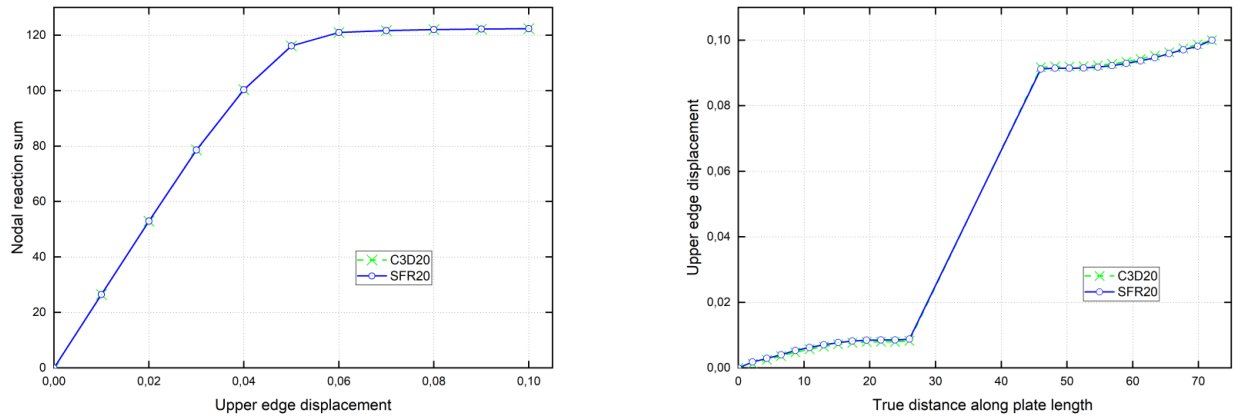

(a) (b)

Figure 6.14: Perforated plate: (a) displacement-force curves, (b) True distance in plate center along the length versus upper edge displacement.

isotropic hardening with perfect plasticity is shown in Figure 6.15. It is clear that both elements SFR20 and C3D20 are in good agreement in results for the cyclic loading case.

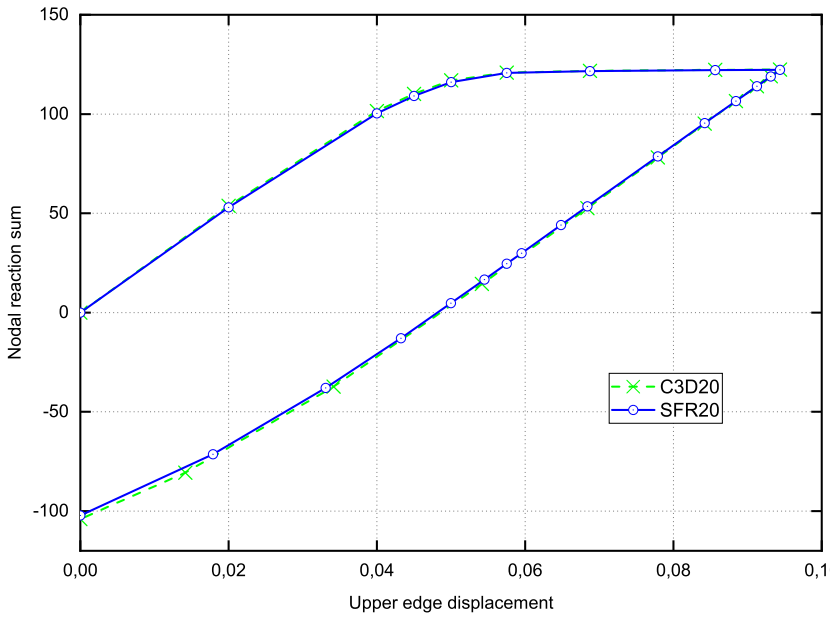

Figure 6.15: Perforated plate subjected to cyclic loading: cyclic response for isotropic hardening.

Chapter 7

General conclusion

This research aimed to formulate and assess the effectiveness of two novel 20-node hexahedral solid finite elements: a conforming element SFR20 and a non-conforming element SFR20I. Both elements are part of the family grounded in the Space Fiber Rotation concept. This conceptual framework involves a fundamental 3D rotation of a virtual fiber within the element, enhancing the definition of the displacement field approximation. Consequently, this methodology introduces additional rotational degrees of freedom per node. To address Poisson's locking deficiency, the incompatible modes approach was incorporated into the non-conforming element SFR20I.

This thesis covers key themes of the research topic. In this context, in the first chapter a bibliographic synthesis was established at the start of this work in order to present the different formulations proposed in finite elements developments. Basic notions on the continuum mechanics and the finite element method was addressed in the second chapter. The third chapter present the Space Fiber Rotation concept formulation and the process of developing the presented elements. In order to evaluate the performance of the SFR20 and SFR20I elements, a series of standard linear test cases in the literature was conducted in chapter four. The theory of plasticity and the formulation of the elastoplastic model is addressed in chapter five. this chapter was followed by an evaluation of the SFR20 element performance which carried out by a series of typical structural problems.

The validation of the proposed elements is carried out through two parts of the work. Firstly, the performance of the SFR20 and SFR20I elements is examined through popular benchmarks in which the efficiency is assessed by comparing the findings with analytical and numerical reference solutions. Both elements uses a reduced integration scheme with $3 \times 3 \times 3$ Gauss points, the reduced numerical integration is used to save calculation time. The presented elements exhibit good performance in terms of accuracy, rate of convergence, and sensitivity to mesh distortion. They are shown to be significantly better than the standard 20-node hexahedron. In particular, the SFR20I element showed excellent

accuracy even for very coarse meshes. The second part of the work was related to the validation of the SFR20 element to analyse the elastoplastic behavior of structures. In this part of the work the element was assessed by adopting two integration schemes; the SFR20 usesd a reduced integration scheme and a full integration scheme element denoted as SFR20F which it uses $4 \times 4 \times 4$ Gauss points.

Due to the difficulty of elastoplastic analysis of structures and the clear need for a powerful computing environment in order to perform these analyzes robustly and efficiently. In addition to that, there is a need to examine the results accurately and clearly. The SFR20 element and the elastoplastic constitutive model were implemented as customizable feature called user subroutines in the commercial finite element package *Abaqus*; which is an environment where it offers to the users to implement new finite elements and material models. This results in the development of two subroutines called **UEL** and **UMAT** for solving and visualization of the results respectively. The performance of the SFR20 and SFR20F to analyse the elastoplastic behavior of structures was assessed by examining different series of typical structural problems. Overall, the proposed element with both integration schemes give identical response comparing to the C3D20 element. The displacement field for the present element against other counterpart are presented. Add to that, the evolution of the Von-Mises stresses and equivalent plastic strain were illustrated and investigated. The post-processing of the equivalent plastic deformation was done by exploiting the properties of **UMAT** subroutine which give the possibility to follow the propagation of plasticity in different structures studied.

In conclusion, according to the series of standard linear and non-linear test cases in this work, it showed that these elements are in general efficient and robust. They have no locking and converge well towards the reference solutions. Add to that, they appear to capture the stresses and strains rapidly as like the C3D20 element. Lastly, the potential of these elements can therefore be exploited to treat other linear and nonlinear phenomena for isotropic and composite materials.

Perspectives

In perspective, this elements are planned to be integrated for the analysis of thermomechanical behavior of structures, where the influence of the thermal loading effect on the structure and the role of the presented elements to capture the displacement field, stresses and strains are investigated.

Another perspective is the implementation of these elements to deal with the problems of large displacements and large deformations by combining geometric nonlinearities effects with material nonlinearities.

Finally, Extend the the use of this elements based on the Space Fiber Rotation concept for the analysis of elastoplastic behavior with damage models.

Appendix A

Shape functions

The shape functions and their derivitives for the 20 node hexahedral element are as follows:

– Vertices nodes:

node	**1**	**2**	**3**	**4**	**5**	**6**	**7**	**8**
ξ	-1	1	1	-1	-1	1	1	-1
η	-1	-1	1	1	-1	-1	1	1
ζ	-1	-1	-1	-1	1	1	1	1

The shape functions and their derivatives of the vertices nodes:

$$\begin{aligned} N_i &= \tfrac{1}{8}(-2+\xi\xi_i+\eta\eta_i+\zeta\zeta_i)(1+\xi\xi_i)(1+\eta_i\eta)(1+\zeta\zeta_i) \\ \tfrac{\partial N_i}{\partial \xi} &= \tfrac{1}{8}\xi_i(1+\eta\eta_i)(1+\zeta\zeta_i)(-1+2\xi\xi_i+\eta\eta_i+\zeta\zeta_i) \\ \tfrac{\partial N_i}{\partial \eta} &= \tfrac{1}{8}\eta_i(1+\xi\xi_i)(1+\zeta\zeta_i)(-1+\xi\xi_i+2\eta\eta_i+\zeta\zeta_i) \\ \tfrac{\partial N_i}{\partial \zeta} &= \tfrac{1}{8}\zeta_i(1+\xi\xi_i)(1+\eta\eta_i)(-1+\xi\xi_i+\eta\eta_i+2\zeta\zeta_i) \end{aligned} \tag{A.1}$$

– Coordinates of the perpendicular plane nodes with ξ axis:

node	**9**	**11**	**13**	**15**
ξ	0	0	0	0
η	-1	1	-1	1
ζ	-1	-1	1	1

The shape functions and their derivatives of nodes $9, 11, 13, 15$:

$$\begin{aligned} N_i &= \tfrac{1}{4}(1-\xi^2)(1+\eta\eta_i)(1+\zeta\zeta_i) \\ \tfrac{\partial N_i}{\partial \xi} &= -\tfrac{1}{2}\xi(1+\eta\eta_i)(1+\zeta\zeta_i) \\ \tfrac{\partial N_i}{\partial \eta} &= \tfrac{1}{4}\eta_i(1-\xi^2)(1+\zeta\zeta_i) \\ \tfrac{\partial N_i}{\partial \zeta} &= \tfrac{1}{4}\zeta_i(1-\xi^2)(1+\eta\eta_i) \end{aligned} \tag{A.2}$$

– Coordinates of the perpendicular plane nodes with η axis:

node	**10**	**12**	**14**	**16**
ξ	1	-1	1	-1
η	0	0	0	0
ζ	-1	-1	1	1

The shape functions and their derivatives of nodes $10, 12, 14, 16$:

$$\begin{aligned} N_i &= \tfrac{1}{4}(1+\xi\xi_i)(1-\eta^2)(1+\zeta\zeta_i) \\ \tfrac{\partial N_i}{\partial \xi} &= \tfrac{1}{4}\xi_i(1-\eta^2)(1+\zeta\zeta_i) \\ \tfrac{\partial N_i}{\partial \eta} &= -\tfrac{1}{2}\eta(1+\xi\xi_i)(1+\zeta\zeta_i) \\ \tfrac{\partial N_i}{\partial \zeta} &= \tfrac{1}{4}\zeta_i(1+\xi\xi_i)(1-\eta^2) \end{aligned} \tag{A.3}$$

– Coordinates of the perpendicular plane nodes with ζ axis:

node	**17**	**18**	**19**	**20**
ξ	-1	1	1	-1
η	-1	-1	1	1
ζ	0	0	0	0

The shape functions and their derivatives of nodes $17, 18, 19, 20$:

$$\begin{aligned} N_i &= \tfrac{1}{4}(1+\xi\xi_i)(1+\eta\eta_i)(1-\zeta^2) \\ \tfrac{\partial N_i}{\partial \xi} &= \tfrac{1}{4}\xi_i(1+\eta\eta_i)(1-\zeta^2) \\ \tfrac{\partial N_i}{\partial \eta} &= \tfrac{1}{4}\eta_i(1+\xi\xi_i)(1-\zeta^2) \\ \tfrac{\partial N_i}{\partial \zeta} &= -\tfrac{1}{2}\zeta(1+\xi\xi_i)(1+\eta\eta_i) \end{aligned} \tag{A.4}$$

Appendix B

Abaqus implementation tutorial

B.1 Implementation aspects of elastoplasticity model in Abaqus

Figure B.1 demonstrate a basic flowchart with data flow and actions for an Abaqus/-Standard analysis and the levels of application of different Abaqus subroutines. These subroutines are used in conjuction with Abaqus allowing the user to perform a variety of common tasks (eg: Structural Engineering Analysis, Computational Fluid Dynamics, Heat Transfer). The implimentation of subroutines such UEL and UMAT requires basically two files; an Input file with the extension (*.inp) ; this file contains all the data about the model (ie. node, connectivity, material properties, ...etc). The second is the source code file written in Fortran language with the extension (*.for), this file possess the user's coding for the computation model.

B.1.1 The Input file

The ABAQUS Input file contains all the commands (keywords) defining the model to generate the simulation. The keywords are pre-define functions address instructions, commands or values to Abaqus to be performed. There are three types of lines in the Input file; The lines that start with double asterisk signify that this line is a comment. Hence, Abaqus passes it without reading what it contains. The command lines start with one asterisk and they contains keywords to be performed by Abaqus. The last type is the Data lines and they are statements and they have a specific format (ex: numerical value, words). The following are descriptions of the main keywords of the input file:

- `*Heading`: This keyword defines the title of the analysis.

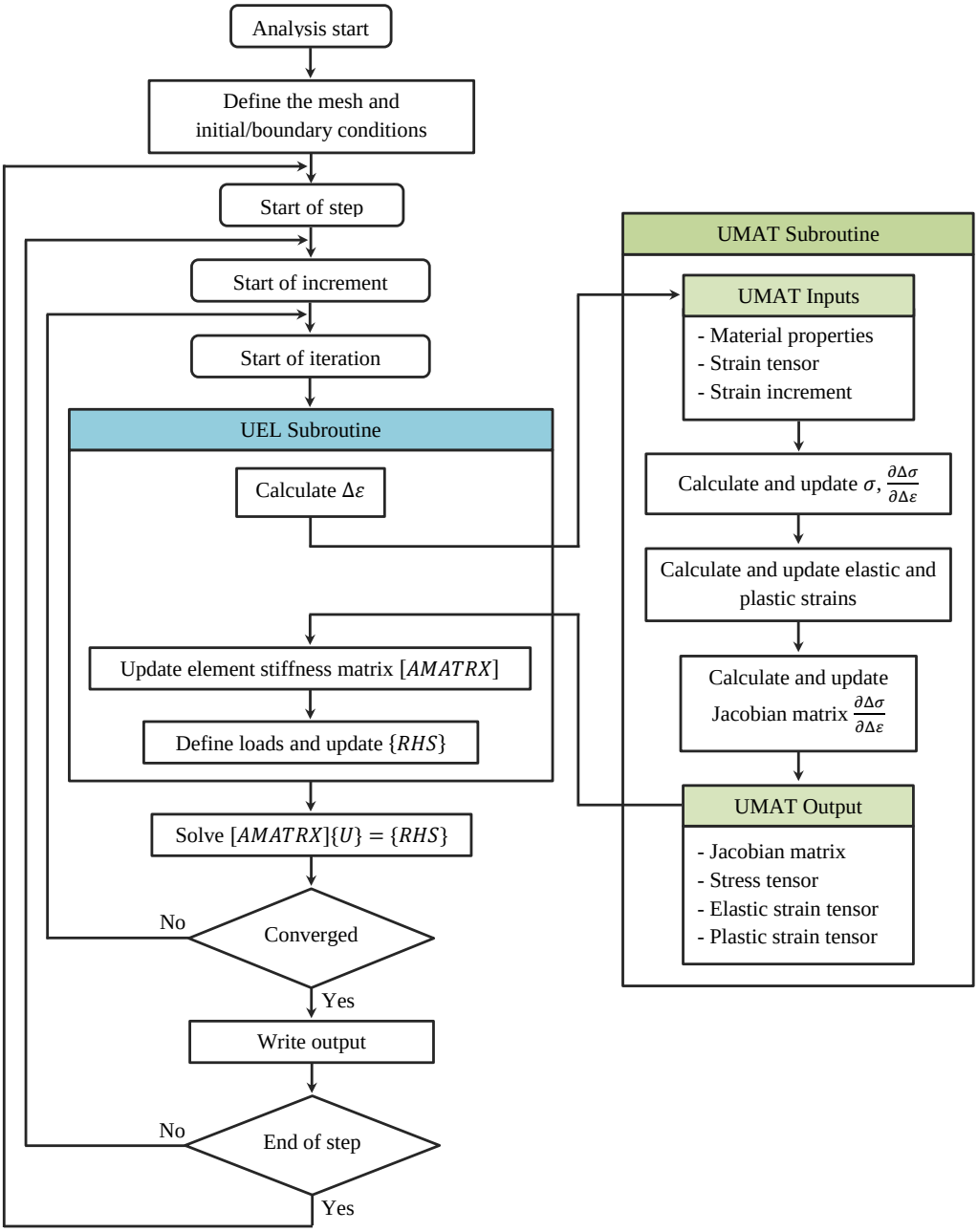

Figure B.1: Standard Abaqus analysis flowchart with implementation of UEL and UMAT subroutines.

- `*Preprint`: Print data from the input file to *Data file* with the extension (`*.data` in order to verify weather Abaqus read and understood the input file correctly.
- `*Part`: Start the defintion of the problem geometry.
- `*Node, input=X:\...dir\nodes.txt`: Indicates the start of node coordinates definition. Node coordinates are imported using the `input` attribute from the (nodes.txt)

file containing the coordinates data.

- `*Element, input=X:\...dir\connec.txt`: Indicates the start of element connectivity definition. element connectivity are imported using the `input` attribute from the (connec.txt) file containing the element connectivity data.
- `*Elset, *Nset`: Set/Group of elements and nodes respectively.
- `*Step`: Define the analysis type of the simulation (i.e. static, dynamic, viscoelastic, ...etc). The user can define one or more of analysis steps, step sequence is a convenient way to capture changes in the loading and boundary conditions of the model.
  - `*Static`: Type of the analysis, the data line after this keyword defines the number of load increments, minimum and maximum amount of load for automatic time stepping, the user can customize general solution and solver controls.
  - `*Boundary`: Define the boundary conditions of the model, the values could be all basic solution variables (displacements, rotations, or temperature). Boundaries are defined with node/element sets.
  - `*Load`: Define external loading to the model, as like the boudary the loads are defined by node/element sets.
  - `*Node Output, *element output`: Output request defines which variables will be output during the analysis step, these output could be nodal or element outputs.

B.1.2 Source code file

Abaqus subroutines are typically follow Fortran77 or C languages conventions.Each subroutine is provided with pre-defined set of *Subroutine arguments*; these arguments should not be violated otherwise the Abaqus will give an error leading to abord the analysis.

B.1.2.1 Description of the UEL subroutine

User-defined **EL**ement (UEL) is a subroutine that allows the user to implement linear or nonlinear finite elements. A user element is defined by the following typical interface:

```
      SUBROUTINE UEL(RHS,AMATRX,SVARS,ENERGY,NDOFEL,NRHS,NSVARS,
     1 PROPS,NPROPS,COORDS,MCRD,NNODE,U,DU,V,A,JTYPE,TIME,DTIME,
     2 KSTEP,KINC,JELEM,PARAMS,NDLOAD,JDLTYP,ADLMAG,PREDEF,NPREDF,
     3 LFLAGS,MLVARX,DDLMAG,MDLOAD,PNEWDT,JPROPS,NJPROP,PERIOD)
C
      INCLUDE 'ABA_PARAM.INC'
C
      DIMENSION RHS(MLVARX,*),AMATRX(NDOFEL,NDOFEL),PROPS(*),
     1 SVARS(*),ENERGY(8),COORDS(MCRD,NNODE),U(NDOFEL),
     2 DU(MLVARX,*),V(NDOFEL),A(NDOFEL),TIME(2),PARAMS(*),
     3 JDLTYP(MDLOAD,*),ADLMAG(MDLOAD,*),DDLMAG(MDLOAD,*),
     4 PREDEF(2,NPREDF,NNODE),LFLAGS(*),JPROPS(*)

      'user coding to define RHS, AMATRX, SVARS, ENERGY, and PNEWDT'

      RETURN
      END
```

Listing B.1: Typical UEL subroutine interface

UEL subroutine arguments are described as:

- `RHS`: Stands for Right Hand Sided, an array containing the residual vector corresponding to a single element, the size of this array is (NDOFEL × NRHS).
- `NDOFEL`: Number of degrees of freedom in the element.
- `NRHS`: Number of load vectors.
- `AMATRX`: An array containing the Jacobian stiffness matrix, the size of this array is (NDOFEL × NDOFEL).
- `SVARS`: An array containing the values of the solution-dependent state variables associated with the element, the size of this array is (NSVARS × 1)
- `NSVARS`: Number of solution-dependent state variables (SDVs), defined by the user.
- `PROPS`: An array containing real property values defined for use with element, the size of this array is (NPROPS × 1).
- `NPROPS`: Number of property values.
- `COORDS`: An array containing the real node coordinates of the element, the size of this array is (MCRD × NNODE).

- `MCRD`: Maximum of the user-defined number of coordinates.
- `NNODE`: User-defined number of nodes on the element.
- `U`: Array containing the current estimates of the basic solution variables (displacements, rotations, temperatures, ...etc).
- `JELEM`: User-assigned element number.

In this subroutine Abaqus expects from the user to define the elemental stiffness matrix `AMATRX` and the residual force vector `RHS` according to the constitutive relation **??**. Abaqus calls the UEL for each element independently and within UEL we have a loop over Gauss integration points where the shape functions $[N]$ and their derivitives $[\partial N]$, the Jacobian determinant $detJ$, the element stiffness matrix $[K^e]$ and load vector $\{F^e_{ext}\}$ are calculated in order to estimate the basic solution variables `U`. At the end of looping over all the elements Abaqus performs the assembly of the system automatically to obtain the global stiffness matrix to solve the constitutive model.
Before the user proceed the simulation using the UEL subroutine, few changes have to be made in the original input file to incorporate a successful implementation. The SFR20 element must be declare using the ∗`USER ELEMENT` command, this command must appear before the user element is invoked with the ∗`ELEMENT` option, Table B.1 explaine the following lines:

```
1 *USER ELEMENT, TYPE=Un, NODES=NNODE, COORDINATES=MCRD,
2 PROPERTIES=NPROPS, I PROPERTIES=NPROPS, VARIABLES=NSVARS, UNSYMM
3 Data line(s)
```

Next, the SFR element connectivity must be declared by the typical ∗`ELEMENT` coomand. The `type` parameter should be defined by the same name as the one given when the UEL was defined (ie. `Un`). Then the element connectivities are liste in standard manner:

```
1 *ELEMENT,TYPE=Un, ELSET=UEL
2 Data line(s)
```

The user can specifie a name for the element set to wich these elements are assigned by the command `ELSET`.

Property values of the model are given by the ∗`UEL PROPERTY` option by the following command lines:

```
1 *UEL PROPERTY, ELSET=UEL
2 Data line(s)
```

Data line for the UEL property could be any parameter, coefficient or value. Note that the `ELSET` name for the *`UEL PROPERTY` option must be the same as the one defined in the *`ELEMENT`.

The following Table B.1 explains the definition of each parameter and what argument passes to the UEL from this entries.

Table B.1: Syntax definition for interfacing UEL.

Parameter	Argument	Definition
TYPE	Un	Element type defined by the user, where n is an integer number $n = 1, 2, ..., 99$
NODES	NNODE	Number of nodes on the element
COORDINATES	MCRD	Maximum number of coordinates in nodes (x, y, z)
PROPERTIES	NPROPS	Number of floating point properties
I PROPERTIES	NPROPS	Number of integer properties
VARIABLES	NSVARS	Number of state dependent solution variables SDVs
UNSYMM	-	Unsymmetric Jacobian Flag
ELSET	NAME	Element set name
UEL PROPERTY	Data line(s)	Invoke the UEL subroutine

B.1.2.2 Description of the UMAT subroutine

User-defined **MAT**erial (UMAT) is a subroutine that allows the user to implement general constitutive linear or nonlinear equations. It is worth noting that UMAT subroutine is used with ABAQUS/STANDARD only, in the other hand, VUMAT subroutine is used with ABAQUS/EXPLICITE. A typical interface of the UMAT subroutine is given below:

```
      SUBROUTINE UMAT(STRESS,STATEV,DDSDDE,SSE,SPD,SCD,
     1 RPL,DDSDDT,DRPLDE,DRPLDT,STRAN,DSTRAN,TIME,DTIME,TEMP,
     2 DTEMP,PREDEF,DPRED,CMNAME,NDI,NSHR,NTENS,NSTATV,PROPS,
     3 NPROPS,COORDS,DROT,PNEWDT,CELENT,DFGRD0,DFGRD1,NOEL,
     4 NPT,LAYER,KSPT,KSTEP,KINC)
C
      INCLUDE 'ABA_PARAM.INC'
C
      CHARACTER*80 CMNAME
      DIMENSION STRESS(NTENS),STATEV(NSTATV),DDSDDE(NTENS,NTENS),
     1 DDSDDT(NTENS),DRPLDE(NTENS),STRAN(NTENS),DSTRAN(NTENS),
     2 TIME(2),PREDEF(1),DPRED(1),PROPS(NPROPS),COORDS(3),
     3 DROT(3,3),DFGRD0(3,3),DFGRD1(3,3)

```

```
15      'user coding to define DDSDDE, STRESS, STATEV, SSE, SPD, SCD
16      and, if necessary, RPL, DDSDDT, DRPLDE, DRPLDT, PNEWDT'
17
18      RETURN
19      END
```

Listing B.2: Typical UMAT subroutine interface

UMAT subrooutine arguments are described as follows:

- `STRESS`: The stress tensor, the size of this array is (NTENS).
- `NTENS`: Size of arrays equals to the sum of Number of direct stress components NDI and number of engineering shear stress components NSHR.
- `STATEV`: An array containing the solution-dependent state variables, the size of this array is (NSTATV).
- `NSTATV`: Number of solution-dependent state variables SDVs.
- `DDSDDE`: Array of the Jacobian matrix of the constitutive model, the size of this array is (NTENS,NTENS).
- `SSE`: Specific elastic strain energy.
- `SPD`: plastic dissipation.
- `STRAN`: An array containing the total strains, the size of this array is (NTENS).
- `DSTRAN`: Array of strain increments, the size of this array is (NTENS).
- `COORDS`: An array containing the original coordinates.
- `DROT`: Rotation increment matrix.

The user has to provide all the calculations to determine the tangent stiffness matrix `DDSDDE` and to update the stress tensor as well as to store the SDVs in the UMAT array `STATEV` whose values are needed for post-processing usage.

As like the UEL subroutine, before conducting any simulation by the UMAT, few changes must be made in the input file. the following lines act as the interface of the UMAT:

```
*MATERIAL, NAME=STEEL
*USER MATERIAL, CONSTANTS=NPROPS, (UNSYMM)
Data line(s)
*DEPVAR
NSTATV
```

The option that invoke the UMAT usage is ∗USER MATERIAL; this option must be located after the original command ∗MATERIAL, the user can give a name to define material with the NAME command. The CONSTANTS command specifies the number of property values that can be used in the UMAT subroutine. If the unsymetric equation solution technique will be used the user should add the command UNSYMM at the last of the line. The option ∗DEPVAR stands for solution dependent variables and NSTATV is the number of SDVs used to allocate space at each material point.

B.1.3 Implementation of the SFR20 element in Abaqus

The presented SFR20 element was implemented in the Abaqus by the UEL subroutine, while the elastoplastic constitutive model is implemented in the form of UMAT subroutine. In order to insure the exchange of information between both subroutines in cases involving coupled systems such as elastoplasticity; two approaches are generally used through the literature [107]:

- Figure B.2 demonstrate the flow of the first approach, the process is through a FORTRAN construct called COMMON Block; this built-in function allows the exchange of the Jacobian matrix DDSDDE from the UMAT to UEL subroutine for every integration point; which will be incorporated to build the element stiffness matrix Equation (5.112) and to obtain the nodal variables U. The stress tensor, the elastic and plastic strain tensors will be determined inside the UMAT subroutine and stored in the STATEV array for the visualisation of results.

- The second approach consists on the development of the elastoplastic behavior calculation code in the UEL Suboutine it self; that means all the calculation supposed to be done in the UMAT should be incorporated in the UEL without using the User MATerial subroutine, this leads to the definition of the Jacobian matrix, the stress tensor, the elastic and plastic strain tensor. All the mentioned arguments need to be defined inside the UEL and stored in the SVARS array.

The elastoplastic behavior was investigated by implementing the presented SFR20 element with UEL-UMAT subroutines using the second approach, this is due to being straightforward and easy to be implemented. Add to that, to aviod the COMMON

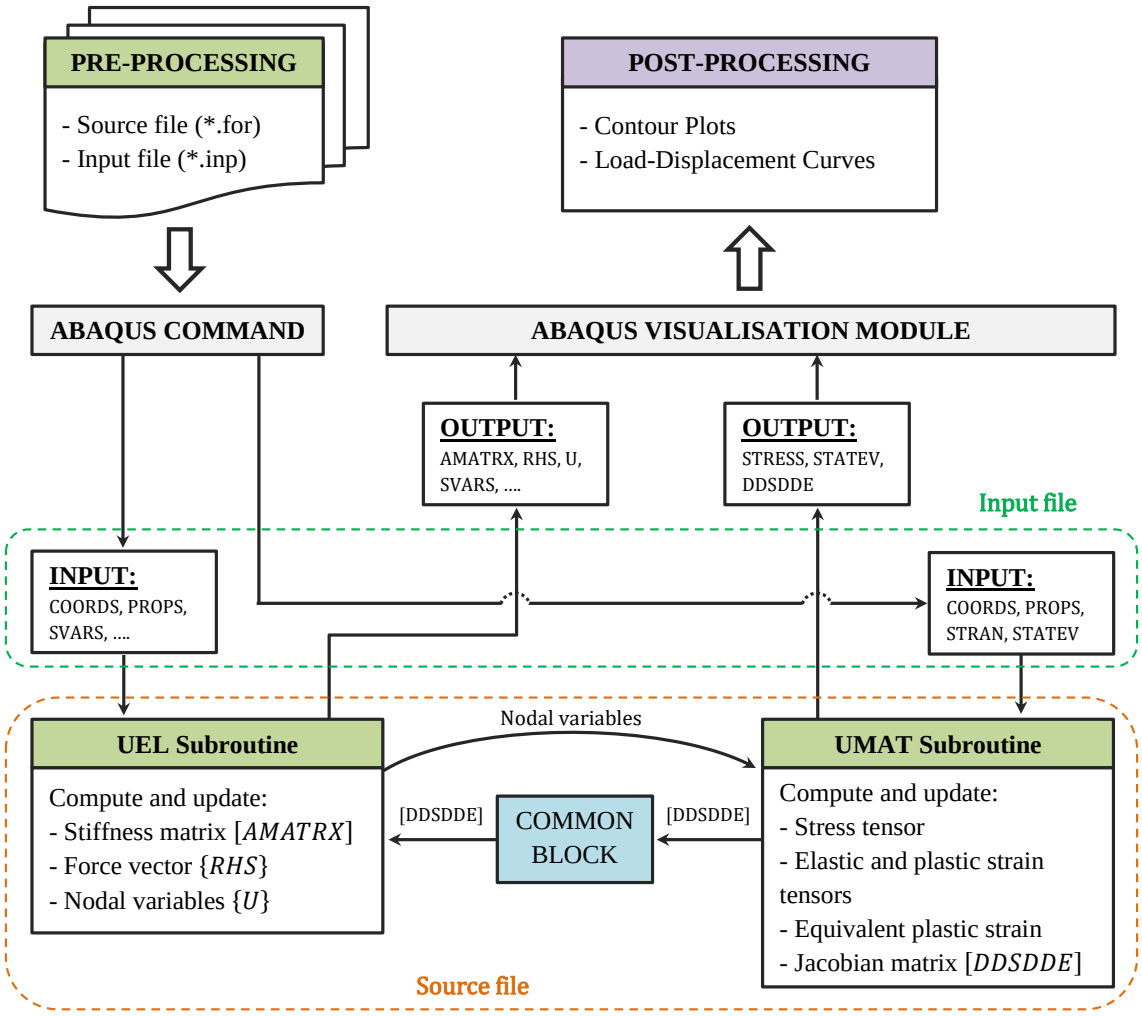

Figure B.2: SFR elements implementation with a UEL and UMAT subroutines using the COMMON block construct for the exchange of data.

block storage problems where large amounts of data are passed between program units. The elastoplastic model was combined with UEL subroutine; where the finite element is developed and the UMAT was used to store the SDVs (i.e. Stresses, elastic strain, Von-Mises Stress and the effective plastic strain).

B.1.4 Running and visualisation

After moving the input file and source code in one directory, The user can submit an Abaqus analysis using subroutines after navigating to the mentioned directory through the Abaqus Command and insert the following line to be excuted:

```
abaqus job=job-name user={source-file | object-file} Other-Commands
```

The word `abaqus` will start the Abaqus compiler in the background, the `job` command defines the input file as the job name, the source code is defined by the command `user`

where the user can insert a (*.for) or (*.obj) file, the last command Other-Command is allocated for other useful commands as like:

```
cpus={number-of-cpus} parallel={domain | loop} gpu={NVIDIA | OFF}
```

Abaqus create several files in the same directory after the analysis is finished, the important files are *log file* (*.log), *data file* (*.dat), *message file* (*.msg), *status file* (*.sta) and *output database file* (*.odb). Each file stores important information that can be used for restarting, postprocessing or other options. The *log file* gives a report about the start and end times for modules run by the current ABAQUS execution procedure, it also contains syntax errors encountered during the analysis. The *data file* print out summary of the input file, the problem size (ie. number of elements, nodes, ...etc), status of the analysis (completed, aborted, ...etc) and job time summary. The convergence of the analysis and incrementation time is reported in the *message file*, the time stepping and incrementation size are summariesed in the *status file*. Finaly, the results are investigated and viewed in the visualization module in ABAQUS/CAE by openning the generated file *output database file*.

When User defined subroutines the investigation of the results using the standard post-processing tool Abaqus/Viewer became not possible, to overcome this drawback two approacher are used to treat the *output database file* for contour plots:

- The first approach is by using special *python scripting* to simulate the topology of the standard Abaqus finite element, this approach is a complex task and it requires more additional user defined information concerning the topology of the developed element [108].

- The most used approach is the *Layer structure* and it was used in the work of [107], to mention but a few. The layer structure approach consiste on attaching each element UEL and UMAT to a layer; where the first and second layer are related to the UMAT and UEL element, respectively. The first layer for UEL elemnt is related to the calculation of the stiffness matrix and the residual vector, whereis, the second layer or the UMAT element is related to the calculation of the elastoplastic behavior and for post-proccessing porposes. It is worth noting that the user must take into account these points:

  - The chosen UMAT element should be a standard Abaqus element and have the same number of nodes as the UEL element does;

  - Both layers share the same nodes. However, they contribute to different element matrices.

The UEL and UMAT elements can be visualized as stacked one over other when post-processing the output data base file in the Abaqus/Viewer module. An example of the input file is illustrated in Appendix B.2, it demonstrates the process of creating two layers; where the SFR20 element is implemented in UEL subroutine and the Abaqus C3D20 element was implemented in the UMAT subroutine for the visualisation purposes.

B.2 Input file for UEL-UMAT visualisation

The following Listing B.2 is an example of the input file for the one element analysis test. This file contains all the details to perform a successful analysis and the implementation of both UEL and UMAT for post-proccesing porposes.

```
*Heading
*Preprint, echo=NO, model=NO,
 history=NO, contact=NO
**
*Node
   1,      100.,     100.0,    100.
   2,      100.,     0.,    100.
   3,      100.,     100.0,    0.
   .
   .
   .
  19,      50.,      0.,      0.
  20,      50.,      100.0,      0.
***************************
** Creating the first layer
** UEL (SFR) finite elements
***************************
*USER ELEMENT, TYPE=U1, NODES=20,
 COORDINATES=3,PROPERTIES=14,
 VARIABLES=378
*ELEMENT, TYPE=U1, ELSET=SOLID
1,  5,  6,  8,  7,  1,  2,  4,  3,
   12, 11, 10,  9, 13, 14, 15,
   16, 18, 17, 19, 20
*UEL PROPERTY, ELSET=SOLID
**E   ,   nu ,  Sy
 70.0,    0.2,  0.0, 0.243, . . .,
 1.9, 0.623
**
***************************
** Creating the second layer
** DUMMY finite elements
***************************
*ELEMENT, TYPE=C3D20, ELSET=output
2,  5,  6,  8,  7,  1,  2,  4,  3,
   12, 11, 10,  9, 13, 14, 15,
   16, 18, 17, 19, 20
*Nset, nset=Set-1
  1,  20,   1
*Elset, elset=Set-1
 1,
*Solid Section, elset=output,
 material=USER
,
*Nset, nset=XSYM
  5,  6,  7,  8,  9, 10, 11, 12
*Nset, nset=YSYM
  2,  4,  6,  8,  11, 14, 17, 19
*Nset, nset=DISP
  1,  3,  5,  7,  9, 16, 18, 20
*Nset, nset=CORNER
  1,  3,  5,  7
```

```
*Nset, nset=MIDLE
  9, 16, 18, 20
**************************
*Material, name=USER
*Depvar
     14
1, S11, S11
2, S22, S22
3, S33, S33
4, S12, S12
5, S23, S23
6, S13, S13
7, E11, E11
8, E22, E22
9, EE33, EE33
10, EE12, EE12
11, EE23, EE23
12, EE13, EE13
13, EQPLS, EQPLS
14, MIS, MIS
*User Material, constants=1
1.,
**************************
** STEP
*Step,EXTRAPOLATION=NO, nlgeom=NO,
 inc=10000
*Static
0.05, 1.,  ,0.05
*Boundary
XSYM, XSYMM
*Boundary
YSYM, YSYMM
**************************
**Boundary
**LOAD, 2, 2,  -1.5
*Cload
CORNER, 2,  -105.00
*Cload
MIDLE, 2,   -445.00
**************************
*Output, field
*Node Output
U, RF
*Element Output
SDV,
*node print
U
*END STEP
```

Listing B.3: Input file example for the one element analysis test.

References

[1] Sarhan M Musa. *Computational Finite Element Methods in Nanotechnology.* CRC Press, 2012. 1

[2] Ivo Babuska and Abdul K Aziz. **Lectures on mathematical foundations of the finite element method.** Technical report, MARYLAND UNIV., COLLEGE PARK. INST. FOR FLUID DYNAMICS AND APPLIED MATHEMATICS., 1972. 1

[3] Olek C Zienkiewicz, Robert Leroy Taylor, and Jian Z Zhu. *The finite element method: its basis and fundamentals.* Elsevier, 2005. 1, 2, 6

[4] Junuthula Narasimha Reddy. *Introduction to the finite element method.* McGraw-Hill Education, 2019. 2

[5] Klaus-Jürgen Bathe. *Finite element procedures.* Klaus-Jurgen Bathe, 2006. 2, 41

[6] Thomas JR Hughes. *The finite element method: linear static and dynamic finite element analysis.* Courier Corporation, 2012. 2

[7] John Tinsley Oden and Junuthula Narasimha Reddy. *An introduction to the mathematical theory of finite elements.* Courier Corporation, 2012. 2

[8] I Babuška and WC Rheinboldt. **Adaptive approaches and reliability estimations in finite element analysis**. *Computer Methods in Applied Mechanics and Engineering*, **17**:519–540, 1979. 2

[9] Les Piegl and Wayne Tiller. *The NURBS book.* Springer Science & Business Media, 1996. 2

[10] Thomas JR Hughes, John A Cottrell, and Yuri Bazilevs. **Isogeometric analysis: CAD, finite elements, NURBS, exact geometry and mesh refinement**. *Computer methods in applied mechanics and engineering*, **194**(39-41):4135–4195, 2005. 2

[11] Julia Ling, Reese Jones, and Jeremy Templeton. **Machine learning strategies for systems with invariance properties**. *Journal of Computational Physics*, **318**:22–35, 2016. 2

[12] CA Brebbia et al. *Boundary element methods in engineering*. Springer, 1982. 2

[13] J Austin Cottrell, Thomas JR Hughes, and Yuri Bazilevs. *Isogeometric analysis: toward integration of CAD and FEA*. John Wiley & Sons, 2009. 3

[14] Douglas Arnold, Richard Falk, and Ragnar Winther. **Finite element exterior calculus: from Hodge theory to numerical stability**. *Bulletin of the American mathematical society*, **47**(2):281–354, 2010. 3

[15] Yousef Saad. *Iterative methods for sparse linear systems*. SIAM, 2003. 3

[16] Ivo Babuska, Barna A Szabo, and I Norman Katz. **The p-version of the finite element method**. *SIAM journal on numerical analysis*, **18**(3):515–545, 1981. 3

[17] Peter Benner, Ekkehard Sachs, and Stefan Volkwein. *Model order reduction for PDE constrained optimization*. Springer, 2014. 3

[18] Jean-Louis Batoz and Gouri Dhatt. *Modélisation des structures par éléments finis: Solides élastiques*. Presses Université Laval, 1990. 4, 41

[19] R. H. MacNeal and R. L. Harder. **A proposed standard set of problems to test finite element accuracy**. *Finite Elements in Analysis and Design*, **1**:3–20, 1985. 4, 41, 42, 50, 51, 52, 55, 57

[20] Thomas JR Hughes, Martin Cohen, and Medhat Haroun. **Reduced and selective integration techniques in the finite element analysis of plates**. *Nuclear Engineering and design*, **46**(1):203–222, 1978. 4

[21] OC Zienkiewicz, RL Taylor, and JM Too. **Reduced integration technique in general analysis of plates and shells**. *International Journal for Numerical Methods in Engineering*, **3**(2):275–290, 1971. 4

[22] E. L. Wilson, R. Taylor, W. P. Doherty, and J. Ghaboussi. *Numerical and Computer Methods in Structural Mechanics: Proceedings*, chapter Incompatible displacement models, pages 43–57. Academic Press, New York, 1973. 4

[23] Robert L Taylor, Peter J Beresford, and Edward L Wilson. **A non-conforming element for stress analysis**. *International Journal for numerical methods in Engineering*, **10**(6):1211–1219, 1976. 4

[24] Juan C Simo and MS10587420724 Rifai. **A class of mixed assumed strain methods and the method of incompatible modes**. *International journal for numerical methods in engineering*, **29**(8):1595–1638, 1990. 4

[25] U Andelfinger and E Ramm. **EAS-elements for two-dimensional, three-dimensional, plate and shell structures and their equivalence to HR-elements**. *International journal for numerical methods in engineering*, **36**(8):1311–1337, 1993. 5

[26] Juan-Carlos Simo and Francisco Armero. **Geometrically non-linear enhanced strain mixed methods and the method of incompatible modes**. *International Journal for Numerical Methods in Engineering*, **33**(7):1413–1449, 1992. 5

[27] JC Simo, F Armero, and RL Taylor. **Improved versions of assumed enhanced strain tri-linear elements for 3D finite deformation problems**. *Computer methods in applied mechanics and engineering*, **110**(3-4):359–386, 1993. 5

[28] Magnus Fredriksson and Niels Saabye Ottosen. **Accurate eight-node hexahedral element**. *International journal for numerical methods in engineering*, **72**(6):631–657, 2007. 5

[29] RJ Sousa, RM Jorge, RA Valente, and JMA Sá. **A new volumetric and shear locking-free 3D enhanced strain element**. *Engineering Computations: Int J for Computer-Aided Engineering*, **20**(7):896–925, 2003. 5

[30] Theodore HH Pian. **State-of-the-art development of hybrid/mixed finite element method**. *Finite elements in analysis and design*, **21**(1-2):5–20, 1995. 5

[31] THH Pian. **A historical note about 'hybrid elements'**. *International Journal for Numerical Methods in Engineering*, **12**(5):891–892, 1978. 5

[32] Theodore HH Pian and K Sumihara. **Rational approach for assumed stress finite elements**. *International Journal for Numerical Methods in Engineering*, **20**(9):1685–1695, 1984. 5

[33] Theodore HH Pian and Pin Tong. **Relations between incompatible displacement model and hybrid stress model**. *International Journal for Numerical Methods in Engineering*, **22**(1):173–181, 1986. 5

[34] KY Sze and A Ghali. **Hybrid hexahedral element for solids, plates, shells and beams by selective scaling**. *International Journal for Numerical Methods in Engineering*, **36**(9):1519–1540, 1993. 5

[35] Flávio LS Bussamra, Paulo de Mattos Pimenta, and João António Teixeira de Freitas. **Hybrid-Trefftz stress elements for three-dimensional elastoplasticity**. *Computer Assisted Mechanics and Engineering Sciences*, **8**(2-3):235–246, 2001. 5

[36] FLS Bussamra, E Lucena Neto, and DS Raimundo Jr. **Hybrid quasi-Trefftz 3-D finite elements for laminated composite plates**. *Computers & structures*, **92**:185–192, 2012. 5

[37] DJ Allman. **A compatible triangular element including vertex rotations for plane elasticity analysis**. *Computers & Structures*, **19**(1-2):1–8, 1984. 5

[38] Shah M Yunus, Sunil Saigal, and Robert D Cook. **On improved hybrid finite elements with rotational degrees of freedom**. *International journal for numerical methods in engineering*, **28**(4):785–800, 1989. 5

[39] Shah M Yunus, Timothy P Pawlak, and Robert D Cook. **Solid elements with rotational degrees of freedom: Part 1-hexahedron elements**. *International Journal for Numerical Methods in Engineering*, **31**(3):573–592, 1991. 5, 35

[40] Timothy P Pawlak, Shah M Yunus, and Robert D Cook. **Solid elements with rotational degrees of freedom: Part II-tetrahedron elements**. *International Journal for Numerical Methods in Engineering*, **31**(3):593–610, 1991. 5

[41] R Ayad. **Contribution à la modélisation numérique pour l'analyse des solides et des structures, et pour la mise en forme des fluides non-newtoniens. Application à des matériaux d'emballage**. *Habilitation to conduct researches, University of Reims, Reims, France,(in French)*, 2002. 5

[42] Yan Shang, Chen-Feng Li, and Kang-Yu Jia. **8-node hexahedral unsymmetric element with rotation degrees of freedom for modified couple stress elasticity**. *International Journal for Numerical Methods in Engineering*, **121**(12):2683–2700, 2020. 5

[43] Yan Shang, Song Cen, and Ming-Jue Zhou. **8-node unsymmetric distortion-immune element based on Airy stress solutions for plane orthotropic problems**. *Acta Mechanica*, **229**(12):5031–5049, 2018. 5

[44] Kamel Meftah, Rezak Ayad, and Mabrouk Hecini. **A new 3D 6-node solid finite element based upon the "Space Fibre Rotation" concept**. *European Journal of Computational Mechanics/Revue Européenne de Mécanique Numérique*, **22**(1):1–29, 2013. 5

[45] Rezak Ayad, Wajdi Zouari, Kamel Meftah, Tarak Ben Zineb, and Ayech Benjeddou. **Enrichment of linear hexahedral finite elements using rotations of a virtual space fiber**. *International journal for numerical methods in engineering*, **95**(1):46–70, 2013. 5, 8, 33, 35, 37

[46] Kamel Meftah, Wajdi Zouari, Lakhdar Sedira, and Rezak Ayad. **Geometric non-linear hexahedral elements with rotational DOFs**. *Computational Mechanics*, **57**(1):37–53, 2016. 5, 8

[47] Kamel Meftah, Lakhdar Sedira, Wajdi Zouari, Rezak Ayad, and Mabrouk Hecini. **A multilayered 3D hexahedral finite element with rotational DOFs**. *European Journal of Computational Mechanics*, **24**(3):107–128, 2015. 5, 8

[48] Kamel Meftah and Lakhdar Sedira. **A Four-Node Tetrahedral Finite Element Based on Space Fiber Rotation Concept**. *Acta Universitatis Sapientiae, Electrical and Mechanical Engineering*, **11**(1):67–78, 2019. 5, 6

[49] Ayoub Ayadi, Kamel Meftah, Lakhdar Sedira, and Hossam Djahara. **An Eight-Node Hexahedral Finite Element with Rotational DOFs for Elastoplastic Applications**. *Acta Universitatis Sapientiae, Electrical and Mechanical Engineering*, **11**(1):54–66, 2019. 5, 6, 8

[50] Ayoub Ayadi, Kamel Meftah, and Lakhdar Sedira. **Elastoplastic analysis of plane structures using improved membrane finite element with rotational DOFs**. *Frattura ed Integrità Strutturale*, **14**(52):148–162, 2020. 5, 8

[51] Hexin Zhang and Jun Shang Kuang. **Eight-node membrane element with drilling degrees of freedom for analysis of in-plane stiffness of thick floor plates**. *International journal for numerical methods in engineering*, **76**(13):2117–2136, 2008. 6

[52] A Madeo, R Casciaro, G Zagari, Raffaele Zinno, and G Zucco. **A mixed isostatic 16 dof quadrilateral membrane element with drilling rotations, based on Airy stresses**. *Finite Elements in Analysis and Design*, **89**:52–66, 2014. 6

[53] Nicola A Nodargi and Paolo Bisegna. **A novel high-performance mixed membrane finite element for the analysis of inelastic structures**. *Computers & Structures*, **182**:337–353, 2017. 6

[54] ET Ooi, S Rajendran, and JH Yeo. **A 20-node hexahedron element with enhanced distortion tolerance**. *International Journal for Numerical Methods in Engineering*, **60**(15):2501–2530, 2004. 6, 41, 43, 44, 45, 51

[55] E. T. Ooi, S. Rajendran, and J. H. Yeo. **Extension of unsymmetric finite elements US-QUAD8 and US-HEXA20 for geometric nonlinear analyses**. *Engineering Computations*, **24**:407–431, 2007. 6

[56] Chong-Jun Li, Juan Chen, and Wan-Ji Chen. **A 3D hexahedral spline element**. *Computers & structures*, **89**(23-24):2303–2308, 2011. 6, 41

[57] Henri Edouard Tresca. *Sur l'ecoulement des corps solides soumis a de fortes pressions*. Imprimerie de Gauthier-Villars, successeur de Mallet-Bachelier, rue de Seine-Saint-Germain, 10, prés l'Institut, 1864. 6

[58] de Saint-Venant. **Mémoire sur l'établissement des équations différentielles des mouvements intérieurs opérés dans les corps solides ductiles au delà des limites où l'élasticité pourrait les ramener à leur premier état.** *Journal de Mathématiques Pures et Appliquées*, **16**:308–316, 1871. 6

[59] Maurice Levy. **Extrait du Mémoire sur les équations générales des mouvements intérieurs des corps solides ductiles au delà des limites où l'élasticité pourrait les ramener à leur premier état; présenté le 20 juin 1870.** *Journal de Mathématiques Pures et Appliquées*, **16**:369–372, 1871. 6

[60] Rodney Hill. *The mathematical theory of plasticity*, **11**. Oxford university press, 1998. 6

[61] R v Mises. **Mechanik der festen Körper im plastisch-deformablen Zustand**. *Nachrichten von der Gesellschaft der Wissenschaften zu Göttingen, Mathematisch-Physikalische Klasse*, **1913**:582–592, 1913. 6

[62] Heinrich Hencky. **Zur Theorie plastischer Deformationen und der hierdurch im Material hervorgerufenen Nachspannungen**. *ZAMM-Journal of Applied Mathematics and Mechanics/Zeitschrift für Angewandte Mathematik und Mechanik*, **4**(4):323–334, 1924. 6

[63] Ludwig Prandtl. *Spannungsverteilung in platischen korpern*. Waltman, 1925. 6

[64] GG Pope. **A discrete element method for the analysis of plane elasto-plastic stress problems**. *Aeronautical Quarterly*, **17**(1):83–104, 1966. 7

[65] PV Marcal and I Po King. **Elastic-plastic analysis of two-dimensional stress systems by the finite element method**. *International Journal of Mechanical Sciences*, **9**(3):143–155, 1967. 7

[66] Yoshimura Yamada, N Yoshimura, and T Sakurai. **Plastic stress-strain matrix and its application for the solution of elastic-plastic problems by the finite element method**. *International Journal of Mechanical Sciences*, **10**(5):343–354, 1968. 7, 91

[67] IM May and IAS Al-Shaarbaf. **Elasto-plastic analysis of torsion using a three-dimensional finite element model**. *Computers & structures*, **33**(3):667–678, 1989. 7

[68] Gustavo G Weber, AM Lush, A Zavaliangos, and Lallit Anand. **An objective time-integration procedure for isotropic rate-independent and rate-dependent elastic-plastic constitutive equations**. *International journal of plasticity*, **6**(6):701–744, 1990. 7

[69] Francisco Armero and Krishna Garikipati. **An analysis of strong discontinuities in multiplicative finite strain plasticity and their relation with the numerical simulation of strain localization in solids**. *International journal of solids and structures*, **33**(20-22):2863–2885, 1996. 7

[70] Ted Belytschko and Tom Black. **Elastic crack growth in finite elements with minimal remeshing**. *International journal for numerical methods in engineering*, **45**(5):601–620, 1999. 7

[71] Yan P Cao, N Hu, H Fukunaga, J Lu, and Zhen H Yao. **A highly accurate brick element based on a three-field variational principle for elasto-plastic analysis**. *Finite elements in analysis and design*, **39**(12):1155–1171, 2003. 7

[72] E Rank, A Düster, V Nübel, K Preusch, and OT Bruhns. **High order finite elements for shells**. *Computer Methods in Applied Mechanics and Engineering*, **194**(21-24):2494–2512, 2005. 7

[73] E Artioli, Giovanni Castellazzi, and P Krysl. **Assumed strain nodally integrated hexahedral finite element formulation for elastoplastic applications**. *International Journal for Numerical Methods in Engineering*, **99**(11):844–866, 2014. 7, 91

[74] Michaela Nagler, Astrid Pechstein, and Alexander Humer. **A mixed finite element formulation for elastoplasticity**. *International Journal for Numerical Methods in Engineering*, **123**(21):5346–5368, 2022. 7

[75] Javier Bonet and Richard D Wood. *Nonlinear continuum mechanics for finite element analysis*. Cambridge university press, 1997. 13, 14

[76] Junuthula Narasimha Reddy. *Principles of continuum mechanics: A study of conservation principles with applications*. Cambridge University Press, 2010. 13

[77] Karan S Surana. *Classical Continuum Mechanics*. CRC Press, 2022. 13

[78] Gouri Dhatt, Emmanuel Lefrançois, and Gilbert Touzot. *Finite element method*. John Wiley & Sons, 2012. 13

[79] David V Hutton. *Fundamentals of finite element analysis*. McGraw-Hill Science Engineering, 2004. 13

[80] Olek C Zienkiewicz and Robert L Taylor. *The finite element method for solid and structural mechanics*. Elsevier, 2005. 13

[81] Jacob Fish and Ted Belytschko. *A first course in finite elements*, **1**. Wiley New York, 2007. 13

[82] Danilo Capecchi. *History of virtual work laws: a history of mechanics prospective*, **42**. Springer Science & Business Media, 2012. 25

[83] Olek C Zienkiewicz, Robert L Taylor, and JZ Zhu. *The Finite Element Method: Its Basis and Fundamentals*. Butterworth-Heinemann, 2013. 25

[84] Farid Abed-Meraim, Vuong-Dieu Trinh, and Alain Combescure. **New quadratic solid–shell elements and their evaluation on linear benchmark problems**. *Computing*, **95**(5):373–394, 2013. 41, 46

[85] ABAQUS. *Analysis User's Manual*. V.6.11, 2010. 41, 42

[86] PC Kohnke. *ANSYS: Theory Reference Release 5.4. ANSYS*. Inc: Canonsburg, PA, 1997. 41

[87] Olgierd Cecil Zienkiewicz, Robert Leroy Taylor, Olgierd Cecil Zienkiewicz, and Robert Lee Taylor. *The finite element method*, **3**. McGraw-hill London, 1977. 41

[88] YK Cheung and Chen Wanji. **Isoparametric hybrid hexahedral elements for three dimensional stress analysis**. *International Journal for Numerical Methods in Engineering*, **26**(3):677–693, 1988. 42, 45, 46

[89] BP Naganarayana and G Prathap. **Field-consistency analysis of 27-noded hexahedral elements for constrained media elasticity**. *Finite elements in analysis and design*, **9**(2):149–168, 1991. 42, 43

[90] Antoine Legay and Alain Combescure. **Elastoplastic stability analysis of shells using the physically stabilized finite element SHB8PS**. *International Journal for Numerical Methods in Engineering*, **57**(9):1299–1322, 2003. 46

[91] Stephen Timoshenko. *Strength of materials*. 1930. 46, 48

[92] PMA Areias, JMA César de Sá, CA Conceição António, and AA Fernandes. **Analysis of 3D problems using a new enhanced strain hexahedral element**. *International Journal for Numerical Methods in Engineering*, **58**(11):1637–1682, 2003. 51

[93] Stephen P Timoshenko and Sergius Woinowsky-Krieger. *Theory of plates and shells*. McGraw-hill, 1959. 53, 54

[94] Timon Rabczuk, PMA Areias, and T Belytschko. **A meshfree thin shell method for non-linear dynamic fracture**. *International journal for numerical methods in engineering*, **72**(5):524–548, 2007. 56

[95] Wilhelm Flügge. *Stresses in shells*. Springer Science & Business Media, 1960. 56, 58

[96] DRJ Owen and E Hinton. *Finite elements in plasticity: theory and practice*. 1980. 60, 68

[97] Peter Wriggers. *Nonlinear finite element methods*. Springer Science & Business Media, 2008. 60, 78

[98] Eduardo A de Souza Neto, Djordje Peric, and David RJ Owen. *Computational methods for plasticity: theory and applications*. John Wiley & Sons, 2011. 60, 65, 66, 89, 91

[99] René De Borst, Mike A Crisfield, Joris JC Remmers, and Clemens V Verhoosel. *Nonlinear finite element analysis of solids and structures*. John Wiley & Sons, 2012. 60

[100] Nam-Ho Kim. *Introduction to nonlinear finite element analysis*. Springer Science & Business Media, 2014. 60

[101] Jamshid Ghaboussi, David A Pecknold, and Xiping Steven Wu. *Nonlinear computational solid mechanics*. CRC Press, 2017. 60

[102] Ted Belytschko, Wing Kam Liu, Brian Moran, and Khalil Elkhodary. *Nonlinear finite elements for continua and structures*. John wiley & sons, 2014. 61

[103] Yury Vetyukov. *Nonlinear mechanics of thin-walled structures: asymptotics, direct approach and numerical analysis*. Springer Science & Business Media, 2014. 61

[104] Percy Williams Bridgman, Percy Williams Bridgman, Percy Williams Bridgman, and Percy Williams Bridgman. *Collected experimental papers*, **6**. Harvard University Press Cambridge, 1964. 69

[105] Mark L Wilkins. **Calculation of elastic-plastic flow**. Technical report, California Univ Livermore Radiation Lab, 1963. 78

[106] PS Theocaris and E Marketos. **Elastic-plastic analysis of perforated thin strips of a strain-hardening material**. *Journal of the Mechanics and Physics of Solids*, **12**(6):377–380, 1964. 91

[107] Subrato Sarkar, Indra Vir Singh, BK Mishra, AS Shedbale, and LH Poh. **A comparative study and ABAQUS implementation of conventional and localizing gradient enhanced damage models**. *Finite Elements in Analysis and Design*, **160**:1–31, 2019. 109, 111

[108] S Roth, G Hütter, U Mühlich, B Nassauer, L Zybell, and M Kuna. **Visualisation of user defined finite elements with abaqus/viewer**. *GACM Rep*, **5**:7–14, 2012. 111